

Low-dimensional Material: Structure-property Relationship and
Applications in Energy and Environmental Engineering

Hang Xiao

Submitted in partial fulfillment of the
requirements for the degree of
Doctor of Philosophy
in the Graduate School of Arts and Sciences

COLUMBIA UNIVERSITY

2017

© 2017

Hang Xiao

All Rights Reserved

ABSTRACT

Low-dimensional Material: Structure-property Relationship and Applications in Energy and
Environmental Engineering

Hang Xiao

In the past several decades, low-dimensional materials (0D materials, 1D materials and 2D materials) have attracted much interest from both the experimental and theoretical points of view. Because of the quantum confinement effect, low-dimensional materials have exhibited a kaleidoscope of fascinating phenomena and unusual physical and chemical properties, shedding light on many novel applications. Despite the enormous success has been achieved in the research of low-dimensional materials, there are three fundamental challenges of research in low-dimensional materials:

- 1) Develop new computational tools to accurately describe the properties of low-dimensional materials with low computational cost.
- 2) Predict and synthesize new low-dimensional materials with novel properties.
- 3) Reveal new phenomenon induced by the interaction between low-dimensional materials and the surrounding environment.

In this thesis, atomistic modelling tools have been applied to address these challenges. We first developed ReaxFF parameters for phosphorus and hydrogen to give an accurate description of the chemical and mechanical properties of pristine and defected black phosphorene. ReaxFF for P/H is transferable to a wide range of phosphorus and hydrogen containing systems including bulk black phosphorus, blue phosphorene, edge-hydrogenated phosphorene, phosphorus clusters and phosphorus hydride molecules. The potential parameters were obtained by conducting global optimization with respect to a set of reference data generated by extensive *ab initio* calculations.

We extended ReaxFF by adding a 60° correction term which significantly improved the description of phosphorus clusters. Emphasis was placed on the mechanical response of black phosphorene with different types of defects. Compared to the nonreactive SW potential of phosphorene, ReaxFF for P/H systems provides a significant improvement in describing the mechanical properties of the pristine and defected black phosphorene, as well as the thermal stability of phosphorene nanotubes. A counterintuitive phenomenon was observed that single vacancies weaken the black phosphorene more than double vacancies with higher formation energy. Our results also showed that the mechanical response of black phosphorene is more sensitive to defects in the zigzag direction than that in the armchair direction. Since ReaxFF allows straightforward extensions to the heterogeneous systems, such as oxides, nitrides, the proposed ReaxFF parameters for P/H systems also underpinned the reactive force field description of heterogeneous P systems, including P-containing 2D van der Waals heterostructures, oxides, etc.

Based on the evolutionary algorithm driven structural search, we proposed a new stable trisulfur dinitride (S_3N_2) 2D crystal that is a covalent network composed solely of S-N σ bonds. S_3N_2 crystal is dynamically, thermally and chemically stable as confirmed by the computed phonon spectrum and ab initio molecular dynamics simulations. GW calculations showed that the 2D S_3N_2 crystal is a wide, direct band-gap (3.92 eV) semiconductor with a small hole effective mass. The anisotropic optical response of 2D S_3N_2 crystal was revealed by GW-BSE calculations. Our result not only marked the prediction of the first 2D crystal composed of nitrogen and sulfur, but also underpinned potential innovations in 2D electronics, optoelectronics, etc.

Inspired by the discovery of S_3N_2 2D crystal, we proposed a new 2D crystal, diphosphorus trisulfide (P_2S_3), based on the extensive evolutionary algorithm driven structural search. The 2D P_2S_3 crystal was confirmed to be dynamically, thermally and chemically stable by the computed

phonon spectrum and *ab initio* molecular dynamics simulations. This 2D crystalline phase of P_2S_3 corresponds to the global minimum in the Born-Oppenheimer surface of the phosphorus sulfide monolayers with 2:3 stoichiometry. It is a wide band gap (4.55 eV) semiconductor with P-S σ bonds. The electronic properties of P_2S_3 structure can be tuned by stacking into multilayer P_2S_3 structures, forming P_2S_3 nanoribbons or rolling into P_2S_3 nanotubes, expanding its potential applications for the emerging field of 2D electronics.

Then we showed that the hydrolysis reaction is strongly affected by relative humidity. The hydrolysis of CO_3^{2-} with $n = 1-8$ water molecules was investigated by *ab initio* method. For $n = 1-5$ water molecules, all the reactants follow a stepwise pathway to the transition state. For $n = 6-8$ water molecules, all the reactants undergo a direct proton transfer to the transition state with overall lower activation free energy. The activation free energy of the reaction is dramatically reduced from 10.4 to 2.4 kcal/mol as the number of water molecules increases from 1 to 6. Meanwhile, the degree of the hydrolysis of CO_3^{2-} is significantly increased compared to the bulk water solution scenario. The incomplete hydration shells facilitate the hydrolysis of CO_3^{2-} with few water molecules to be not only thermodynamically favorable but also kinetically favorable. We showed that the chemical kinetics is not likely to constrain the speed of CO_2 air capture driven by the humidity-swing. Instead, the pore-diffusion of ions is expected to be the time-limiting step in the humidity driven CO_2 air capture. The effect of humidity on the speed of CO_2 air capture was studied by conducting CO_2 absorption experiment using IER with a high ratio of CO_3^{2-} to H_2O molecules. Our result is able to provide valuable insights to designing efficient CO_2 air-capture sorbents.

Lastly, the self-assembly mechanism of one-end-open carbon nanotubes (CNTs) suspended in an aqueous solution was studied by molecular dynamics simulations. It was shown

that two one-end-open CNTs with different diameters can coaxially self-assemble into a nanocapsule. The nanocapsules formed were stable in aqueous solution under ambient conditions, and the pressure inside the nanocapsule was much higher than the ambient pressure due to the van der Waals interactions between two parts of the nanocapsule. The effects of the normalized radius difference, normalized inter-tube distance and aspect ratio of the CNT pairs were systematically explored. The electric field response of nanocapsules was studied with *ab initio* molecular dynamics simulations, which showed that nanocapsules can be opened by applying an external electric field, due to the polarization of carbon atoms. This discovery not only shed light on a simple yet robust nanocapsule self-assembly mechanism, but also underpinned potential innovations in drug delivery, nano-reactors, etc.

Table of Contents

List of Figures	iv
Acknowledgements.....	x
Chapter 1 Introduction and Motivation.....	1
1.1 Why study low-dimensional materials?	1
1.1.1 Zero-dimensional materials	1
1.1.2 One-dimensional materials	2
1.1.3 Two-dimensional materials	2
1.1.4 Applications of low-dimensional materials in energy and environmental engineering	4
1.2 Fundamental challenges of research in low-dimensional materials.....	5
1.3 Atomistic modelling.....	7
1.3.1 <i>Ab initio</i> methods.....	8
1.3.2 Force field methods	9
1.3.3 Molecular dynamics	12
1.4 Outline of dissertation	13
Chapter 2 Development of a Transferable Reactive Force Field of P/H Systems: Application to the Chemical and Mechanical Properties of Phosphorene.....	15
2.1 Introduction	15
2.2 Methodology	17
2.2.1 DFT calculations.....	17
2.2.2 ReaxFF.....	18

2.3	DFT training of force field.....	20
2.4	Parameterization and validation of ReaxFF.....	22
2.4.1	Relative stabilities of bulk black phosphorus, black and blue phosphorene	24
2.4.2	Relative stabilities of phosphorus clusters.....	27
2.4.3	Potential energy curves for phosphorus hydride molecules	29
2.4.4	Defects for black phosphorene	31
2.4.5	Adatoms for black phosphorene: a transferability test	33
2.4.6	Mechanical property of black phosphorene predicted by ReaxFF	34
2.4.7	Effect of defects on the mechanical response of black phosphorene	36
2.4.8	Thermal stability of phosphorene nanotubes.....	39
2.5	Concluding remarks	40
Chapter 3	Prediction of a Two-dimensional S ₃ N ₂ Solid for Optoelectronic Applications	42
3.1	Introduction.....	42
3.2	Computational methods	43
3.3	Results and discussion.....	44
3.4	Concluding remarks	51
Chapter 4	Predicting a Two-dimensional P ₂ S ₃ Monolayer: A Global Minimum Structure	52
4.1	Introduction.....	52
4.2	Computational methods	53
4.3	Results and discussion.....	55
4.4	Concluding remarks	60
Chapter 5	The Catalytic Effect of H ₂ O on the Hydrolysis of CO ₃ ²⁻ in Hydrated Clusters and Its Implication to the Humidity-driven CO ₂ Air Capture	62

5.1	Introduction	62
5.2	Computational methods	65
5.3	Results and discussion.....	65
5.3.1	Hydrolysis reaction with $n = 1-5$	65
5.3.2	Hydrolysis reaction with $n = 6-8$	68
5.3.3	Comparison with the hydrolysis reaction in the bulk water ($n \gg 1$)	70
5.3.4	The driving force of the change in activation free energy.....	70
5.3.5	Implication to the humidity driven CO ₂ air capture.	71
5.4	Concluding remarks	74
Chapter 6	Self-assembled Nanocapsules in Water: A Molecular Mechanism Study	76
6.1	Introduction	76
6.2	Model and method.....	77
6.3	Results and discussions	79
6.3.1	Effect of normalized radius difference $\Delta R/r_m$	80
6.3.2	Effect of normalized inter-tube distance D/r_m	82
6.3.3	Effect of temperature	83
6.3.4	Effect of aspect ratio l/d	84
6.3.5	Open the nanocapsule by an external electric field	87
6.4	Concluding remarks	89
Chapter 7	Conclusions and Future Work.....	90
7.1	Concluding remarks	90
7.2	Future work	92
	Bibliography	94

List of Figures

Figure 1.1 Schematic illustration of the 0D fullerene, 1D carbon nanotube and 2D graphene.	1
Figure 1.2 Humidity swing sorbent for CO ₂ capture directly from ambient air. ⁴⁶	5
Figure 1.3 A schematic illustration of the motives and progresses of this thesis.	6
Figure 1.4 Interatomic distance dependency of the phosphorus-phosphorus bond order.....	11
Figure 1.5 Hierarchy of computational methods on a time vs length scale.	12
Figure 2.1 Crystal structures of bulk black phosphorus, black phosphorene and blue phosphorene calculated by DFT and ReaxFF.	25
Figure 2.2 Relative stabilities of (a) bulk black phosphorus for a broad range of unit cell volume, (b) black phosphorene for a broad range of in-plane unit cell area, (c) blue phosphorene for a broad range of in-plane unit cell area.....	27
Figure 2.3 Structures of phosphorus clusters from DFT and ReaxFF with the 60 ° correction. ..	28
Figure 2.4 DFT and ReaxFF potential energy curves for: (a) dissociation of a P-H bond in phosphine, (b) dissociation of a P-P bond in the P ₂ H ₄ molecule, (c) dissociation of a P-P bond in the P ₂ H ₂ molecule, (d) angle distortion of H-P-H in phosphine, (e) angle distortion of P-P-P in the P ₃ H ₅ molecule, (f) angle distortion of H-P-P in the P ₂ H ₂ molecule, (g) torsion distortion of H-P-P-H in the P ₂ H ₄ molecule and of H-P-P-P in the P ₄ H ₂ molecule.	30
Figure 2.5 Structures of defected black phosphorene calculated with DFT, ReaxFF and SW potential.....	32
Figure 2.6 Adsorption structures of P and H adatoms on black phosphorene calculated with DFT and ReaxFF compared to SW results (only for P adatom).	34

Figure 2.7 (a) Stress-strain responses of black phosphorene along the armchair direction and zigzag direction calculated by ReaxFF and SW potential at 1 K compared to DFT results. (b) Stress-strain responses of black phosphorene along the armchair direction and zigzag direction calculated by ReaxFF at 1K and 300 K.	36
Figure 2.8 Stress-strain responses of defected and defect-free black phosphorene along the armchair direction (a) and the zigzag direction (b) calculated by ReaxFF at 1K.	37
Figure 2.9 Structure deformation and stress distribution of black phosphorene with single vacancy (a), double vacancy (b) and Stone-Wales defect (c) at $\epsilon_{\text{armchair}} = 0.13$. Structure deformation and stress distribution of black phosphorene with single vacancy (d), double vacancy (e) and Stone-Wales defect (f) at $\epsilon_{\text{zigzag}} = 0.13$. Colors show the stress distribution.....	38
Figure 2.10 Cohesive energies of the (m, 0) zigzag PNT (a) and (0, n) armchair PNT (b). The phase diagrams for thermal stability of the (m, 0) zigzag PNTs (c) and the (0, n) armchair PNTs (d) with varying temperatures and wrapping vectors of the nanotube. Stable and unstable PNT structures are shown.....	40
Figure 3.1 2D crystalline structures of α -S ₃ N ₂ (a), β -S ₃ N ₂ (b) and γ -S ₃ N ₂ (c). Bonding is depicted by an isosurface of the electron density.	45
Figure 3.2 The phonon dispersion relations of α -S ₃ N ₂ (a), β -S ₃ N ₂ (b) and γ -S ₃ N ₂ (c). The Brillouin zone of each polymorph, with the relevant high-symmetry k -points indicated, is shown in the inset figure.	46
Figure 3.3 <i>Ab initio</i> MD snapshots of the α -S ₃ N ₂ supercell structures at temperatures (a) T = 800 K (b) T = 1000 K under ambient pressure at 10 ps.....	47

Figure 3.4 <i>Ab initio</i> MD snapshots of the α -S ₃ N ₂ supercell structures exposed to the high pressure (a) oxygen gas, (b) water vapour, (c) nitrogen gas and (d) hydrogen gas at temperatures T = 800 K.....	48
Figure 3.5 Calculated band structure (left) obtained with the PBE functional (blue lines) and the GW method (red dash lines) for the α -S ₃ N ₂ solid. The DOS (right) is obtained with the PBE functional. The effective mass of electrons and holes at the Γ point along the Γ -X and the Γ -Y directions are indicated by black arrows.....	49
Figure 3.6 G ₀ W ₀ +BSE absorption spectra for the α -S ₃ N ₂ crystal for the incident light polarized along the [100] and [010] directions. The black vertical dashed line marks electronic band gap calculated at the level of G ₀ W ₀	50
Figure 4.1 2D crystalline structures of α -P ₂ S ₃ (a), β -P ₂ S ₃ (b) and γ -P ₂ S ₃ (c). The Brillouin zone of each polymorph, with the relevant high-symmetry <i>k</i> -points indicated, is depicted in the inset figure. Bonding is depicted by an isosurface of the electron density.	55
Figure 4.2 The phonon dispersion relations of α -P ₂ S ₃ (a), β -P ₂ S ₃ (b) and γ -P ₂ S ₃ (c).....	56
Figure 4.3 <i>Ab initio</i> MD snapshots of the α -P ₂ S ₃ supercell structures at temperature T = 1000 K under ambient pressure at time t = 0 ps (a) and t = 10 ps (b).	57
Figure 4.4 <i>Ab initio</i> MD snapshots of the α -P ₂ S ₃ supercell structures exposed to the high pressure oxygen gas (a), water vapour (b), hydrogen gas (c), and nitrogen gas (d) at temperatures T = 1000 K.....	58
Figure 4.5 Calculated band structure (left) obtained with the PBE functional (blue lines) and the GW method (black dash lines) for the α -P ₂ S ₃ solid. The DOS (right) is obtained with the PBE functional.	59

Figure 4.6 The electronic band structures of the α -P₂S₃ monolayer (a), α -P₂S₃ bilayer (b) and α -P₂S₃ 3D crystal, obtained with the PBE functional. Monolayer, bilayer and 3D crystal structures of α -P₂S₃ are shown in inset figures. 60

Figure 5.1 Humidity driven CO₂ absorption/desorption on IER. Empty-Fresh state: dry sorbent with only a few water molecules neighboring each carbonate ion. Empty-Dry state: OH⁻ ion and HCO₃⁻ ion are formed by the hydrolysis of CO₃²⁻ in the dry condition. Full-Dry state: the full-loaded sorbent in the dry condition. OH⁻ formation and chemical absorption of CO₂ (Eqs. 5.1-5.2) represent the absorption process. Empty-Wet state: CO₂ regeneration in the wet condition (Eq. 5.3), which represents the physical desorption of CO₂. 63

Figure 5.2 (a) Reactants, intermediates, products and transition states for the reaction in Eq. 5.1 (n = 1-5). (b) Relative free energy profiles (in kcal/mol) for the hydration of CO₃²⁻ with 1-5 water molecules. For transition states and intermediate states, the sodium ions, carbonate ions, bicarbonate ions, hydroxyl ions and the water molecules directly involved in reaction are visualized with the ball-and-stick model, while the water molecules do not directly take part in the reaction are visualized with the tube model. For reactants and products, all species are visualized with the ball-and-stick model. The same visualization protocol is adopted in Figure 5.4. 67

Figure 5.3 The activation free energy (in black) of Eq. 5.1 as a function of the number of H₂O molecules; the reaction free energy (in red) of Eq. 5.1 as a function of the number of H₂O molecules. The activation free energy and reaction free energy in bulk water are calculated with 8 explicit H₂O molecules using the SMD continuum solvation model.¹⁷¹ 68

Figure 5.4 (a) Reactants, intermediates, products and transition states for the reaction in Eq. 5.1 (n = 6-8). (b) Relative free energy profiles (in kcal/mol) for the hydration of CO₃²⁻ with 6-8 water molecules. 69

Figure 5.5 (a) The enthalpic (in red) and entropic (in purple) components of the activation free energy of Eq. 5.1 as a function of the number of H ₂ O molecules. (b) Binding enthalpy of adding one H ₂ O to reactants (in black), transition states (in red) and products (in purple) of the reactions with n water molecules.	71
Figure 5.6 Two different scenarios of the adsorption of H ₂ O on CO ₃ ²⁻ anchored on the surface of a porous material at low humidity.	72
Figure 5.7 (a) Schematic of experimental device. (b) The time to absorb 10 ppm CO ₂ as a function of the ratio of H ₂ O to CO ₃ ²⁻	73
Figure 6.1 Snapshots of the self-assembly process of the nanocapsule from one-end-open (8,8) and (13,13) CNTs. In A, B, C, D and E, nanocapsules are sliced in half to show the water molecules inside. The rigid caps (A, B, C, D, E) are marked in cyan, and the straight regions described by the Morse bond model are marked in green. While in a, b, c, d and e, one-end-open CNTs are marked in grey and water molecules are not displayed for clarity.	78
Figure 6.2 The center-of-mass distance (in black) and the interaction energy (in red) between one-end-open (8,8) and (13,13) nanotubes as a function of time. The nanocapsule is formed at around 400 ps.	80
Figure 6.3 Time evolution of the nanocapsule self-assembly by one-end-open CNT pairs with different normalized radius differences ($\Delta R/r_m$).	81
Figure 6.4 Time evolution of the nanocapsule self-assembly by one-end-open CNT pairs ($\Delta R/r_m = 1.06$) with varying normalized inter-tube distances (D/r_m).	83
Figure 6.5 The nanocapsule self-assembly map as both normalized inter-tube distance (D/r_m) and normalized radius difference ($\Delta R/r_m$) are varied. Snapshots of systems at time t=500 ps are shown. The cases when the nanocapsule is assembled or not at 300 K are separated by the solid red line.	

The scenarios when the nanocapsule is assembled or not at 350 K are separated by the dashed red line (the systems at 350 K are not shown).	84
Figure 6.6 Time evolution of the nanocapsule self-assembly by one-end-open CNT pairs ($\Delta R/r_m = 1.06$, $D/r_m = 0.52$) with different aspect ratio, l/d	85
Figure 6.7 (a) The van der Waals pressure inside the nanocapsule and the interaction energy between two CNTs as a function of the aspect ratio, l/d . Comparison of water structure in the CNTs before (b) and after (c) the nanocapsule is formed. Square ice structure is formed in the smaller CNT due to the high van der Waals pressure and the nano-confinement.	86
Figure 6.8 The electric field response of the nanocapsule when $E=0.25$ V/Å and $E=0.75$ V/Å. The electrostatic potential (ESP) maps and the structures of the nanocapsule at $t=0.2$ ps, 0.6 ps and 1 ps are shown.	88

Acknowledgements

First and foremost, I would like to offer my sincere thanks and appreciation to my advisor, Dr. Xi Chen, for his support, guidance, understanding and most importantly, his friendship during my graduate studies at Columbia University. His passion and creativity for science has always encouraged me to expand my horizons and face new challenges. His warm and approachable personality has made working with him very enjoyable.

I would also like to thank my committee members Dr. Peter Schlosser, Dr. Vasilis Fthenakis, Dr. Gautam Dasgupta and Dr. Jie Yin for being part of my PhD committee and giving me suggestions and feedback on my work. Aside from the committee service, I would especially like to thank Dr. Gautam Dasgupta, for his guidance and advice over the past years. I highly respect him for his immense knowledge and great ability in teaching. I would like to thank Dr. Ngai Yin Yip and Dr. Athanasios Bourtsalas, for their advice and feedback regarding the 3rd year oral exam and the 4th year proposal, respectively. I would like to thank Dr. Klaus Lackner and his student Xiaoyang Shi for their scientific collaborations.

I am proud and consider myself very fortunate to be part of the Chen team and I would like to thank the past and present group members for their suggestions, support and friendship throughout my research and life. They are Xiaoyang Shi, Junfeng Xiao, Liangliang Zhu, Jun Xu, Xiangbiao Liao, Feng Hao and Yayun Zhang.

Finally, and most importantly, I would like to thank my wife Xin, for her support, encouragement, wisdom and unwavering love throughout this entire process. I thank my mom, Xiaoling, and my dad, Baocang, for being with me at every stage of my life. They have made many

sacrifices to ensure that I could lead a better life and get a better education. I could not be more thankful for being part of such an amazing family. It is to them that I dedicate this work.

Chapter 1 Introduction and Motivation

1.1 Why study low-dimensional materials?

In the past several decades, low-dimensional materials have attracted much interest from both the experimental and theoretical viewpoints. They refer to those materials in which at least one of the three physical dimensions constrained to the nanometer scale. Owing to the quantum confinement effect, low-dimensional materials have exhibited a kaleidoscope of fascinating phenomena and unusual physical and chemical properties, underpinning many novel applications. Typical examples of low-dimensional materials (see Figure 1.1) are zero-dimensional (0D) fullerenes, one-dimensional (1D) nanotubes, and two-dimensional (2D) nanosheets, which will be briefly introduced in the following sections.

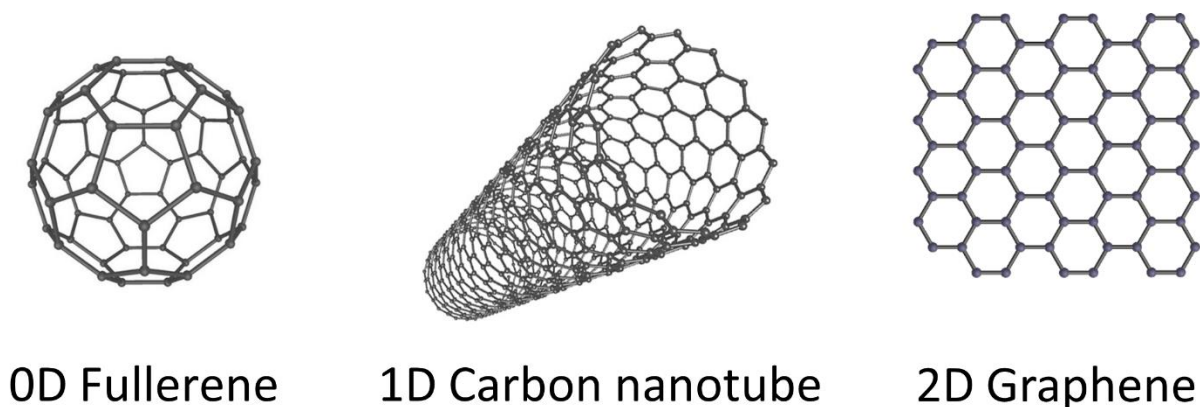


Figure 1.1 Schematic illustration of the 0D fullerene, 1D carbon nanotube and 2D graphene.

1.1.1 Zero-dimensional materials

The discovery of 0D fullerene¹ (C_{60}) in 1985 started the era of carbon nanomaterials. C_{60} is a closed carbon cage formed by 20 hexagons and 12 pentagons, resembling a tiny soccer ball.

Fullerene C_{60} has had a profound impact throughout science. For example, the fabrication of a single-molecule transistor made from C_{60} ² and the discovery of superconductivity in a single- C_{60} transistor.³ However, C_{60} has not enjoyed a great deal of success in practical applications, partly due to the high cost. The discovery of 0D fullerene directly led to the research in 1D carbon nanotubes.

1.1.2 One-dimensional materials

1D carbon nanotubes (CNTs) were discovered in 1991 by Sumio Iijima.⁴ They are hollow cylindrical forms of fullerenes, with either closed or open tips. Perfect CNTs composed of carbon atoms bonded in a hexagonal lattice except at their tips. The exceptional mechanical, electrical and thermal properties of CNTs make them ideal candidates for many different applications. For example, semiconducting CNTs have been used in field-effect transistors based chemical sensors,⁵ metallic CNTs have been used as electrodes for electrocatalysis⁶ and CNTs have found their way into bulk composite materials with improved mechanical performance.⁷ Nanocapsules self-assembled by CNTs can be ideal vehicles for drug delivery, since CNTs are non-immunogenic⁸ and can be functionalized.^{9–12} In Chapter 6, we show that one-end-open carbon nanotubes with proper radius difference can coaxially self-assemble into a stable nanocapsule, underpinning potential applications in nano-reactors, drug-delivery, etc.

1.1.3 Two-dimensional materials

In 2004, the isolation of graphene,¹³ a single layer of graphite, opened the field of two-dimensional materials. Graphene is composed of a single layer of carbon atoms densely packed in a 2D honeycomb lattice. Electrons travelling inside graphene behave like massless relativistic particles, leading to peculiar properties such as the anomalous quantum Hall effect¹⁴ and the

absence of localization effects.¹⁵ Many remarkable properties of graphene, such as high electron mobility at ambient temperature ($200,000 \text{ cm}^2/\text{V s}$),^{16,17} exceptional mechanical properties including Young's modulus of 1 TPa ¹⁸ and superior thermal conductivity ($5000 \text{ W}/(\text{m K})$)¹⁹ have been reported. Owing to its remarkable properties, the potential applications of graphene include high-speed electronics,²⁰ optical devices,²¹ chemical sensors,²² energy harvesting and storage^{21,23,24} and composite structural materials,²⁵ etc. The success of graphene has inspired the exploration of a whole family of 2D materials including the 2D insulator boron nitride (BN),^{26–28} 2D semiconductor molybdenum disulfide (MoS_2)^{26,29,30} and recently, phosphorus monolayer, i.e. phosphorene.^{31,32} Owing to its tunable band gap and high carrier mobility, phosphorene holds great potential in electronic and optoelectronic applications.^{31,33–36}

Although *ab initio* methods can accurately describe the electronic structure of phosphorene, they are limited to small systems (several hundreds of atoms) with short time scales (picoseconds). On the other hand, molecular dynamics simulations powered by non-reactive force fields are able to reach much larger scale with much longer time, but they are not suitable to describe states far from equilibrium and unable to model chemical reactions. A computational tool that can bridge this gap is therefore highly desirable. In Chapter 2, we develop a parameter set of ReaxFF for P/H, which provides an accurate description of the chemical and mechanical properties of pristine and defected black phosphorene.

Despite tremendous success has been achieved in the study of 2D materials, their practical applications are still very limited. Graphene, with an excellent carrier mobility, has zero band gap, which limits its further electronic and optoelectronic applications. The MoS_2 has sizeable band gap, but lower carrier mobility. Recently isolated phosphorene combines a sizeable and tunable band gap with high carrier mobility, but it degrades upon exposure to air. New low-dimensional

materials with novel properties are still highly desirable. In this thesis, we propose two new stable 2D crystals, S_3N_2 and P_2S_3 , underpinning potential applications in 2D electronics and optoelectronics.

1.1.4 Applications of low-dimensional materials in energy and environmental engineering

Although the production of graphene with few defects by mechanical exfoliation has led to the rapid development of graphene research, this method is not applicable to the majority of applications which require larger quantities of graphene. Meanwhile, the issues of poor dispersion, sheet defects, restacking and multilayer thickness hinder the full realization of graphene's potential, including electronic and high surface area properties.³⁷ Recently, graphene aerogel, a 3D porous material formed by the assembly of 2D graphene flakes have been extensively studied. Graphene aerogels exhibits high conductivity and reliable long range order as well as high surface area and accessible pore volume at extremely low density. As a result, graphene aerogels hold promise for many applications in catalysis,^{38–40} gas adsorption⁴¹ and energy storage.^{42,43}

To fight the climate change in the 21st century, carbon neutrality is far from being enough. The development of carbon negative technologies, e.g. direct air capture of CO_2 , is urgent.⁴⁴ The major challenge of developing an efficient absorbent for air capture of CO_2 is not how to absorb CO_2 , but how to release it with very low energy cost. This essentially requires a reversible chemical reaction that can be triggered by a simple environmental variable. Lackner et al.⁴⁵ discovered that an anionic exchange resin (IER) washed by carbonate solution can efficiently absorb CO_2 from ambient air when it is dry, while release CO_2 when it is wet, as shown in Figure 1.2.

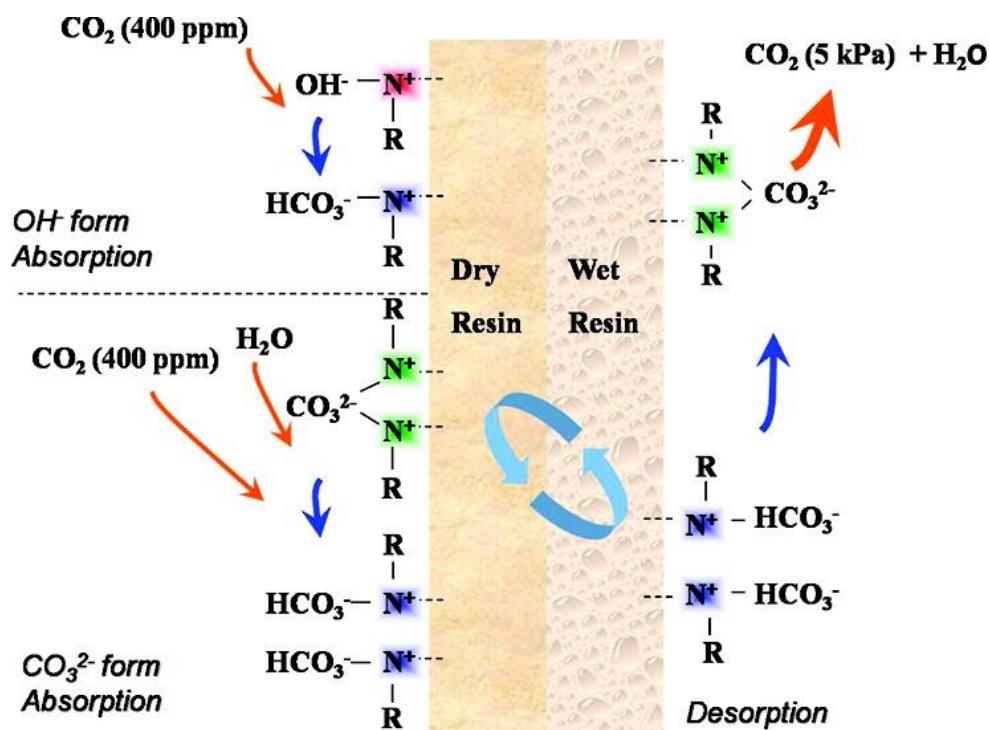


Figure 1.2 Humidity swing sorbent for CO₂ capture directly from ambient air.⁴⁶

Graphene aerogel, with extremely high specific surface area and accessible pore volume at extremely low density, can be an ideal sorbent for CO₂ air capture driven by humidity swing. Designing efficient sorbent for CO₂ air capture requires a detailed understanding of both thermodynamic and kinetic characteristics of the hydrolysis of CO₃²⁻ in nanoscale hydrated clusters, which is introduced in Chapter 5.

1.2 Fundamental challenges of research in low-dimensional materials

Three fundamental challenges of research in low-dimensional materials are:

- 1) Develop new computational tools to accurately describe the properties of low-dimensional materials with low computational cost.
- 2) Predict and synthesize new low-dimensional materials with novel properties.

- 3) Reveal new phenomenon induced by the interaction between low-dimensional materials and the surrounding environment.

In this thesis, atomistic modelling methods have been applied to address these challenges (schematically illustrated in Figure 1.3).

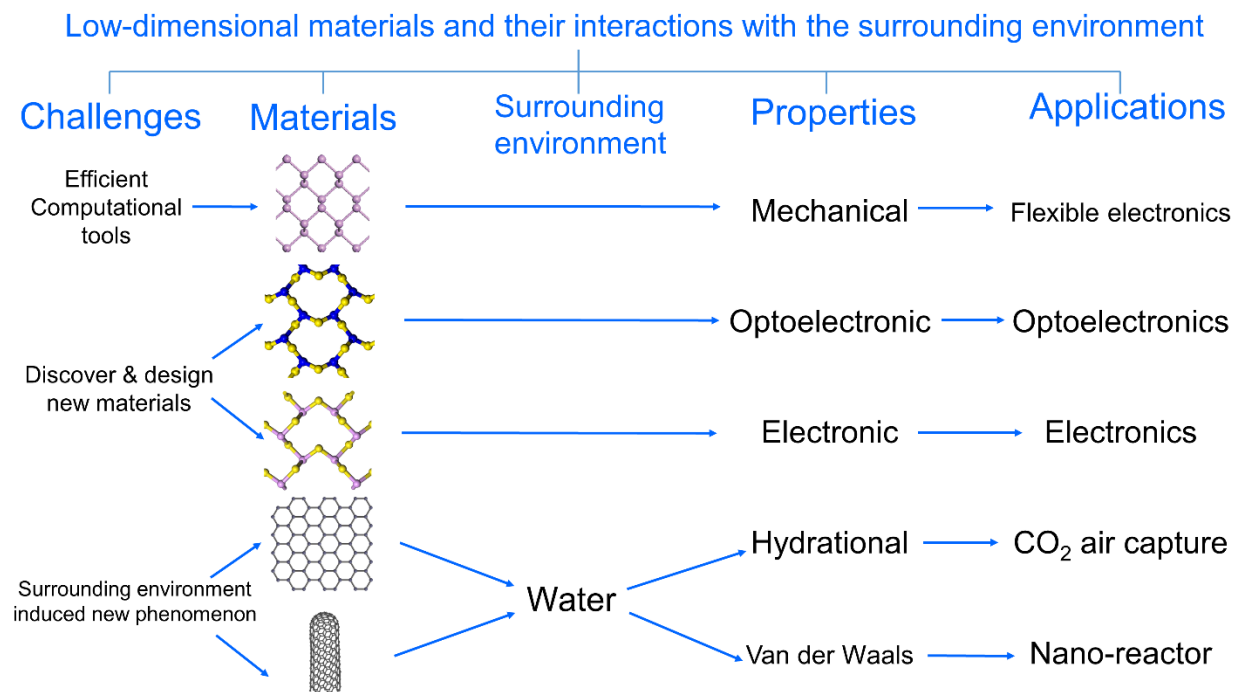


Figure 1.3 A schematic illustration of the motives and progresses of this thesis.

A number of discoveries and advances have been produced:

- 1) The parameterization and validation of a reactive force field for P/H systems, which provides an accurate description of the chemical and mechanical properties of pristine and defected black phosphorene.
- 2) The discovery of the first 2D crystal composed of N and S atoms, S₃N₂ for optoelectronic applications.
- 3) The discovery of the first 2D crystal composed of P and S atoms, P₂S₃ for electronic applications.

- 4) Revealing the catalytic effect of water in basic hydrolysis of CO_3^{2-} in hydrated clusters, providing valuable insights to designing efficient CO_2 air-capture sorbents.
- 5) One-end-open carbon nanotubes with proper radius difference can coaxially self-assemble into a nanocapsule with very high internal pressure (on the order of 1 GPa), underpinning potential applications in nano-reactors, drug-delivery, etc.

1.3 Atomistic modelling

Owing to the phenomenal increase in computational power of computers — as well as the development of efficient algorithms for theoretical predictions, computer simulation with atomistic detail is now a very prominent tool in material sciences, chemistry, physics and biology. In these fields, atomistic simulations have yielded unprecedented insight needed to predict material properties, can be used to design new materials and drugs, or to interpret experimental data.

The world we live in is composed of microscopic atoms in continual vibrational motion. Different atoms and their electronic interactions bring about everything in the material world. Therefore, the computational investigation of material properties and chemical reactions requires the description of atoms and the interactions between them. In a computational point of view, the electronic interactions between atoms can be treated either explicitly or implicitly. *Ab initio* methods provide accurate predictions over a wide range of systems by treating electronic interactions explicitly. Nonetheless, they are limited to small systems (several hundreds of atoms) with short time scales (picoseconds), since they are fairly computational intensive. For force field methods, electronic interactions are treated implicitly, trading precision for computational

efficiency. In this section, *ab initio* methods, force field methods and molecular dynamics will be reviewed in brief.

1.3.1 *Ab initio* methods

According to the Born-Oppenheimer approximation,⁴⁷ the movements of the electrons and the much heavier nuclei can be separated. Therefore, *ab initio* methods are based on solving the Schrödinger equation for the electrons of a system. The time-dependent Schrödinger equation has the form

$$\mathbf{H}\psi = E\psi \quad (1.1)$$

where \mathbf{H} is the electronic Hamiltonian, ψ is the many electron wave function and E is the total electron energy of the system.

The density functional theory (DFT) is one of the most successful *ab initio* methods for calculations of the electronic structure of atoms, molecules, and the condensed phases. The DFT is based on two theorems introduced by Hohenberg and Kohn in 1964,⁴⁸ and later extended by Kohn and Sham in 1965.⁴⁹

First, the ground-state energy E of an atomic system is shown to be a unique functional of the electron density $n(\mathbf{r})$,

$$E[n] = \int v(\mathbf{r})n(\mathbf{r})d\mathbf{r} + F[n] \quad (1.2)$$

where $v(\mathbf{r})$ is the external potential, and $F[n]$ is the functional containing the interactions of the electrons and the kinetic energy. According to the Hohenberg and Kohn theory, $F[n]$ can be separated into two terms

$$F[n] = \int \int \frac{n(\mathbf{r})n(\mathbf{r}')}{|\mathbf{r} - \mathbf{r}'|} d\mathbf{r}d\mathbf{r}' + G[n] \quad (1.3)$$

The first term on the right is the electron-electron Coulomb contribution and the second term $G[n]$ is a functional of the electron density. According to the Kohn and Sham theory, $G[n]$ has the form

$$G[n] = T[n] + E_{xc}[n] \quad (1.4)$$

where $T[n]$ is the kinetic energy of a non-interacting electron gas with density $n(\mathbf{r})$, and E_{xc} is the exchange-correlation energy. Its exact form is only known for the simplest case, i.e. the uniform electron gas. Suitable approximations have to be found for non-uniform electron densities. The simplest approximation of E_{xc} is the local density approximation (LDA),

$$E_{xc}^{\text{LDA}}[n] = \int n(\mathbf{r}) \varepsilon_{xc}[n(\mathbf{r})] d\mathbf{r} \quad (1.5)$$

where ε_{xc} is the exchange and correlation energy per particle of the uniform electron gas. The next step in approximating E_{xc} is to include the dependency of the gradient of the electron density at \mathbf{r} , leading to the generalized gradient approximation (GGA),

$$E_{xc}^{\text{GGA}}[n] = \int n(\mathbf{r}) \varepsilon_{xc}[n(\mathbf{r}), \nabla n(\mathbf{r})] d\mathbf{r} \quad (1.6)$$

1.3.2 Force field methods

Compared to *ab initio* methods, the force field methods are faster by several orders of magnitude, allowing the treatment of larger systems with longer time scales. In force field approaches, electrons are treated implicitly. The electronic interactions between atoms are taken into account by a force field, which includes energy terms to describe the interactions between atoms. Force fields can be broadly classified into two categories, namely non-reactive force fields and reactive force fields.

The potential functions of non-reactive force fields are relatively simple and are computationally inexpensive as compared to reactive force fields. A simple example of a non-reactive force field involves the use of harmonic potentials to represent bonds, angles, and torsions

and Coulomb's law for electrostatic interactions described by point charges and the Lennard-Jones (L-J) potential for van der Waals interactions. A typical non-reactive force field according to this scheme has the form,

$$\begin{aligned}
U_{ff}(\vec{r}) = & \sum_{bonds} k_i^{bond} (r_i - r_0)^2 + \sum_{angles} k_i^{angle} (\theta_i - \theta_0)^2 \\
& + \sum_{torsions} k_i^{torsion} [1 + \cos(n_i \phi_i + \delta_i)] \\
& + \sum_i \sum_{j \neq i} 4\epsilon_{ij} \left[\left(\frac{\sigma_{ij}}{r_{ij}} \right)^{12} - \left(\frac{\sigma_{ij}}{r_{ij}} \right)^6 \right] + \sum_i \sum_{j \neq i} \frac{q_i q_j}{\epsilon r_{ij}}
\end{aligned} \tag{1.7}$$

Owing to the simple form of potential functions, non-reactive force fields are easy to parameterize. They are able to represent the equilibrium structures of the atomistic systems with good accuracy, but they are not suitable to describe states far from equilibrium. In addition, they are unable to model chemical reactions, due to the requirement of breaking and forming bonds.

Unlike non-reactive force fields, reactive force fields include connection-dependent terms and hence are able to describe breaking and forming bonds. Some of the widely used reactive potentials are ReaxFF,⁵⁰ AIREBO⁵¹ and Tersoff.⁵² In our research we will be using the ReaxFF to study the chemical and mechanical properties of phosphorene.

ReaxFF adopts a bond order formulism to ensure smooth transition of bond dissociation and bond formation. The bond order BO_{ij} between a pair of atoms can be directly calculated from the interatomic distance r_{ij} as given in Eq. 1.8 and shown illustratively for a phosphorus-phosphorus bond in Figure 1.4.

$$\begin{aligned}
BO_{ij} = & BO_{ij}^\sigma + BO_{ij}^\pi + BO_{ij}^{\pi\pi} \\
= & \exp \left[p_{bo1} \left(\frac{r_{ij}}{r_0^\sigma} \right)^{p_{bo2}} \right] + \exp \left[p_{bo3} \left(\frac{r_{ij}}{r_0^\pi} \right)^{p_{bo4}} \right] + \exp \left[p_{bo5} \left(\frac{r_{ij}}{r_0^{\pi\pi}} \right)^{p_{bo6}} \right]
\end{aligned} \tag{1.8}$$

where r_0^σ , r_0^σ , r_0^σ are bond radii for single, double and triple bonds between particles i and j, p_{bo1} , p_{bo2} , p_{bo3} , p_{bo4} , p_{bo5} , p_{bo6} are bond order parameters. The effects of over-coordination and under-coordination are incorporated in ReaxFF by a bond order correction scheme, enabling ReaxFF to correctly adapt to the instantaneous configurations in the system.

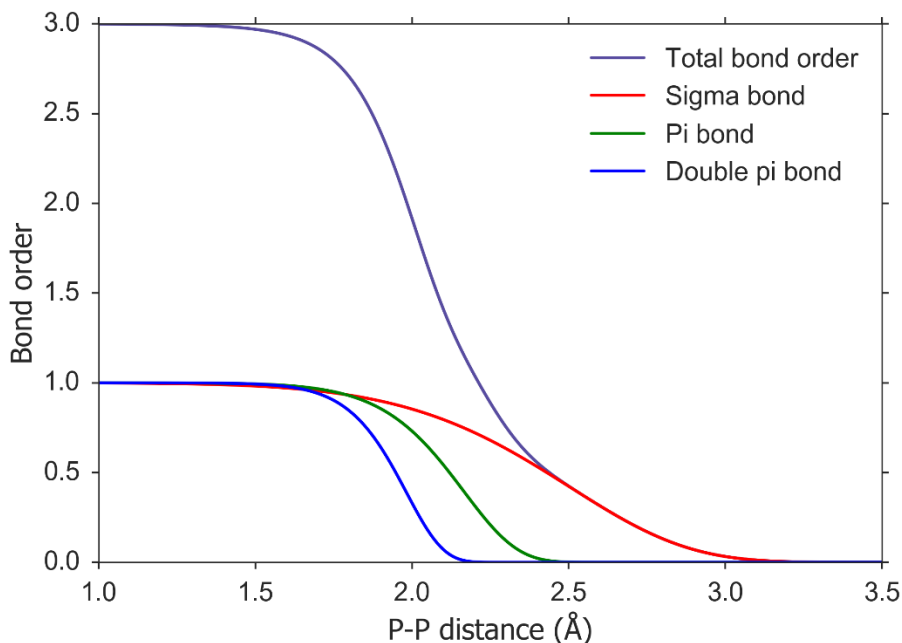


Figure 1.4 Interatomic distance dependency of the phosphorus-phosphorus bond order.

For a typical ReaxFF, the bond energies (U_{bond}) are corrected with over-coordination penalty energies (U_{over}) and under-coordination penalty energies (U_{under}). Energy contributions from valence angle (U_{val}) and torsion angle (U_{tor}) are incorporated. Dispersion interactions are represented by the van der Waals term (U_{vdW}). Energy contribution from Coulomb interactions ($U_{Coulomb}$) are taken into account between all atom pairs, where the atomic charges are calculated based on instantaneous configurations using the Electron Equilibration Method (EEM).⁵³ All energy terms except the last two are bond-order dependent and a detailed description of them can be found in Refs. ^{50,54,55}. The total energy is the sum of these energy terms, shown by

$$U_{system} = U_{bond} + U_{over} + U_{under} + U_{val} + U_{tors} + U_{vdW} + U_{Coulomb} \quad (1.9)$$

The time and length scales accessible to ReaxFF is schematically represented by Figure 1.5. ReaxFF bridges the gap between *ab initio* treatments of atomic systems and the non-reactive force field traditionally used in atomistic simulations. Owing to the complicated potential functions, ReaxFF is around 10-50 times slower than non-reactive force fields. Nevertheless, ReaxFF is still much faster than *ab initio* methods, enabling the simulation of reactive systems larger than 10^6 atoms at nanosecond time scales.

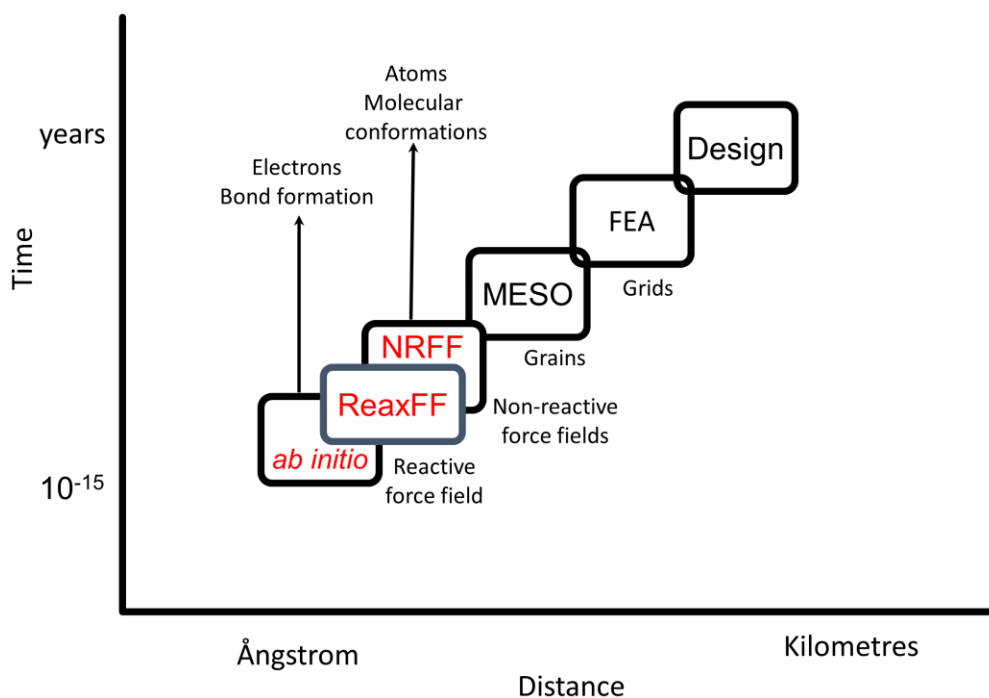


Figure 1.5 Hierarchy of computational methods on a time vs length scale.

1.3.3 Molecular dynamics

Molecular dynamics (MD) is a computer simulation approach for studying the time evolution of a system of interacting particles. The first MD simulation was performed by Alder

and Wainwright in the late 1950's to study the interactions of hard spheres.⁵⁶ MD simulations are widely applied today in chemical physics, molecular biology and material science.

In MD simulations, the trajectories of particles are generated by an integration of Newton's second law,

$$m \frac{d^2 \mathbf{r}}{dt^2} = -\nabla U(\mathbf{r}) \quad (1.10)$$

where m is the mass of a particle and $U(\mathbf{r})$ is the potential energy function. With molecular dynamics simulations, both thermodynamic properties and time dependent (kinetic) phenomenon can be studied.

In classical molecular dynamics, the potential energy function is represented by the force field (non-reactive or reactive). *Ab initio* molecular dynamics (AIMD) uses forces obtained from *ab initio* calculations, allowing chemical processes to be studied in an accurate and unbiased manner. However, AIMD is limited to smaller systems and shorter time scales, due to high computational cost. Details of MD simulations can be found elsewhere.⁵⁷⁻⁵⁹

1.4 Outline of dissertation

This PhD thesis contains 7 chapters, including Chapter 1 as an introduction of motivation and computational methods used throughout the thesis. In Chapter 2, the parameterization and validation of a ReaxFF for P and H is introduced. In Chapter 3, the discovery of a new S₃N₂ 2D material for optoelectronic applications is reported. Inspired by the discovery of S₃N₂, Chapter 4 presents the discovery of a new P₂S₃ 2D material for electronic applications. In Chapter 5, the catalytic effect of water in the hydrolysis of CO₃²⁻ in hydrated clusters is explored. Chapter 6 reports the molecular mechanism study of the self-assembly of one-end-open CNTs into

nanocapsules in water. In Chapter 7, concluding remarks and the introduction of future work are provided.

Chapter 2 Development of a Transferable Reactive Force Field of P/H Systems: Application to the Chemical and Mechanical Properties of Phosphorene

2.1 Introduction

In recent years, two-dimensional (2D) materials have attracted much interest because of their fascinating electronic,^{60,61} mechanical,¹⁸ optoelectronic,^{62,63} and chemical^{64,65} properties. The epic discovery of graphene opened up the possibility of isolating and studying the intriguing properties of a whole family of 2D materials including the 2D insulator boron nitride (BN),^{26–28} 2D semiconductor molybdenum disulfide^{26,29,30} and recently, 2D phosphorus, i.e. phosphorene.^{31,32} Single layer black phosphorus, i.e. phosphorene, was obtained in experiments in 2014.³² Because of its tunable band gap and a small hole effective mass, phosphorene holds great potential in electronic and optoelectronic applications.

Over the past decade, tremendous success has been achieved in the synthesis of 2D materials. However, the cycles of synthesis, characterization and test for 2D materials are slow and costly, which inspired the development of computational tools to design new 2D materials^{66–68} and to provide guidance for the fabrication of 2D devices.^{69–72} Although *ab initio* methods (such as density functional theory, DFT) provide accurate description of the electronic structure of 2D crystals, they are limited to small systems (several hundreds of atoms) with short time scales (picoseconds). To the contrary, molecular dynamics simulations powered by force fields are able to reach much larger scale with much longer time. To date, several force fields have been developed for black phosphorus.

A valence force field (VFF) for black phosphorus was first proposed in 1982 and used to study the elastic properties in black phosphorus.⁷³ More recently, Jiang *et al.*⁷⁴ developed a Stillinger-Weber (SW) potential for phosphorene based on the VFF model by fitting parameters to experimental phonon spectrum. In the SW potential, the energy parameters were taken from the VFF model, and geometrical parameters were derived analytically from the equilibrium state of individual potential terms. While both VFF model and SW potential have been used to describe phonons and elastic deformations, they are not suitable to describe states far from equilibrium.⁷⁵ Moreover, the SW potential strongly underestimated the Young's modulus of black phosphorene in the zigzag direction.⁷⁶ Due to its nonreactive nature, SW potential also has difficulty describing phosphorene with defects. An improved force field which balances accuracy and computational efficiency is therefore highly desirable. In 2001, van Duin *et al.* developed a reactive force field (ReaxFF) for hydrocarbons.⁵⁰ ReaxFF is a bond order interaction model, capable of handling bond breaking and forming with associated changes in atomic hybridization. Since its development, ReaxFF model has been applied to a wide range of systems.^{54,55,77–81} To the best of our knowledge, a ReaxFF model for phosphorene system is still lacking.

In this chapter, we develop a ReaxFF parameter set for P and H to describe the chemical and mechanical properties of the pristine and defected black phosphorene. ReaxFF for P/H is transferable to a wide range of phosphorus and hydrogen containing systems including bulk black phosphorus, blue phosphorene, hydrogenated phosphorene, phosphorus clusters and phosphorus hydride molecules. The ReaxFF parameters for P/H were fitted to a set of reference data generated by extensive *ab initio* calculations. The proposed ReaxFF for P/H provides a distinctive improvement in describing the thermomechanical properties the pristine and defected black phosphorene, as well as that of the phosphorene nanotubes (PNTs) over the SW potential. The

ReaxFF parameters for P/H presented here provide a first step in the development of a reactive force field description for the heterogeneous P systems.

2.2 Methodology

2.2.1 DFT calculations

The fitting data used for P/H systems was obtained from DFT calculations performed with the Cambridge series of total-energy package (CASTEP).^{82,83} For these calculations, ultrasoft pseudopotentials were used to describe the core electrons and the electron exchange-correlation effects were described by the Perdew–Burke–Ernzerhof (PBE)⁸⁴ generalized gradient approximation. In this work, the empirical dispersion correction scheme proposed by Grimme (D2)⁸⁵ was used in combination with the PBE functional. In computing the energies of phosphorus clusters, phosphorus hydride molecules and phosphorene with defects and adatoms, spin polarization was used to account for the energy contributions from magnetization. Periodic boundary conditions were used for all the calculations, with monolayer structures represented by a periodic array of slabs separated by a 15 Å thick vacuum region. A large 5×7 supercell of black phosphorene was adopted to study the effect of defects and adatoms. A plane wave cutoff of 520 eV was used to determine the self-consistent charge density. For condensed phases, the Brillouin zone integrations were performed with Monkhorst-Pack⁸⁶ mesh with 0.02 Å^{-1} k -point spacing. For cluster calculations, a cubic supercell of 20 Å (to ensure the interactions between clusters in adjacent cells is negligible) was used with the clusters or molecules placed at the center of the cell with the Brillouin zone sampled at the Γ point. All geometries were optimized by CASTEP using the conjugate gradient method (CG) with convergence tolerances of a total energy within $5.0 \times 10^{-6} \text{ eV atom}^{-1}$, maximum Hellmann–Feynman force within 0.01 eV Å^{-1} , maximum ionic

displacement within 5.0×10^{-5} Å, and maximum stress within 0.01 GPa. For black phosphorene, the stress-strain responses in the armchair and zigzag directions were calculated using the method described in the references^{87,88} with CASTEP. The CASTEP calculations showed good agreement with previous theoretical values for a variety of phosphorene properties: lattice constants,³² Young's moduli and Poisson's ratios in the armchair and zigzag directions,⁸⁹ formation energies of defects⁹⁰ and binding energies of adatoms.⁹¹ And the calculated lattice constants of bulk black phosphorus agreed well with experimental values.⁹²

2.2.2 ReaxFF

The ReaxFF model^{50,54,77} is a bond order interaction model. For ReaxFF, the interatomic potential describes chemical reactions through a bond order framework, in which the bond order is directly calculated from interatomic distances. Within the bond order framework, the electronic interactions (i.e. the driving force of the chemical bonding) are treated implicitly, allowing the method to simulate chemical reactions without expensive quantum chemical calculations. Typical empirical force field (EFF) potentials adopt empirical equations to describe the bond stretching, bond bending, and bond torsion events, with additional expressions to handle the van der Waals (vdW) and Coulomb interactions. These EFF potentials require a user-specified connectivity table, while ReaxFF is able to calculate the atom connectivity on the fly, which distinguishes ReaxFF from conventional EFF potentials since the breaking and forming of bonds can be captured during MD simulations.

For a ReaxFF description of P/H systems, the bond energies (U_{bond}) are corrected with over-coordination penalty energies (U_{over}). Energy contributions from valence angle (U_{val}) and torsion angle (U_{tor}) are included. Dispersion interactions are described by the combination of the original van der Waals term (U_{vdW}) and low-gradient vdW correction term (U_{lgvdW}).⁵⁵ The energy

contribution from Coulomb interactions ($U_{Coulomb}$) is taken into account between all atom pairs, where the atomic charges are calculated based on connectivity and geometry using the Electron Equilibration Method (EEM).⁵³ All energy terms except the last three are bond order dependent and a detailed description of them (except U_{60cor}) can be found in Refs. ^{50,54,55}. The total energy is the summation of these energy pieces, shown by

$$U_{system} = U_{bond} + U_{over} + U_{val} + U_{60cor} + U_{tors} + U_{vdW} + U_{lgvdW} + U_{Coulomb} \quad (2.1)$$

The stability of P₄ cluster and the instability of larger phosphorus clusters has been an ongoing puzzle for several decades.⁹³ Phosphorus is often expected to favor valence angles near 101 °.⁹⁴ If this is true, the strain energy of bonds in P₄ cluster (with 60 ° valence angles) should make it unstable. In QM calculations, this problem was resolved by including the effect of d-orbitals.⁹⁵ In order to address the stability of the P₄ cluster (and other phosphorus clusters with valence angles near 60 °), we added a 60 ° angle correction term to Eq. 2.1.*

$$U_{60cor} = -p_{cor1} \cdot f_1(BO_{ij}) \cdot f_2(BO_{jk}) \cdot \exp \left[-p_{cor2} * (\theta_{60} - \theta_{ijk})^2 \right] \quad (2.2a)$$

$$f_1(BO_{ij}) = 1 - \exp(-p_{val3} \cdot BO_{ij}^{p_{cor3}}) \quad (2.2b)$$

$$f_2(BO_{jk}) = 1 - \exp(-p_{val3} \cdot BO_{jk}^{p_{cor3}}) \quad (2.2c)$$

In section 3.2.2, it is demonstrated that the accuracy of cluster formation energies was significantly improved by the addition of the 60 ° angle correction term.

* Note that, for the simulation of P/H systems with the 60 ° angle correction, one needs to use the force field file with 60 ° angle correction and recompile the LAMMPS package with our modified source file, *reaxc_valence_angles.cpp*. We verified that the 60 ° angle correction term would only affect the properties of P/H systems with valence angles near 60 °. Therefore, for the simulation of condensed phases (either pristine or defected) and phosphorus hydride molecules, the original software of LAMMPS package can be used with the force field file without 60 ° angle correction. Because the lgvdW term is included in the ReaxFF, the “pair_style” command in the input file of LAMMPS should be: pair_style reax/c NULL lgvdw yes.

The LAMMPS code⁹⁶ was used to perform MD calculations for the tensile behavior for the black phosphorene of dimension $27.5 \times 25.8 \text{ \AA}$ at 1.0 K and 300.0 K. Periodic boundary conditions were employed in both the zigzag and armchair directions. The equation of motion was solved with a velocity Verlet algorithm, using a time step of 1.0 fs, which led to stable dynamics trajectories. The system was thermalized to steady state with the NPT (constant number of particles, constant pressure, and constant temperature) ensemble for 50 ps by the Nosé-Hoover thermostat.^{97,98} Subsequently, the black phosphorene was stretched in zigzag or armchair direction at a strain rate of 10^9 s^{-1} , and the stress in the lateral direction was fully relaxed. In computing the stress, the inter-layer spacing of 5.24 \AA was used as the thickness of the black phosphorene. Young's modulus and Poisson's ratio were calculated from the stress-strain curve in the strain range $[0, 0.01]$. Following the same procedure of calculating the stress-strain curve for the defect-free black phosphorene, the MD calculations for defected phosphorene under tensile strain were conducted for the black phosphorene of dimension $27.5 \times 25.8 \text{ \AA}$ at 1.0 K with one defect (in the form of single vacancy, double vacancy or Stone-Wales defect). For the stability analysis of PNTs, each PNT with the length of 10 supercells is equilibrated to a thermally stable state under NPT ensemble at a given temperature (from 0-800 K).

2.3 DFT training of force field

The ReaxFF parameters for P/H systems were optimized using a modified version of the evolutionary algorithms (EA) software suite OGOLEM,^{99,100} which is able to globally optimize ReaxFF parameter sets with high parallel efficiency. Based on DFT calculations for bulk black phosphorus, pristine and defected black phosphorene, blue phosphorene, phosphorus hydride molecules and phosphorus clusters, ReaxFF parameters were generated for P-P and P-H bond

energies, P-P-P, H-P-P and H-P-H valence angle energies and for H-P-P-P and H-P-P-H torsion energies.

The parametrization of ReaxFF for P/H systems consisted of following steps:

- (i) The training set of DFT data points was built for crystals, clusters and phosphorus hydride molecules. For crystal phases, the energy-volume relationship of the black phosphorus crystal and the energy-area relationship of both black and blue phosphorene were deduced. The bond dissociation profiles of P-P bonds in the P_2H_4 and P_2H_2 molecules, and of P-H bonds in the PH_3 molecules were included. Energy profiles for angle distortion of P-P-P in the P_3H_5 molecule, of H-P-P in the P_2H_4 molecule, and of H-P-H in the PH_3 molecule were added. In these energy profiles, only the lowest-energy states (singlet, triplet or quintet depending on geometry) were included. The Mulliken charges for the phosphorus hydride molecules were added to the training set. A minimum number of terms in Eq. 2.1 were selected (starting with $U_{bond}, U_{over}, U_{val}, U_{vdW}, U_{Coulomb}$). The parameters were fitted to the training set using OGOLEM.^{99,100}
- (ii) The torsion angle term (U_{tor}), low gradient correction term (U_{lgvdW}), and 60 ° angle correction term (U_{60cor}) were added to the total energy function to obtain a refined fit to the training set. Energy profiles for torsion distortion of H-P-P-H in the P_2H_4 molecule and of H-P-P-P in the P_4H_2 molecule were included. Energies and geometries of phosphorene with different types of defects were added to the training set.
- (iii) The global optimized parameters were validated by the comparison of properties calculated by ReaxFF to experimental data and DFT data.

2.4 Parameterization and validation of ReaxFF

Our final fitted, global optimized ReaxFF for P/H systems is given in Tables 2.1-2.7. The potential form is given in Eq. 2.1 (a detailed description of all terms can be found in Refs. ^{50,54,55}). Unless otherwise stated, all ReaxFF results in the following discussion refer to our global optimized ReaxFF parameter set.

Table 2.1

Atom parameters for P and H

	Bond radii				Coulomb parameters			Bond order correction			Valence Angle	
	r_σ (Å)	r_π (Å)	$r_{\pi\pi}$ (Å)	p_{ovun2}	η (eV)	χ (eV)	γ (Å)	p_{boc3}	p_{boc4}	p_{boc5}	p_{val3}	p_{val5}
P	2.1199	1.9507	1.8354	-2.0858	8.5658	6.3467	0.4060	15.5783	11.8556	2.8491	4.8954	1.6350
H	0.7853			-15.7683	7.4366	5.3200	1.0206	3.3517	1.9771	0.7571	2.1488	2.8793

For H, parameters from Ref. ¹⁰¹ were used. Definitions of the individual ReaxFF parameters in this table and Tables 2.2-2.6 can be found in Refs. ^{50,54,55}.

Table 2.2

VdW parameters and low-gradient vdW correction parameters for P and H

	van der Waals parameters					lgvdW			
	r_{vdW} (Å)	ϵ (kcal/mol)	α	γ_{vdW} (Å)	r_{core} (Å)	ϵ_{core} (kcal/mol)	α_{core}	r_{lg} (Å)	c_{lg}
P	2.3355	0.0887	9.5120	7.6148	2.6552	0.0743	15.5028	2.1233	5066.5788
H	1.5904	0.0419	9.3557	5.0518	2.0000	0.0000	1.0000	1.9593	101.0453

For H, parameters from Ref. ¹⁰¹ were used.

Table 2.3

Van der Waals and bond radius parameters for the P-H bond

r_σ	r_{vdW}	ϵ	γ_{vdW}
(Å)	(Å)	(kcal/mol)	(Å)

P-H	1.4319	1.5940	0.1064	10.3773
-----	--------	--------	--------	---------

Table 2.4

Bond energy and bond order parameters for the P-P, P-H and H-H bonds

Bond	D_e^σ (kcal/mol)	D_e^π (kcal/mol)	$D_e^{\pi\pi}$ (kcal/mol)	p_{be1}	p_{be2}	p_{ovun1}	p_{bo1}	p_{bo2}	p_{bo3}	p_{bo4}	p_{bo5}	p_{bo6}
P-P	52.2711	23.4911	20.0346	0.4917	1.4218	0.7412	-0.2457	7.5884	-0.2226	13.6705	-0.2395	17.8190
P-H	124.0512			-0.3732	5.9712	0.5862	-0.1003	5.6515				
H-H	156.0973			-0.1377	2.9907	0.8240	-0.0593	4.8358				

For the H-H bond, parameters from Ref. ¹⁰¹ were used.

Table 2.5

Valence angle parameters.

Valence angle	θ_{00} (degree)	k_a (kcal/mol)	k_b (1/rad) ²	p_{v1}	p_{v2}
P-P-P	81.1291	81.4496	0.5055	0.1993	1.0534
H-P-P	87.7897	48.0234	1.1576	2.4234	1.6028
H-P-H	91.5071	16.1001	2.6120	0.5531	1.0740

Table 2.6

60° angle correction parameters.

60° angle correction	θ_{60} (degree)	p_{cor1} (kcal/mol)	p_{cor2} (1/rad) ²	p_{cor3}
P-P-P	60	16.6700	150.0000	1.0534

The parameters of 60° angle correction for P-P-P are designed to improve the description of phosphorus clusters with ReaxFF, explained in section 2.2.

Table 2.7

Torsion angle parameters

General parameters		Torsion angle	V_1	V_2	V_3	p_{tor1}
p_{tor2}	9.6260					
p_{tor3}	9.7452	H-P-P-P	-0.0137	46.5023	0.7269	-3.2753
p_{tor4}	4.1021	H-P-P-H	-0.1595	49.6094	0.5875	-2.0714

2.4.1 Relative stabilities of bulk black phosphorus, black and blue phosphorene

For ReaxFF to accurately describe phosphorus in the condensed phase, descriptions for different crystalline phases should be included in the DFT training set. Relative stabilities of the black phosphorus crystal as a function of unit cell volumes and relative stabilities of the both black and blue phosphorene as a function of unit cell in-plane areas were calculated. In general, the ReaxFF model gives a good description of lattice parameters of all three crystal phases (see Table 2.8) and shows a good consistency of the crystal structures of these crystal phases (see Figure 2.1).

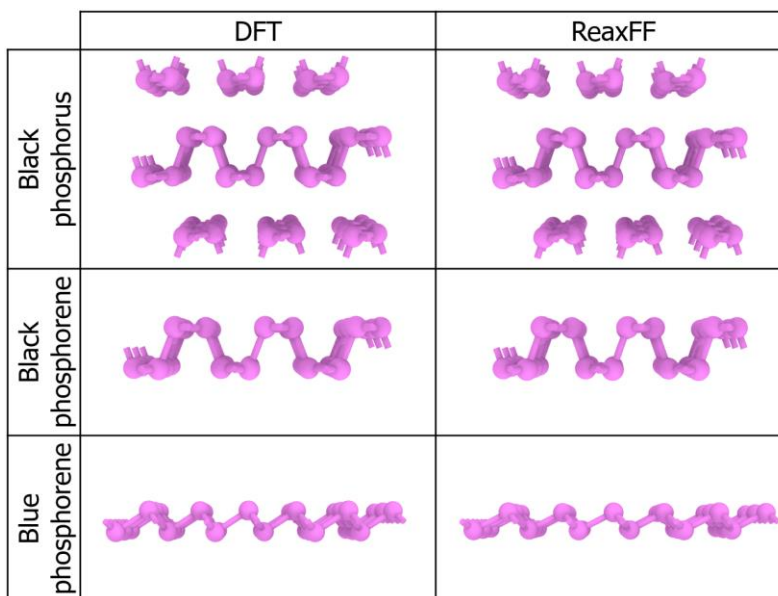


Figure 2.1 Crystal structures of bulk black phosphorus, black phosphorene and blue phosphorene calculated by DFT and ReaxFF.

Table 2.8

DFT results and ReaxFF results (at 0 K) of bulk black phosphorus, black phosphorene and blue phosphorene compared to experimental obtained data.

Structure	Lattice parameter	DFT (Å)	ReaxFF (Å)	Experiment ⁹² (Å)
Bulk black phosphorus	<i>a</i>	3.30	3.46	3.31
	<i>b</i>	4.40	4.29	4.38
	<i>c</i>	10.43	10.43	10.48
Black phosphorene	<i>a</i>	3.28	3.46	
	<i>b</i>	4.56	4.31	
Blue phosphorene	<i>a</i>	3.26	3.43	
	<i>b</i>	5.65	5.96	

In particular, the DFT and ReaxFF results of cohesive energies are compared to SW results and experimental data in Table 2.9. The equilibrium cohesive energy of bulk phosphorus used in

the fitting procedure was the experimental data¹⁰² of -3.26 eV rather than the value computed from DFT (-3.43 eV). ReaxFF predicts a black phosphorus cohesive energy of -2.91 eV. The cohesive energy of black phosphorene calculated by ReaxFF is -2.84 eV, which slightly underestimates the DFT result of -3.35 eV. Still, ReaxFF provides a much better prediction of cohesive energy of phosphorene than that of SW potential, which underestimates the cohesive energy of phosphorene by an order of magnitude. ReaxFF are able to correctly reproduce the relative order of stability of three crystal phases (shown in Table 2.9). In Figure 2.2(a) and Figure 2.2(b), the results from ReaxFF correctly describe the relative stabilities of bulk black phosphorus for a broad range of cell volume, as well as that of black phosphorene for a broad range of cell area. In the training set, not all the data can be fitted equally well. For blue phosphorene (Figure 2.2(c)), ReaxFF slightly overestimates the in-plane area of the unit cell, leading to a small offset of the energy profile of the relative stability. Given that no existing force field can describe the properties of blue phosphorene, the present ReaxFF may represent a major step forward.

Table 2.9

DFT results versus ReaxFF results of cohesive energies compared to SW results and experimental data

Structure	Property	DFT	ReaxFF	SW ⁷⁴	Experiment ¹⁰²
Bulk black phosphorus	$E_{cohesive}(\text{bulk})/\text{eV}$	-3.43	-2.91		-3.26
Black phosphorene	$E_{cohesive}(\text{black})/\text{eV}$	-3.35	-2.84	-0.54	
	$E_{cohesive}(\text{black}) - E_{cohesive}(\text{bulk}) / (\text{kcal/mol})$	1.94	1.58		
Blue phosphorene	$E_{cohesive}(\text{blue}) - E_{cohesive}(\text{bulk}) / (\text{kcal/mol})$	3.00	2.15		

$E_{cohesive}(\text{bulk})$, $E_{cohesive}(\text{black})$ and $E_{cohesive}(\text{blue})$ are the cohesive energies of bulk black phosphorus, black phosphorene and blue phosphorene, respectively.

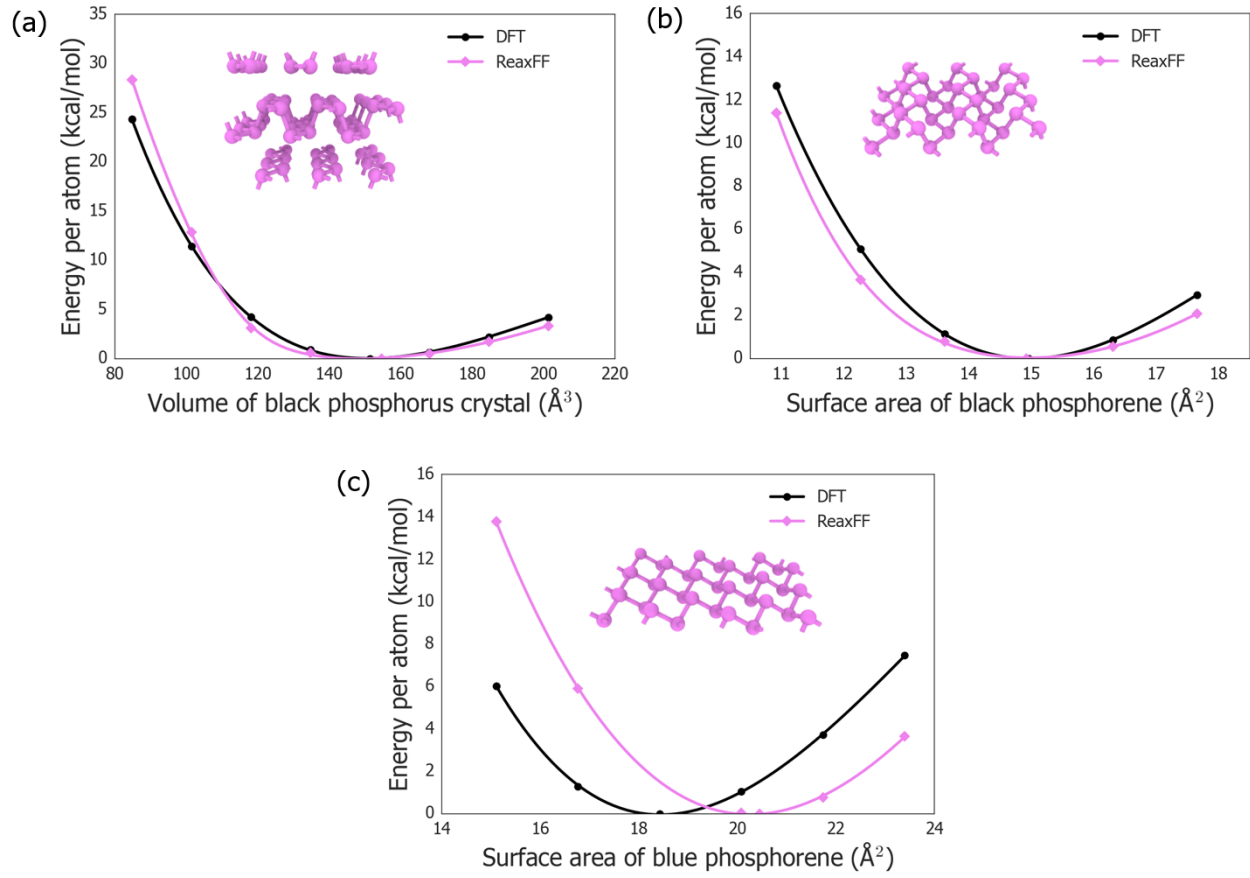


Figure 2.2 Relative stabilities of (a) bulk black phosphorus for a broad range of unit cell volume, (b) black phosphorene for a broad range of in-plane unit cell area, (c) blue phosphorene for a broad range of in-plane unit cell area.

2.4.2 Relative stabilities of phosphorus clusters

For ReaxFF to provide accurate description of phosphorus in clusters, the geometries and formation energies of P clusters of sizes 4,5,6 and 8 atoms are included in the training set. The formation energies per atom of clusters, E_{cf} , defined by

$$E_{cf} = E_c/n - E_{cohesive}(\text{bulk}) \quad (2.3)$$

where E_c is the energy of the relaxed phosphorus cluster with n atoms, $E_{cohesive}(\text{bulk})$ is the cohesive energy of the bulk black phosphorus. As can be seen from Figure 2.3, ReaxFF is capable of providing a very good description of the geometries of P clusters. Table 2.10 shows that the cluster formation energies per atom calculated by ReaxFF with 60 ° correction agree well with the DFT results. It is intriguing that a simple 60 ° angle correction term is able to provide such a notable improvement in terms of cluster formation energies.

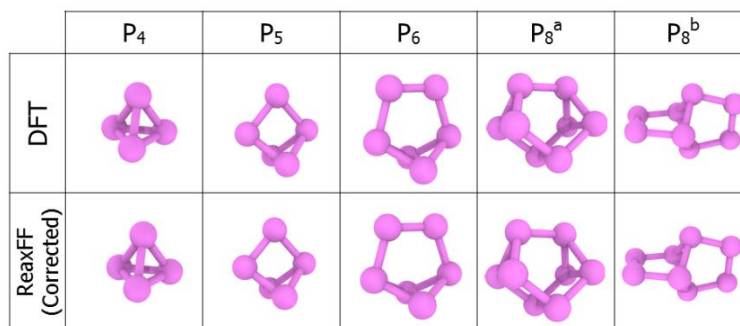


Figure 2.3 Structures of phosphorus clusters from DFT and ReaxFF with the 60 ° correction.

Table 2.10

Formation energy per atom of phosphorus clusters calculated by ReaxFF (with or without 60 ° correction) compared to DFT results.

Cluster	Formation energy per atom		
	(kcal/mol)		
	DFT	ReaxFF	ReaxFF (60 ° correction)
P ₄	7.6	56.9	7.6
P ₅	14.3	30.7	13.1
P ₆	11.3	25.1	9.7
P ₈ ^a	8.2	18.5	6.2
P ₈ ^b	12.7	11.1	11.8

2.4.3 Potential energy curves for phosphorus hydride molecules

Data for selected phosphorus hydride molecules was also included in the training set to train the P-H interactions and to enhance the transferability of the ReaxFF for P/H systems. To include DFT data for P-H, P-H bonds, dissociation profiles were determined from DFT calculations for phosphine, P_2H_2 and P_2H_4 molecules. The bond dissociation profiles were generated from the equilibrium geometries of these molecules by changing the bond length from the equilibrium value while allowing other structural parameters to relax, which are shown in Figure 2.4(a-c). Only the lowest-energy states (singlet, triplet or quintet depending on geometry) were included in bond dissociation profiles. The DFT and ReaxFF curves are shown in Figure 2.4(a-c).

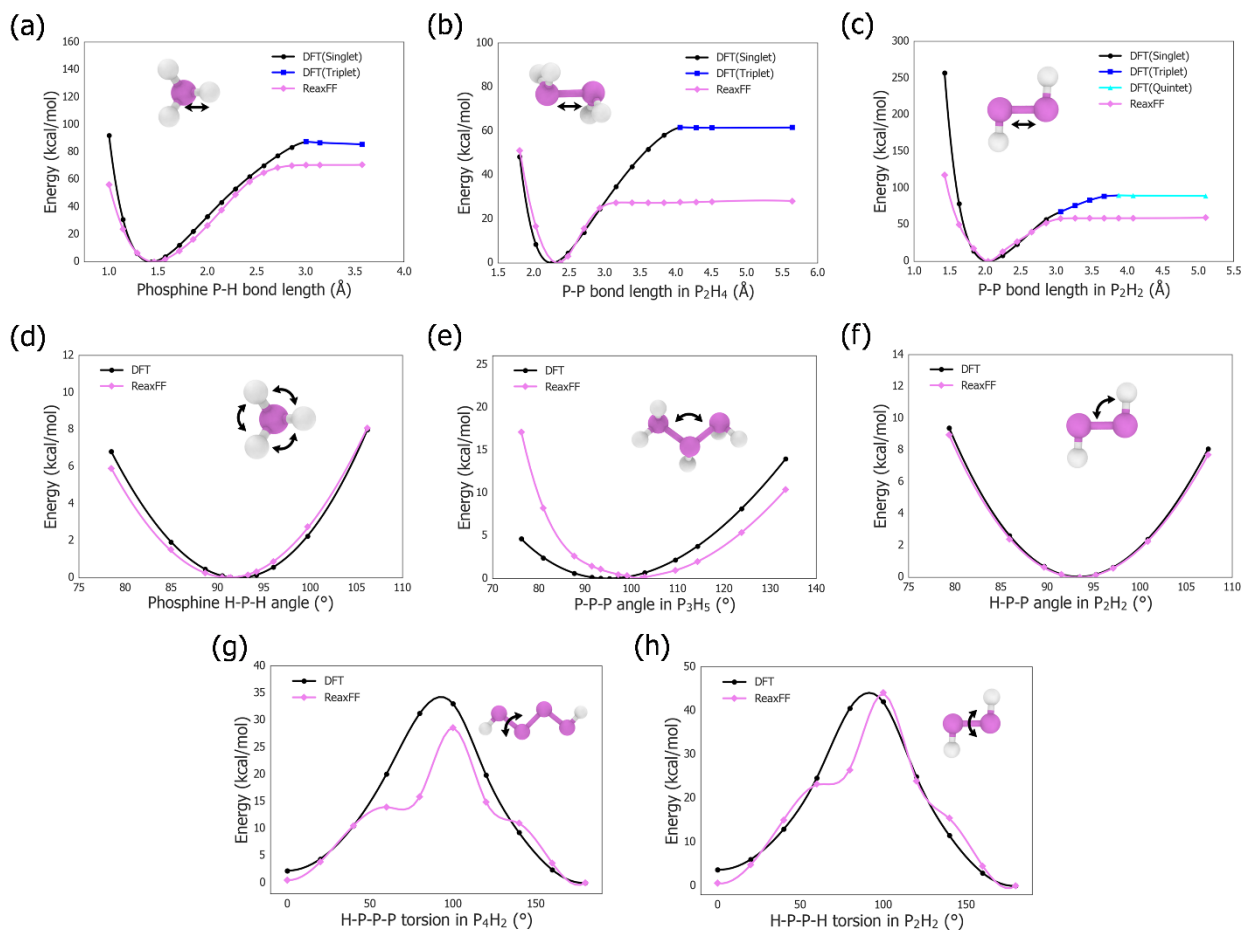


Figure 2.4 DFT and ReaxFF potential energy curves for: (a) dissociation of a P-H bond in phosphine, (b) dissociation of a P-P bond in the P_2H_4 molecule, (c) dissociation of a P-P bond in the P_2H_2 molecule, (d) angle distortion of H-P-H in phosphine, (e) angle distortion of P-P-P in the P_3H_5 molecule, (f) angle distortion of H-P-P in the P_2H_2 molecule, (g) torsion distortion of H-P-P-H in the P_2H_4 molecule and of H-P-P-P in the P_4H_2 molecule.

To include DFT data for P-P-P, H-P-P and H-P-H valence angles, P_3H_5 , P_2H_2 and phosphine molecules were used, respectively. Following the same procedure of constructing the bond dissociation profiles, P_3H_5 , P_2H_2 and phosphine molecules were geometry optimized to create reference states. Afterwards the valence angles were modified while other structural parameters were optimized. The resulting angle distortion curves are shown in Figure 2.4(d-f).

Energy profiles for torsion distortion of H-P-P-H in the P_2H_4 molecule and of H-P-P-P in the P_4H_2 molecule were also included in the training set. The torsion distortion curves were generated from the equilibrium geometries of these molecules by changing the relevant torsion angle from the equilibrium value while allowing other structural parameters to relax, which are shown in Figure 2.4(g-h).

In Figure 2.4(a, d, f, g, h), it is visible that the interactions between phosphorus and hydrogen atoms in phosphorus hydride molecules are well reproduced with ReaxFF. For the interactions between phosphorus atoms in phosphorus hydride molecules (see Figure 2.4(b, c, e)), agreement between the ReaxFF and DFT results is not perfect, because the crystal phases of phosphorus were prioritized over the phosphorus hydride molecules in ReaxFF. The depth of the ReaxFF potential well in Figure 2.4(b) is shallow, in order to offset the errors in cohesive energy for bulk black phosphorus (cf. Table 2.9) and the ultimate strength of black phosphorene in zigzag direction (cf. Figure 2.7).

2.4.4 Defects for black phosphorene

Properties and applications of 2D materials are strongly affected by defects,¹⁰³ which are generally induced by irradiations of ion or electron.¹⁰⁴ Defect engineering has emerged as an important approach to modulate the properties of 2D materials. Thus the accurate description of behavior of different types of defects in phosphorene is critical for ReaxFF of P/H systems. The structures and formation energies of single vacancy (SV), double vacancy (DV) and Stone-Wales (SW) defects are included in the training set. The defect formation energy, E_{df} , defined by

$$E_{df} = E_d - E_{cohesive}(\text{black}) \cdot n \quad (2.4)$$

where E_d is the energy of the defected phosphorene (geometry optimized) with n phosphorus atoms, $E_{cohesive}(\text{black})$ is the energy per atom of the black phosphorene. Figure 2.5 shows that

ReaxFF performs very well in predicting defects geometries of all three types with respect to DFT calculations, whereas SW potential fails to predict the structure of all three type of defects. From Table 2.11, ReaxFF provides a good description of the defect formation energy of single vacancy and double vacancy in phosphorene, as well as the relative stability between single vacancy and double vacancy. The formation energy of Stone-Wales defect is overestimated by 36% by ReaxFF. By comparison, for SW potential, the formation energies of single and double vacancy are seriously underestimated (see Table 2.11) and the Stone-Wales defect is unstable (see Figure 2.5), leading to an erroneous 0 eV formation energy. Compared to SW potential, ReaxFF provides a significant improvement in describing different types of defects in phosphorene.

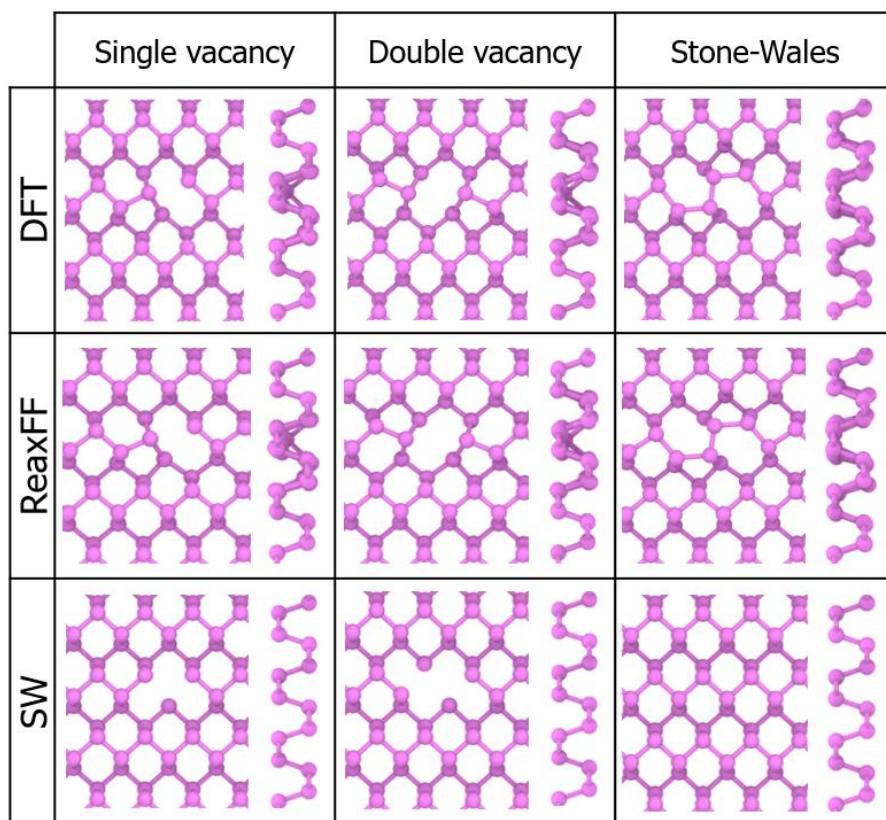


Figure 2.5 Structures of defected black phosphorene calculated with DFT, ReaxFF and SW potential

Table 2.11

DFT results versus ReaxFF results of formation energies of SV, DV and SW defects in black phosphorene compared to SW results.

Defect	Defect formation energy (eV)		
	DFT	ReaxFF	SW ⁷⁴
SV	1.66	1.80	0.54
DV	1.95	2.29	0.73
SW	1.42	1.94	0.00

2.4.5 Adatoms for black phosphorene: a transferability test

Due to its 2D nature, the large surface area to volume ratio of a black phosphorene nanosheet leads to a high chemical activity to foreign atoms. Thus the accurate description of surface adatoms in phosphorene is an important objective for ReaxFF. Structures and formation energies of phosphorus and hydrogen adatoms for black phosphorene were withheld from the training set, to serve as the validation data. The adsorption energy of adatoms on phosphorene, E_{ad} , defined by

$$E_{ad} = E_{adsorp} - E_{psheet} - E_{atom} \quad (2.5)$$

where E_{adsorp}/E_{psheet} is the total energy of phosphorene with/without adatoms and E_{atom} is the energy of the isolated atom. Figure 2.6 shows that ReaxFF agrees very well with DFT calculations for predicting the adsorption structures of P and H adatoms. By contrast, the SW potential overestimates the bond length between P adatom and upper P atoms in black phosphorene. Without P-H interactions, SW potential is not capable to describe the H adatoms for black phosphorene. In Table 2.12, it can be seen that ReaxFF provides a good description of the binding energy of P adatom and slightly overestimates the binding energy of H adatom. However, the SW potential underestimates the binding energy of P adatom by an order of magnitude. Overall, ReaxFF

provides a good description of P and H adatoms on black phosphorene. Since the structures and formation energies of P and H adatoms for black phosphorene were not included in the training set, these results indicate a good transferability of the ReaxFF for P/H systems.

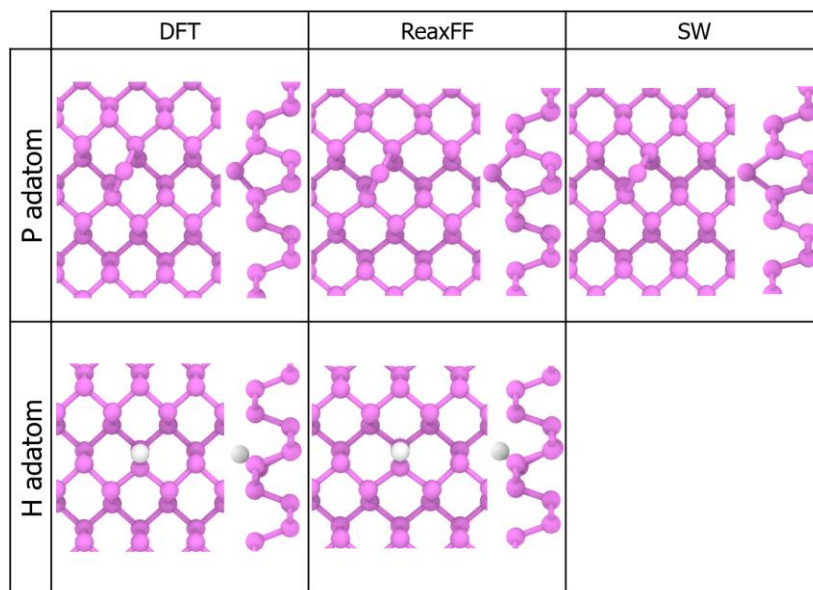


Figure 2.6 Adsorption structures of P and H adatoms on black phosphorene calculated with DFT and ReaxFF compared to SW results (only for P adatom).

Table 2.12

DFT results versus ReaxFF results of binding energies of phosphorus and hydrogen adatoms in black phosphorene compared to SW result (only for P).

Atom	Adatom binding energy (eV)		
	DFT	ReaxFF	SW ⁷⁴
P	-1.67	-1.60	-0.28
H	-1.34	-1.54	

2.4.6 Mechanical property of black phosphorene predicted by ReaxFF

In Table 2.13, the Young's moduli and Poisson's ratios of black phosphorene in armchair and zigzag directions calculated by ReaxFF and SW potential are compared to DFT results.

ReaxFF performs fairly well in reproducing the Young's moduli and Poisson's ratios of black phosphorene in both directions. However, SW potential underestimates the Young's moduli of black phosphorene in both directions, and the Poisson's ratios calculated by SW potential are an order of magnitude smaller than DFT results. Figure 2.7(a) shows the stress-strain curves of black phosphorene in zigzag and armchair directions calculated with DFT, ReaxFF and SW potential. For zigzag direction, ReaxFF is able to capture the modulus change as the strain increases, providing a reasonable agreement in ultimate strength and failure strain. However, the SW potential severely underestimates the ultimate strength and failure strain in the zigzag direction. For armchair direction, ReaxFF overpredicts the failure strain while SW potential underpredicts it. The ultimate strength of black phosphorene in the armchair direction is slightly overestimated by ReaxFF, while it is severely underestimated by SW potential. ReaxFF yields a smaller failure strain at 300 K than 1.0 K for both the zigzag and armchair directions (see Figure 2.7(b)). Generally, ReaxFF gives a much better representation of the mechanical response of pristine black phosphorene over the SW potential.

Table 2.13

DFT results versus ReaxFF results of Young's modulus and Poisson ratios of black phosphorene in armchair and zigzag directions compared to SW results.

	DFT	ReaxFF	SW ⁷⁴
E_{arm} (GPa)	37.8	38.4	33.5
E_{zig} (GPa)	160.4	145.9	105.5
$E_{\text{zig}} / E_{\text{arm}}$	4.24	3.81	3.15
ν_{arm}	0.18	0.20	0.013
ν_{zig}	0.61	0.55	0.075

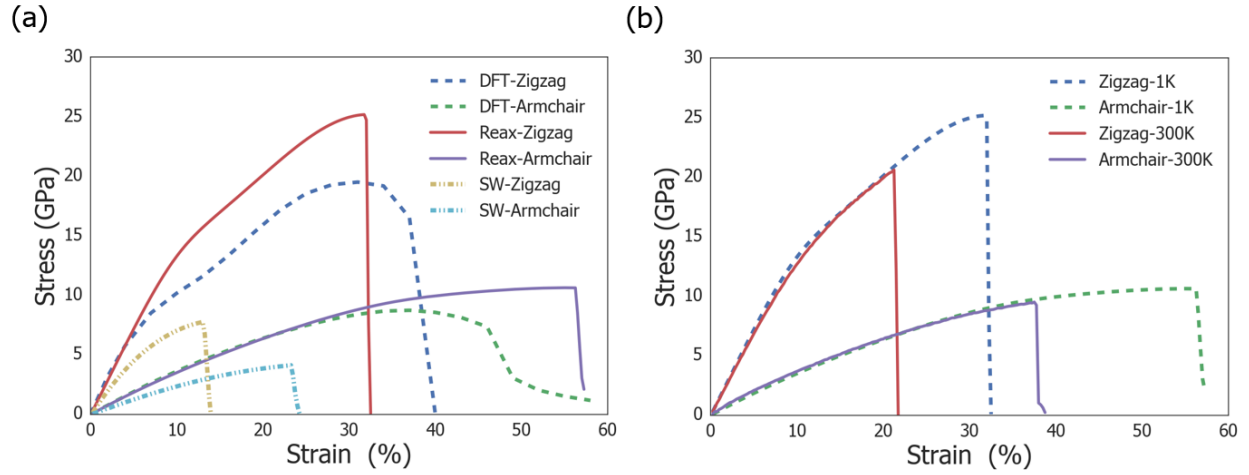


Figure 2.7 (a) Stress-strain responses of black phosphorene along the armchair direction and zigzag direction calculated by ReaxFF and SW potential at 1 K compared to DFT results. (b) Stress-strain responses of black phosphorene along the armchair direction and zigzag direction calculated by ReaxFF at 1 K and 300 K.

2.4.7 Effect of defects on the mechanical response of black phosphorene

Stress-strain curves of defected black phosphorene in the armchair and zigzag directions calculated with ReaxFF at 1 K are shown in Figure 2.8(a) and Figure 2.8(b), respectively. For armchair direction, black phosphorene with single vacancies shows a larger reduction in the failure strain than black phosphorene with double vacancies (keeping defect density the same), even though the double vacancy has a higher formation energy than the single vacancy. The reduction in the failure strain induced by Stone-Wales defect is in between that of single and double vacancy. The Young's modulus in the armchair direction is more or less unaffected by all three types of defects. For zigzag direction, all three types of defects reduce the failure strain by about 50%. Only minor reduction in the Young's modulus in the zigzag direction is induced by all three types of

defects. Thus, the mechanical response of black phosphorene in the zigzag direction is more sensitive to defects than that for the armchair direction.

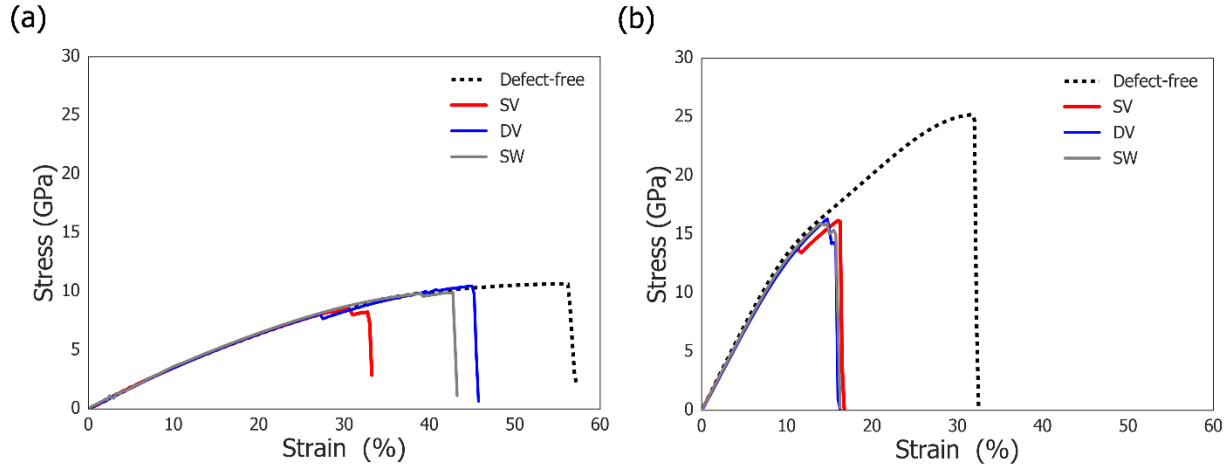


Figure 2.8 Stress-strain responses of defected and defect-free black phosphorene along the armchair direction (a) and the zigzag direction (b) calculated by ReaxFF at 1K.

To understand these phenomenon, the structural deformation and stress distribution of defected black phosphorene under tension ($\epsilon = 0.13$) in the armchair (Figure 2.9(a-c)) and zigzag (Figure 2.9(d-f)) directions were analyzed. For armchair direction (Figure 2.9(a-c)), stress at the single vacancy is more concentrated than that of double vacancy and Stone-Wales defect, due to the unsymmetrical defect geometry of single vacancy (double vacancy and Stone-Wales defect has central symmetry). Thus, the black phosphorene with single vacancies shows a larger reduction in the failure strain along the armchair direction than black phosphorene with double vacancies and Stone-Wales defects. Intriguingly, the structure of black phosphorene with single vacancy undergoes an unsymmetric-to-antisymmetric transition induced by tension in the zigzag direction (Figure 2.9(d)). Consequently, three types of defects have similar influence on the mechanical response of black phosphorene under tension along the zigzag direction.

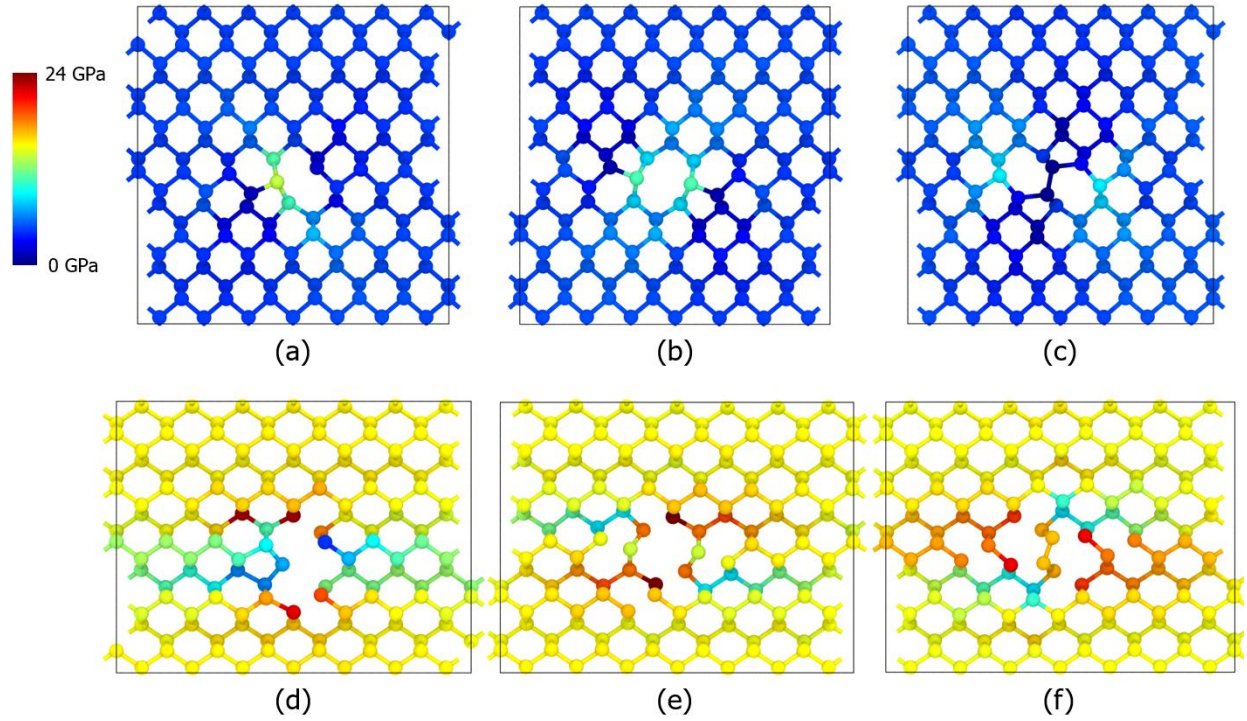


Figure 2.9 Structure deformation and stress distribution of black phosphorene with single vacancy (a), double vacancy (b) and Stone-Wales defect (c) at $\epsilon_{\text{armchair}} = 0.13$. Structure deformation and stress distribution of black phosphorene with single vacancy (d), double vacancy (e) and Stone-Wales defect (f) at $\epsilon_{\text{zigzag}} = 0.13$. Colors show the stress distribution.

Hao *et al.*¹⁰⁵ conducted first-principles study of the effect of single and double vacancies on the mechanical response of black phosphorene. The effect of single and double vacancies on the mechanical response of black phosphorene in both armchair and zigzag directions predicted by ReaxFF agrees fairly well with DFT results.¹⁰⁵ This clearly shows that ReaxFF for P/H systems provides a robust tool to study the effect of defects on the mechanical response of black phosphorene on a much larger space and time scale compared to DFT.

2.4.8 Thermal stability of phosphorene nanotubes

Similar to carbon nanotubes, the electrical and optical properties of the one-dimensional phosphorus nanotube (PNT) are chirality dependent and can be tuned by strain and size,^{106–111} shedding light on its potential applications in transistors, strain sensors and photodetectors. Thus the accurate description of the properties of PNTs is important for ReaxFF. Two types of PNTs were designed by wrapping up a phosphorene sheet along the zigzag and armchair directions, i.e. $(m, 0)$ zigzag PNTs and $(0, n)$ armchair PNTs.^{109,112} Figure 2.10 shows that compared to SW potential, ReaxFF provides a more accurate description of the cohesive energies change of the zigzag PNTs and armchair PNTs with respect to their sizes. SW potential underpredicts the cohesive energies of PNTs by an order of magnitude, indicating that SW potential could seriously underestimate the thermal stability of PNTs.¹¹³ The phase diagrams for thermal stability of the zigzag PNTs and the armchair PNTs with varying temperatures and wrapping vectors of the nanotube are shown in Figure 2.10(c) and Figure 2.10(d), respectively. It is seen that SW potential strongly underpredicts the thermal stability of PNTs, compared to ReaxFF. Guan et al.¹⁰⁸ reported highly stable faceted PNTs can be constructed by laterally joining nanoribbons of different phosphorene phases. Intriguingly enough, ReaxFF for P/H is able to predict the phase transition of armchair and zigzag PNTs into faceted PNTs with higher thermal stability at elevated temperature, as shown in the inset figure. This discovery sheds light on the possible fabrication strategy of faceted PNTs. In short, ReaxFF is more reliable in describing the thermal stability of phosphorene nanotubes, compared to SW potential.

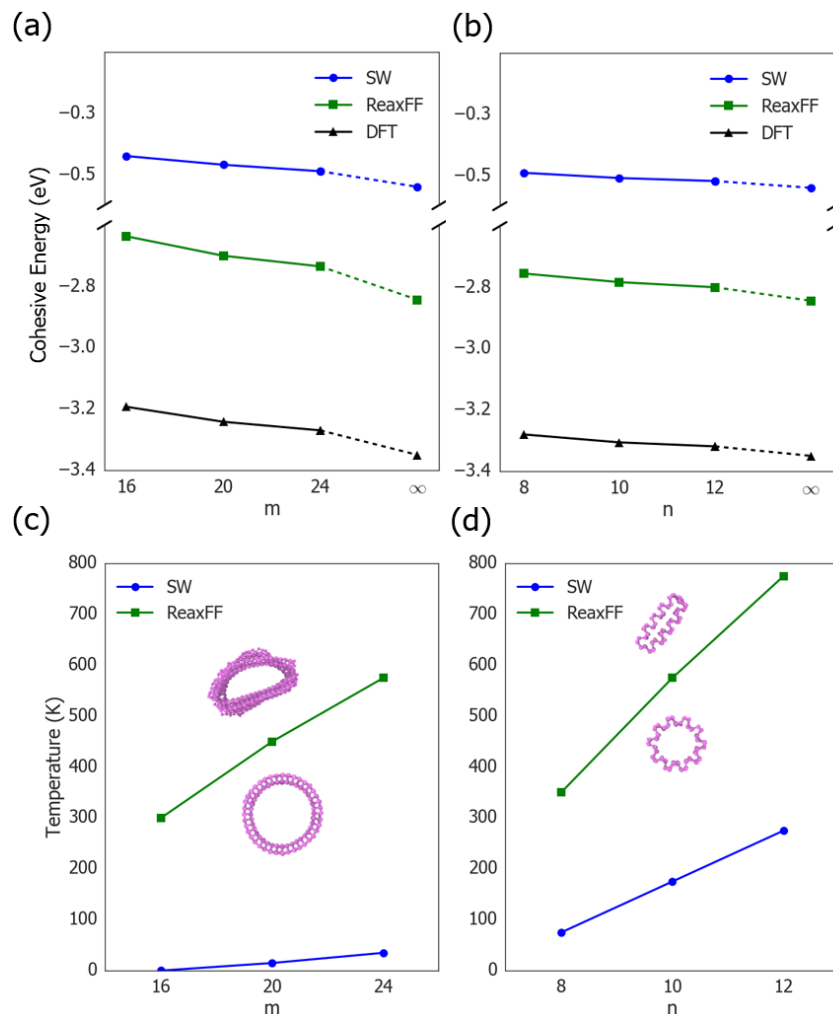


Figure 2.10 Cohesive energies of the $(m, 0)$ zigzag PNT (a) and $(0, n)$ armchair PNT (b). The phase diagrams for thermal stability of the $(m, 0)$ zigzag PNTs (c) and the $(0, n)$ armchair PNTs (d) with varying temperatures and wrapping vectors of the nanotube. Stable and unstable PNT structures are shown.

2.5 Concluding remarks

We present a reactive force field (ReaxFF) for phosphorus and hydrogen, which gives an accurate description of the chemical and mechanical properties of pristine and defected black phosphorene. A 60° correction term is added which significantly improves the description of phosphorus clusters. ReaxFF for P/H is transferable to a wide range of P/H systems including bulk

black phosphorus, blue phosphorene, phosphorus clusters and phosphorus hydride molecules. Emphasis has been placed on obtaining a good description of mechanical response of black phosphorene with different types of defects. Compared to SW potential, ReaxFF for P/H systems provides a notable improvement in describing the cohesive energy, mechanical response of pristine and defected black phosphorene and the thermal stability of phosphorene nanotubes. We observe a counterintuitive phenomenon that single vacancies weaken the black phosphorene more than relatively more unstable double vacancies. It was shown that the mechanical response of black phosphorene is more sensitive to defects in the zigzag direction than the armchair direction. Straightforward extensions to the heterogeneous systems, including oxides, nitrides, etc., enable the ReaxFF parameters for P/H systems to build a solid foundation for the simulation of a wide range of P-containing materials.

Chapter 3 Prediction of a Two-dimensional S₃N₂ Solid for Optoelectronic Applications

3.1 Introduction

The epic discovery of graphene¹³ has inspired the exploration of a whole family of 2D materials, including the 2D insulator boron nitride (BN),^{26–28} graphene analogues of group IV elements, i.e. semimetallic silicene, germanene, and stanine,^{114–120} 2D transition-metal dichalcogenides,^{121–125} such as molybdenum disulfide^{26,29,30} and tungsten disulfide,¹²⁶ and very recently, 2D phosphorus, i.e. phosphorene,³¹ which extend the 2D material family into the group V. These 2D free-standing crystals exhibit unique and fascinating physical and chemical properties that differ from those of their 3D counterparts,^{127,128} opening up possibilities for numerous advanced applications. For example, MoS₂, MoSe₂, and WS₂ are able to achieve one order of magnitude higher sunlight absorption than traditional photovoltaic materials such as GaAs and Si.¹²⁹ Two-dimensional materials offer novel opportunities for fundamental studies of unique physical and chemical phenomena in 2D systems.^{130,131}

Over the past decade, tremendous progress has been made in the synthesis of 2D materials. Nonetheless, the cycles of synthesis, characterization and testing for 2D materials are slow and costly, which inspired the development of computational tools to design or predict new 2D materials, such as the evolutionary crystal structure search^{132,133,67} and particle swarm optimization (PSO) techniques.⁶⁸

In this chapter, based on the evolutionary algorithm driven structural search, we proposed a new S₃N₂ 2D crystal that is dynamically, thermally and chemically stable as confirmed by the computed phonon spectrum and *ab initio* molecular dynamics simulations. GW band structure

calculations showed that 2D S₃N₂ crystal is a semiconductor with wide, direct band gap of 3.92 eV and a low hole effective mass. Anisotropic optical response of 2D S₃N₂ crystal was revealed by GW-BSE calculations. These fascinating properties could pave the way for potential innovations in 2D electronics, optoelectronics, etc.

3.2 Computational methods

The ground state structure of S₃N₂ was obtained using the evolutionary algorithm driven structural search code USPEX.^{132,133,67} The S₃N₂ structures were further geometry optimized with density functional calculations with Perdew–Burke–Ernzerhof (PBE)⁸⁴ exchange-correlation functional using the *ab initio* code Quantum Espresso.¹³⁴ Ultrasoft pseudopotentials are used to describe electron-ion interactions, and a plane-wave cutoff energy of 40 Ry is used, and Monkhorst-Pack⁸⁶ meshes with 0.02 Å⁻¹ *k*-point spacing were used. The convergence test of cutoff energy and *k*-point mesh was conducted. All structure optimizations were conducted without imposing any symmetry constraints. The conjugate gradient method (CG) was used to optimize the atomic positions until the change in total energy was less than 5 ×10⁻⁶ eV/atom, and the maximum displacement of atoms was less than 5 ×10⁻⁵ Å. Since the band gaps may be dramatically underestimated by the GGA level DFT,^{135,136} the quasiparticle GW calculation¹³⁷ of the band structure was carried out using YAMBO software package.¹³⁸ The Green function and Coulomb screening were constructed from the PBE⁸⁴ results, and the plasmon-pole model was used for computing the screening. The G₀W₀ approximation was adopted in carrying out the GW approximation, since it gives very good results for many materials without *d* electrons.¹³⁹ Optical spectra of S₃N₂ in [100] and [010] directions were calculated using the Bethe-Salpeter-equation (BSE) method^{140,141} with a finer *k*-point grid of 36×18×1. Only the incident light polarized parallel

with the 2D crystal was considered in studying the optical spectra, due to the depolarization effect.^{142,143}

3.3 Results and discussion

We theoretically searched for 2D materials in an unexplored territory: 2D crystals composed of nitrogen and sulfur. A new two-dimensional trisulfur dinitride (S_3N_2) crystal with 3 polymorphs: α - S_3N_2 (Figure 3.1(a)), β - S_3N_2 (Figure 3.1(b)) and γ - S_3N_2 (Figure 3.1(c))) were proposed, based on the evolutionary algorithm driven structural search using USPEX.^{132,133,67} The geometry optimized S_3N_2 crystals are shown in Figure 3.1. These S_3N_2 polymorphs are 2D covalent networks composed solely of σ bonds (bonding is depicted by isosurfaces of the electron density). For α - S_3N_2 (space group Pmn21), the unit cell (see Figure 3.1(a)) consists of ten atoms with lattice constants $a = 4.24$ Å, $b = 8.89$ Å, S-N bonds with bond lengths $d_1 = 1.81$ Å, $d_2 = 1.72$ Å, $d_3 = 1.66$ Å, and bond angles $\theta_1 = 116.8^\circ$, $\theta_2 = 119.3^\circ$, $\theta_3 = 119.2^\circ$, $\theta_4 = 106.1^\circ$ and $\theta_5 = 103.7^\circ$ (see Figure 3.1(a)). The unit cell of β - S_3N_2 (space group Pba2) consists of ten atoms with lattice constants $a = 5.22$ Å, $b = 7.73$ Å, S-N bonds with bond lengths $d_1 = 1.68$ Å, $d_2 = 1.70$ Å, $d_3 = 1.82$ Å and bond angles $\theta_1 = 103.6^\circ$, $\theta_2 = 123.9^\circ$, $\theta_3 = 126.3^\circ$, $\theta_4 = 110.0^\circ$ and $\theta_5 = 109.8^\circ$ (see Figure 3.1(b)). The unit cell of γ - S_3N_2 (space group P31m) consists of five atoms with lattice constants $a_1 = a_2 = 5.08$ Å, S-N bonds with bond length $d_1 = 1.80$ Å, and bond angles $\theta_1 = 98.3^\circ$ and $\theta_2 = 109.3^\circ$ (see Figure 3.1(c)). The Brillouin zone with the relevant high-symmetry k-points is depicted in the inset figure for each S_3N_2 polymorph in Figure 3.2(a-c). The cohesive energies of α - S_3N_2 , β - S_3N_2 and γ - S_3N_2 are -3.34 eV, -3.28 eV and -3.09 eV, respectively. Thus the most stable polymorph is α - S_3N_2 .

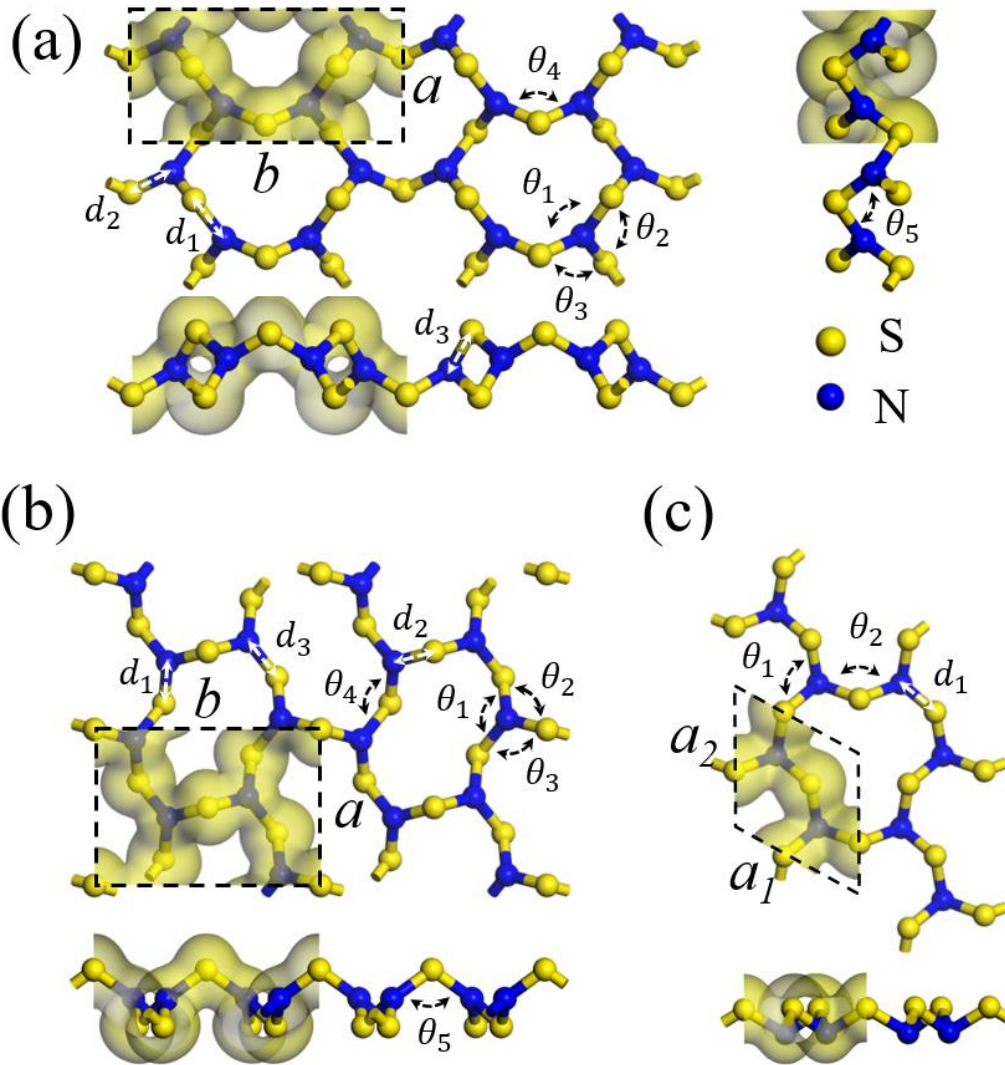


Figure 3.1 2D crystalline structures of α - S_3N_2 (a), β - S_3N_2 (b) and γ - S_3N_2 (c). Bonding is depicted by an isosurface of the electron density.

By conducting phonon dispersion calculation of the free-standing S_3N_2 polymorphs, we verified that all phonon frequencies of the most stable polymorph, α - S_3N_2 , are real (Figure 3.2(a)), confirming its dynamic stability. However, β - S_3N_2 and γ - S_3N_2 are not stable in the local minimum, since they have imaginary phonon frequencies (Figure 3.2(b-c)). In the following discussions, we focus on the properties of the dynamically stable α - S_3N_2 .

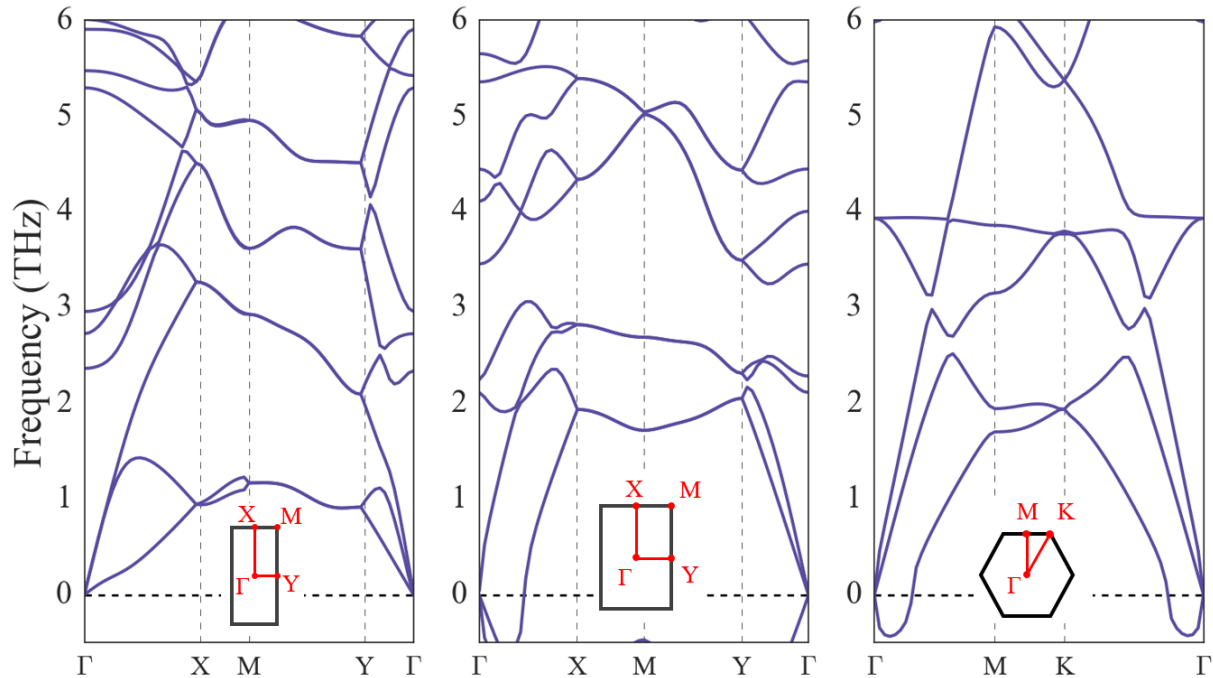


Figure 3.2 The phonon dispersion relations of α -S₃N₂ (a), β -S₃N₂ (b) and γ -S₃N₂ (c). The Brillouin zone of each polymorph, with the relevant high-symmetry k -points indicated, is shown in the inset figure.

Even though all phonon frequencies of the α -S₃N₂ ensure dynamic stability, the optimized structure may correspond to a shallow local minimum and therefore may be unstable at a finite temperature. To verify the stability of α -S₃N₂ at finite temperature, *ab initio* molecular dynamics (MD) simulations (shown in Figure 3.3) were performed at the PBE⁸⁴/GTH-DZVP¹⁴⁴ level in the NPT ensemble of the CP2K¹⁴⁵ code. The simulations were run for 10 ps under 1 atm pressure at temperatures $T = 800$ K and 1000 K, respectively. The stability of α -S₃N₂ structure was maintained at 800 K for 10 ps. However, the crystalline structure dissociated into multiple S-N chains and clusters at 1000 K. These MD calculations verified that the stability of α -S₃N₂ structure holds at least above the room temperature.

The concepts of dynamic stability and thermal stability are related and confusing, so we will provide a detailed introduction of the concepts of them. If the potential energy of a crystal always increases against any combinations of small atomic displacements, the crystal is dynamically stable. Under the harmonic approximation, this is equivalent to the situation that all phonon frequencies are real and positive. Meanwhile, the thermal stability represents the ability of a crystal to resist chemical change (e.g. decomposition) at a certain temperature. Thus, the dynamic stability is the prerequisite for the thermal stability. That is, if a crystal is dynamically unstable, it is definitely thermally unstable, even at very low temperatures (when the atomic displacements induced by thermal fluctuations are small).

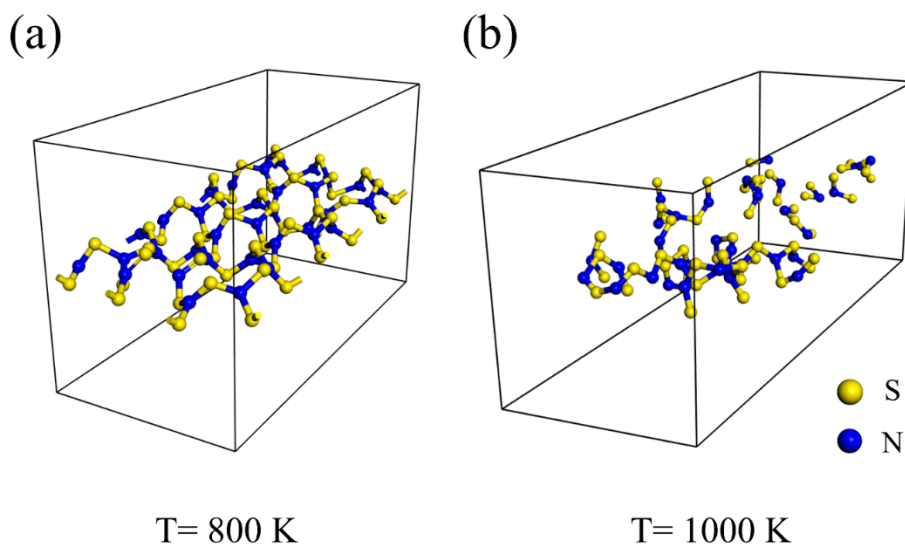


Figure 3.3 *Ab initio* MD snapshots of the α - S_3N_2 supercell structures at temperatures (a) $T = 800 \text{ K}$ (b) $T = 1000 \text{ K}$ under ambient pressure at 10 ps.

To further testify the chemical stability of the structure in air, *ab initio* MD of α - S_3N_2 crystal exposed to very high pressure gases (O_2 , N_2 , H_2O and H_2) at temperatures $T = 800 \text{ K}$ were conducted (Figure 3.4). In our MD simulations, the number density of gas molecules was $73.6 \times$

10^{25} m^{-3} . Such a high gas pressure were also used to study oxidation of graphene¹⁴⁶ and phosphorene¹⁴⁷ in MD simulations. The α -S₃N₂ structure remained intact under these very high gas pressure for 10 ps (Figure 3.4), indicating its chemical stability in air at least above the room temperature.

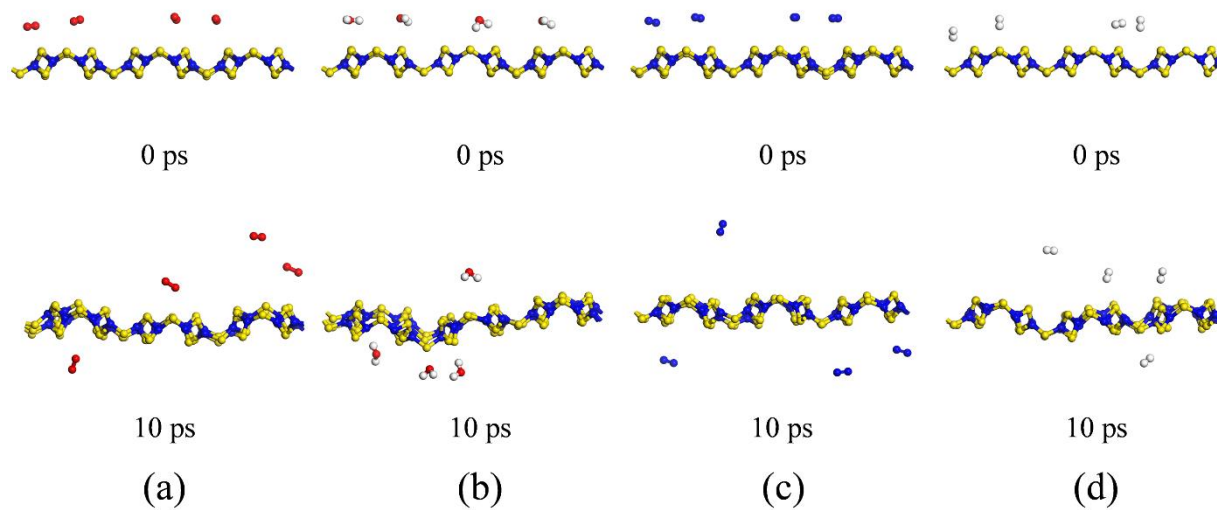


Figure 3.4 *Ab initio* MD snapshots of the α -S₃N₂ supercell structures exposed to the high pressure (a) oxygen gas, (b) water vapour, (c) nitrogen gas and (d) hydrogen gas at temperatures $T = 800$ K.

The quasiparticle and DFT band structures and density of states of the 2D α -S₃N₂ crystal are shown in Figure 3.5. Calculations carried out using GW method showed that the α -S₃N₂ structure is a semiconductor with a wide, direct band gap of 3.92 eV (calculations carried out using PBE functional would underestimate the band gap by 1.90 eV). This is a well-sought characteristic, since most 2D semiconductors reported thus far exhibit band gaps that are smaller than 2 eV. Both the valence band maximum (VBM) and the conduction band minimum (CBM) are composed of mainly the orbitals of sulfur atoms, as shown in Figure 3.5. We also computed the effective mass

of the electrons and holes (shown in Figure 3.5) for the α -S₃N₂ structure at the Γ point along the Γ -X and the Γ -Y directions. The effective electron masses were found to be $m_e^{\Gamma X} = 0.83 m_o$ and $m_e^{\Gamma Y} = 1.08 m_o$, where m_o is the free-electron mass. The effective hole masses were obtained to be $m_h^{\Gamma X} = 0.66 m_o$ and $m_h^{\Gamma Y} = 1.00 m_o$. The effective mass of carriers along the Γ -X direction is lighter than that along the Γ -Y direction, showing an anisotropic transport property. Contrary to the common scenario where the effective mass of hole is greater than electron, the hole effective mass in the present α -S₃N₂ crystal is lighter than its electron counterpart. In short, 2D α -S₃N₂ crystal has a small hole effective mass.

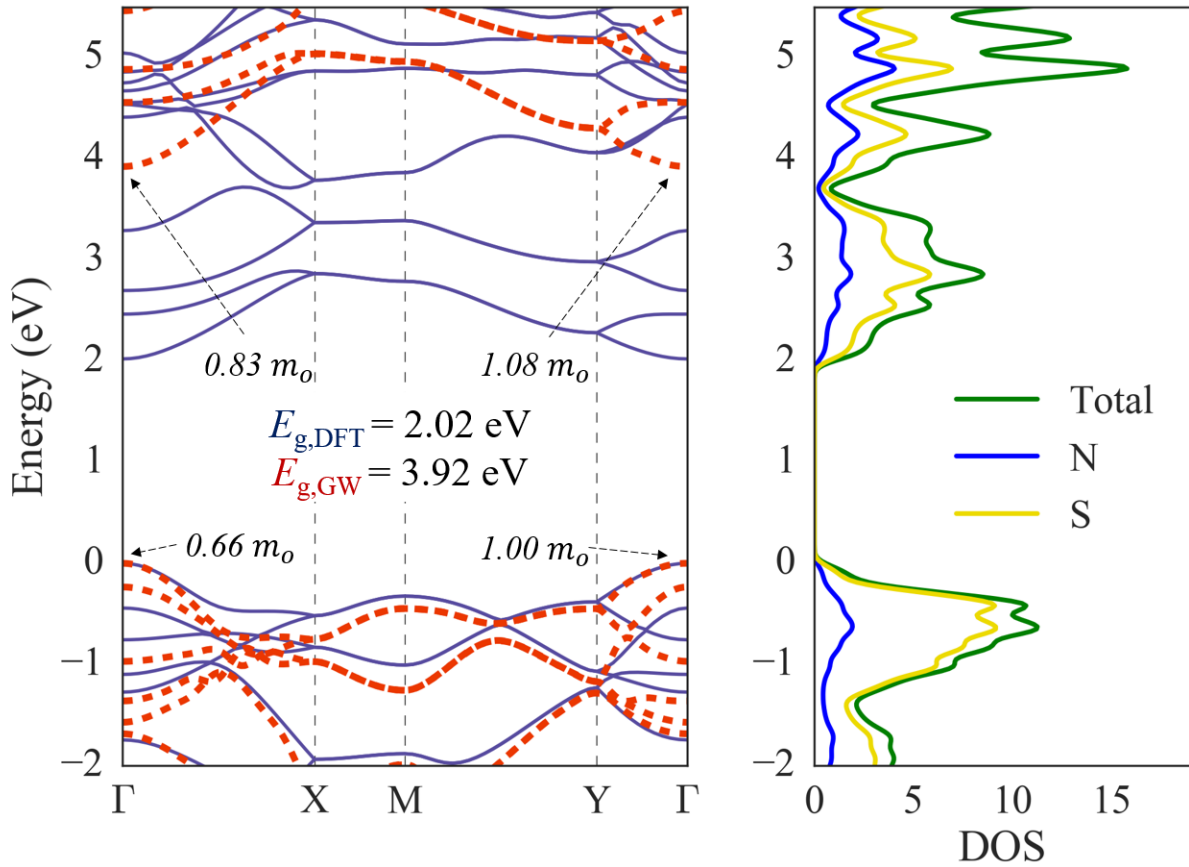


Figure 3.5 Calculated band structure (left) obtained with the PBE functional (blue lines) and the GW method (red dash lines) for the α -S₃N₂ solid. The DOS (right) is obtained with the PBE functional. The effective mass of electrons and holes at the Γ point along the Γ -X and the Γ -Y directions are indicated by black arrows.

The optical absorption spectra for the α -S₃N₂ crystal for the incident light polarized along the [100] and [010] directions are presented in Figure 3.6. Anisotropic optical responses of α -S₃N₂ is observed. A huge exciton binding energy $E_b = 1.19$ eV clearly shows that the optical spectra of α -S₃N₂ is largely affected by the excitonic effects. The optical band gap of the α -S₃N₂ crystal is 2.73 eV.

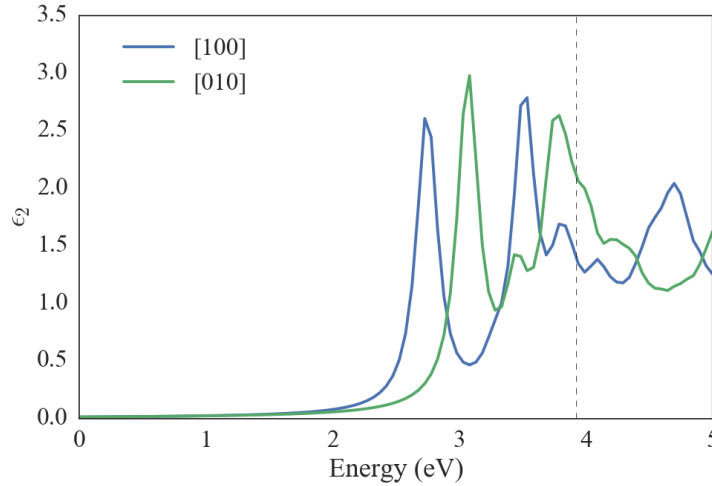


Figure 3.6 G₀W₀+BSE absorption spectra for the α -S₃N₂ crystal for the incident light polarized along the [100] and [010] directions. The black vertical dashed line marks electronic band gap calculated at the level of G₀W₀.

As a 2D material with a wide, direct band gap, combined with a small hole effective mass, the α -S₃N₂ crystal may be an ideal candidate for optoelectronic applications such as ultra-violet light-emitting diodes and semiconductor lasers. Furthermore, the band gap of α -S₃N₂ structure can be tuned by stacking into multilayer α -S₃N₂ crystals, cutting into α -S₃N₂ nanoribbons or rolling up to form α -S₃N₂ nanotubes, expanding its potential applications.

3.4 Concluding remarks

In conclusion, we predicted a new two-dimensional S_3N_2 crystal with distinctive structures and outstanding properties. Band structures calculated using the GW method indicate that 2D S_3N_2 crystal is a wide, direct band-gap (3.92 eV) semiconductor with a small hole effective mass. The anisotropic optical response of 2D S_3N_2 crystal was revealed by GW-BSE calculations. These fascinating properties could pave the way for its optoelectronic applications such as blue or ultra-violet light-emitting diodes (LEDs) and photodetectors.

Chapter 4 Predicting a Two-dimensional P_2S_3

Monolayer: A Global Minimum Structure

4.1 Introduction

Graphene,¹³ the first two-dimensional (2D) material discovered in experiments, has paved the way for the synthesis of many other 2D materials, including the 2D insulator boron nitride (BN),^{26–28} graphene-like group IV 2D materials, i.e. semimetallic silicene, germanene, and stanene,^{114–120} 2D transition-metal dichalcogenides,^{121–125} such as molybdenum disulfide^{26,29,30} and tungsten disulfide,¹²⁶ and recently, 2D phosphorus, i.e. phosphorene,³¹ which holds great promise for applications in electronics and optoelectronics.

Owing to the reduced dimensionality and symmetry, 2D materials have unique electronic, optical and mechanical properties that differ from their bulk counterparts,^{127,128} offering possibilities for numerous advanced applications. For instance, transistors made of single layer MoS_2 present room-temperature current on/off ratios of 10^8 .³⁰ Two-dimensional materials also provide new opportunities for fundamental studies of unique physical and chemical phenomena in 2D systems.^{130,131} More interestingly, stacking different 2D crystals into hetero-structures (often referred to as ‘van der Waals’) has recently been investigated, which leads to new phenomena and novel properties.¹⁴⁸

Over the past decade, a number of experimental methods have been developed to produce monolayer nanosheets by exfoliating layered materials with oxidation, ion intercalation/exchange, or surface passivation induced by solvents.^{149,150} Theoretical approach is perhaps more efficient to search new two-dimensional materials, including evolutionary crystal structure search^{132,133,67} and particle swarm optimization (PSO).⁶⁸ For example, Li *et al.*¹⁵¹ discovered a novel 2D Be_2C

monolayer, with each carbon atom binding to six Be atoms to form a quasi-planar hexacoordinate carbon moiety. In Chapter 3, we proposed a novel light-emitting 2D crystal with a wide direct band gap, namely S_3N_2 monolayer, by using the evolutionary crystal structure search method. The amazing properties of the S_3N_2 2D crystal inspired us to explore the possibility of other group V-VI 2D crystals.

In this chapter, based on the evolutionary algorithm driven structural search, we proposed a new P_2S_3 2D crystal that is dynamically, thermally and chemically stable as confirmed by the computed phonon spectrum and ab initio molecular dynamics simulations. Quasi-particle band structure calculations showed that the P_2S_3 monolayer is a semiconductor with wide band gap of 4.55 eV. The electronic properties of P_2S_3 structure can be modulated by stacking into multilayer P_2S_3 structures, forming P_2S_3 nanoribbons or rolling into P_2S_3 nanotubes, expanding its potential applications for the emerging field of 2D electronics.

4.2 Computational methods

The ground state structure of three P_2S_3 polymorphs (α - P_2S_3 (Figure 4.1(a)), β - P_2S_3 (Figure 4.1(b)) and γ - P_2S_3 (Figure 4.1(c))) were obtained using the evolutionary algorithm driven structural search code USPEX.^{132,133,67} The three P_2S_3 polymorphs were further geometry optimized by density functional calculations with Perdew–Burke–Ernzerhof (PBE)⁸⁴ exchange-correlation functional using the Cambridge series of total-energy package (CASTEP).^{82,83} A plane-wave cutoff energy of 700 eV was used, and Monkhorst-Pack⁸⁶ meshes with 0.02 \AA^{-1} k -point spacing were adopted, which meet the convergence criteria. To calculate the binding energy of bilayer α - P_2S_3 , the empirical dispersion correction schemes proposed by Grimme (D2)⁸⁵ was used in combination with PBE functional to properly describe the van der Waals (vdW) interactions between α - P_2S_3 layers. Since the band gaps may be dramatically underestimated by the GGA-DFT

level,^{135,136} the quasiparticle GW calculation¹³⁷ was conducted to obtain the band structure using YAMBO software package.¹³⁸ The Green function and Coulomb screening were constructed based on the PBE results from Quantum Espresso¹³⁴, and the plasmon-pole model was employed for computing the screening. The G_0W_0 approximation was adopted in carrying out the GW approximation, since it gives accurate results for many materials without d electrons¹³⁹. All structure optimizations were conducted without any imposed symmetry constraints. The conjugate gradient method (CG) was used to optimize the atomic positions until the change in total energy was less than 5×10^{-6} eV/atom, maximum stress within 0.01 GPa and the maximum displacement of atoms was less than 5×10^{-5} Å.

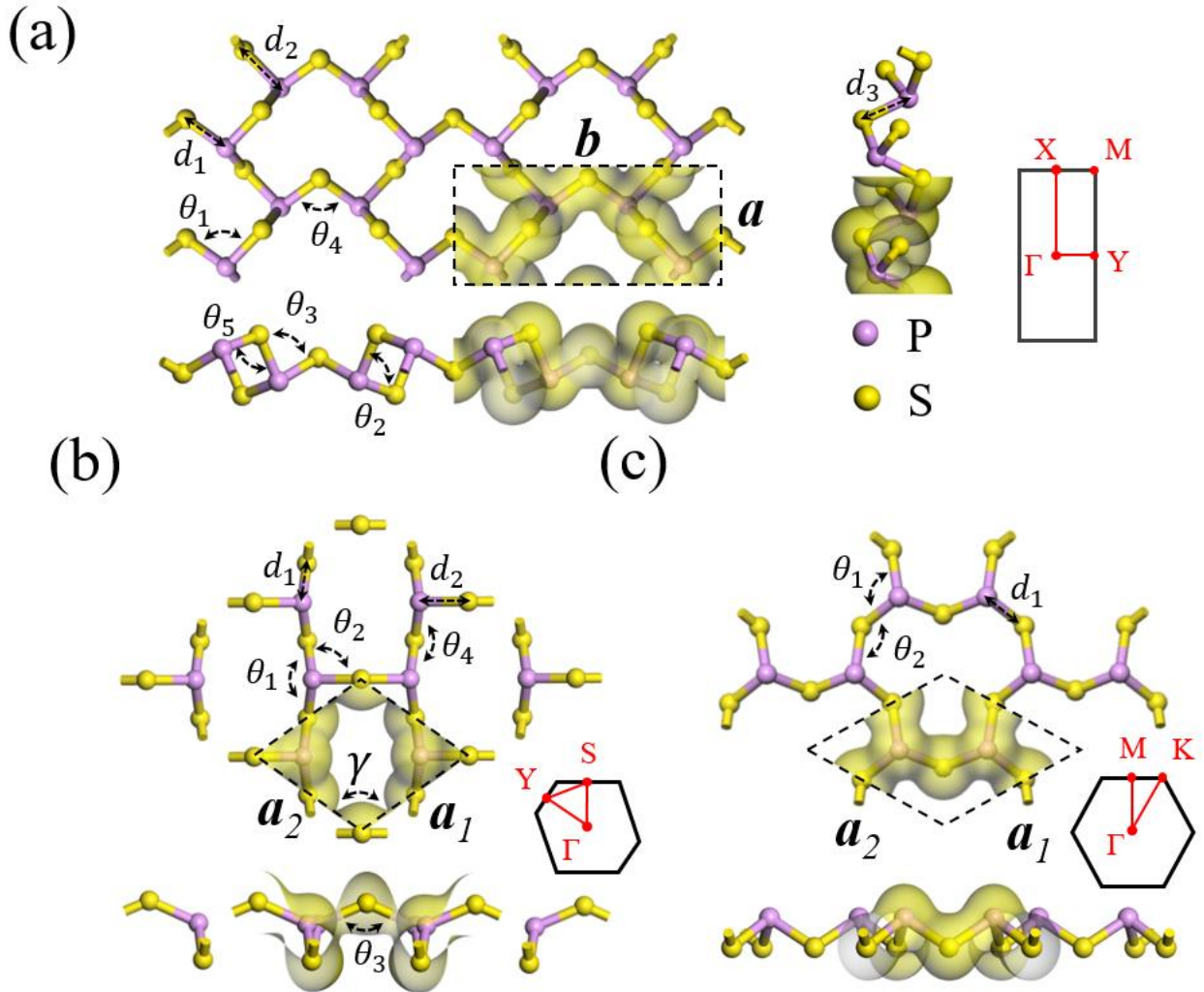


Figure 4.1 2D crystalline structures of α -P₂S₃ (a), β -P₂S₃ (b) and γ -P₂S₃ (c). The Brillouin zone of each polymorph, with the relevant high-symmetry k -points indicated, is depicted in the inset figure. Bonding is depicted by an isosurface of the electron density.

4.3 Results and discussion

Figure 4.1 shows the fully relaxed P₂S₃ polymorphs. Regarding these P₂S₃ polymorphs, P and S are covalently connected in terms of σ bonds (bonding is depicted by isosurfaces of the electron density). For α -P₂S₃ (space group Pmn21), the unit cell (see Figure 4.1(a)) consists of ten atoms with lattice constants $a = 4.71$ Å, $b = 10.62$ Å, P-S bonds with bond lengths $d_1 = 2.14$ Å, $d_2 = 2.12$ Å, $d_3 = 2.15$ Å, and bond angles $\theta_1 = 103.8^\circ$, $\theta_2 = 105.7^\circ$, $\theta_3 = 96.2^\circ$, $\theta_4 = 94.4^\circ$ and $\theta_5 = 107.4^\circ$. The unit cell of β -P₂S₃ (space group Cmm2) consists of five atoms with lattice constants $a_1 = a_2 = 5.35$ Å, the angle between unit vector a_1 and a_2 , $\gamma = 108.8^\circ$, P-S bonds with bond lengths $d_1 = 2.14$ Å, $d_2 = 2.15$ Å, and bond angles $\theta_1 = 93.0^\circ$, $\theta_2 = 111.4^\circ$, $\theta_3 = 132.4^\circ$ and $\theta_4 = 94.1^\circ$ (see Figure 4.1(b)). The unit cell of γ -P₂S₃ (space group P31m) is comprised of five atoms with lattice constants $a_1 = a_2 = 5.92$ Å, P-S bonds with bond length $d_1 = 2.16$ Å, and bond angles $\theta_1 = 95.1^\circ$ and $\theta_2 = 104.9^\circ$ (see Figure 4.1(c)). For these polymorphs, the Brillouin zones with the relevant high-symmetry k -points are illustrated in the inset in Figure 4.1. The cohesive energies of α -P₂S₃, β -P₂S₃ and γ -P₂S₃ are -3.64 eV, -3.59 eV and -3.60 eV, respectively. Thus the most energetically favorable polymorph is α -P₂S₃.

Further, we perform other calculations to assure these polymorphs are stable in the local minimum and can remain stable above the room temperature, despite the aforementioned results that indicate the stability of these free standing P₂S₃ polymorphs by structure optimizations using CG method, First, by conducting phonon dispersion calculation of the free-standing P₂S₃ polymorphs, we verified that all phonon frequencies of α -P₂S₃ are real (Figure 4.2(a)), which

confirms the dynamic stability of this structure. However, β -P₂S₃ and γ -P₂S₃ are not dynamically stable, since they have imaginary phonon frequencies (Figure 4.2(b-c)). Thus, the following will be focused on the properties of the dynamically stable α -P₂S₃.

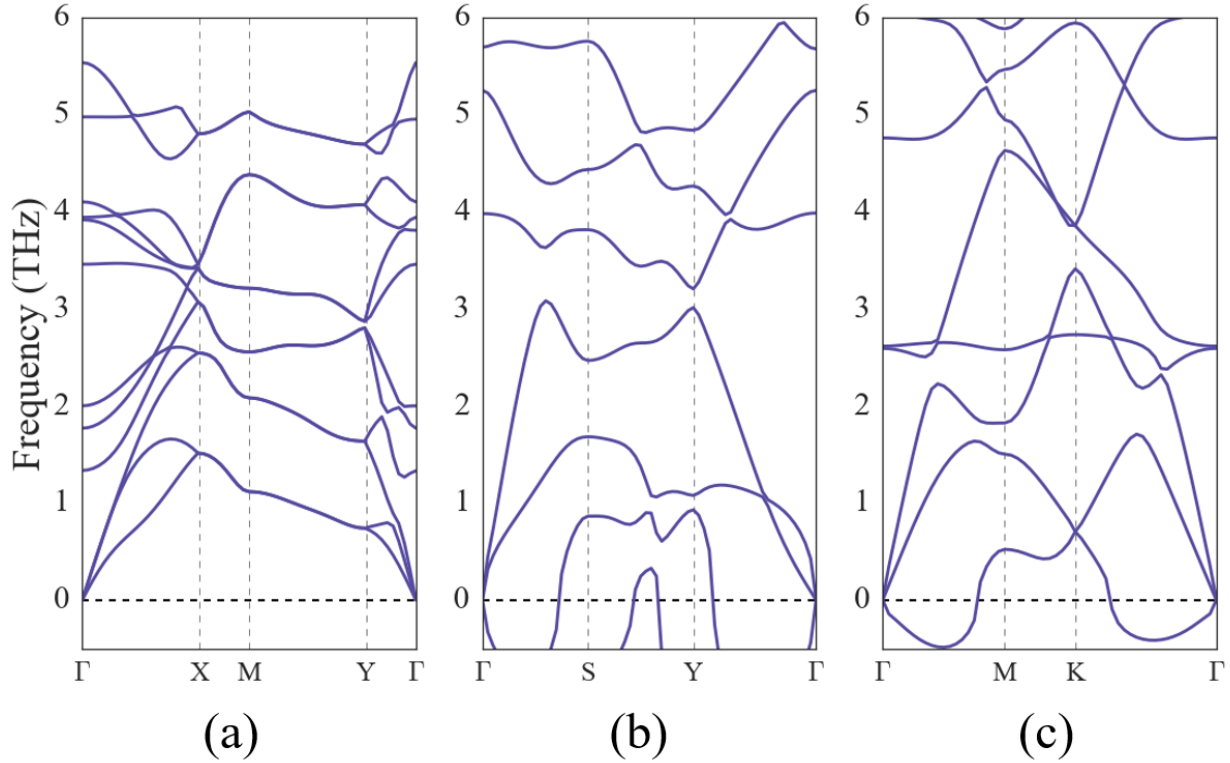


Figure 4.2 The phonon dispersion relations of α -P₂S₃ (a), β -P₂S₃ (b) and γ -P₂S₃ (c).

For α -P₂S₃, the enthalpy of formation ΔH from the elements



calculated by CASTEP at T=0 K is -14.2 kcal/mol. The enthalpies of formation of the most stable phase of P (black phosphorus) and S (α -sulfur) are used in this calculation. This means α -P₂S₃ is an energetically favorable composition relative to phosphorus and sulfur in their solid states.

To evaluate the stability of the structure at finite temperature, *ab initio* molecular dynamics (MD) simulations (shown in Figure 4.3) were performed at the PBE⁸⁴/GTH-DZVP¹⁴⁴ level in the NPT ensemble with the CP2K¹⁴⁵ code. The simulations were run for 10 ps under 1

atm pressure with temperature $T = 1000$ K and no breaking of the bonds was found, indicating the stability of α -P₂S₃ structure holds at least above the room temperature.

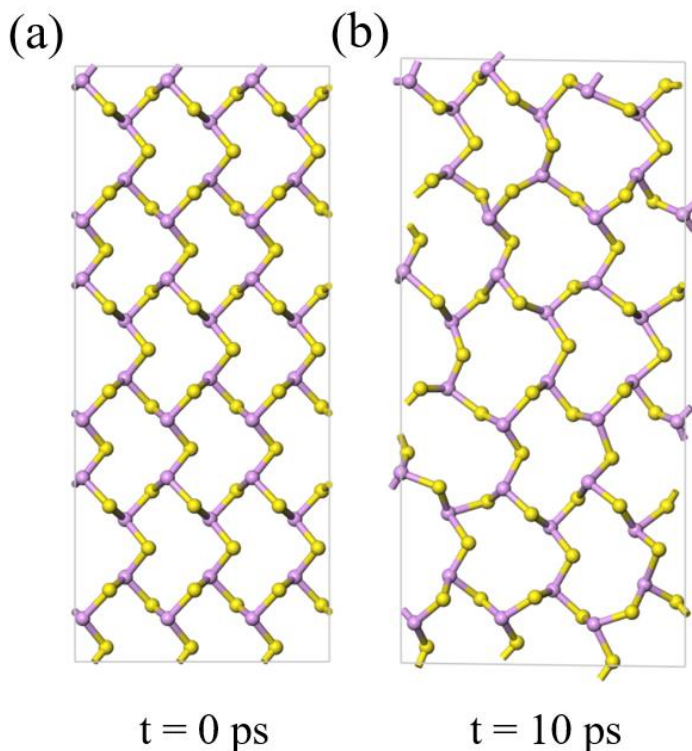


Figure 4.3 *Ab initio* MD snapshots of the α -P₂S₃ supercell structures at temperature $T = 1000$ K under ambient pressure at time $t = 0$ ps (a) and $t = 10$ ps (b).

To further verify the chemical stability of the structure in air, *ab initio* MD simulations of α -P₂S₃ crystal exposed to very high pressure gases (O₂, N₂, H₂O and H₂) at temperature $T = 1000$ K were conducted (Figure 4.4). In our MD simulations, the number density of gas molecules was $57.5 \times 10^{25} \text{ m}^{-3}$. Such a high gas pressure was also used to study oxidation of graphene¹⁴⁶ and phosphorene¹⁴⁷ with MD simulations. The pristine α -P₂S₃ structure was preserved under these very high gas pressure for 10 ps (Figure 4.4), indicating its chemical stability in air at least above room temperature.

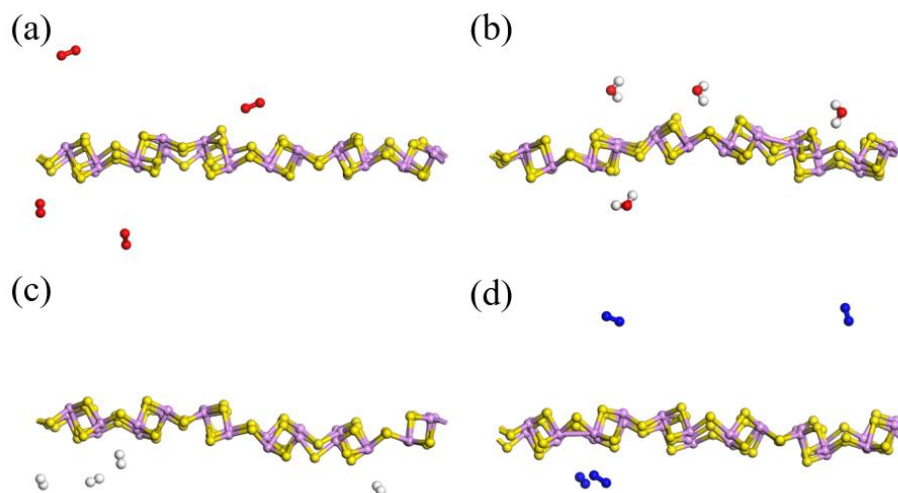


Figure 4.4 *Ab initio* MD snapshots of the α -P₂S₃ supercell structures exposed to the high pressure oxygen gas (a), water vapour (b), hydrogen gas (c), and nitrogen gas (d) at temperatures $T = 1000$ K.

In Figure 4.5, it shows the quasiparticle and DFT band structures and density of states of the 2D α -P₂S₃ crystal. By using the GW method, the calculations showed that the α -P₂S₃ structure is a semiconductor with a wide indirect band gap of 4.55 eV (PBE functional based calculations underestimate the band gap by 2.05 eV). The valence band maximum (VBM) is composed of mainly the orbitals of sulfur atoms, while the conduction band minimum (CBM) is more or less evenly contributed by the orbitals of phosphorus and sulfur atoms (see Figure 4.5).

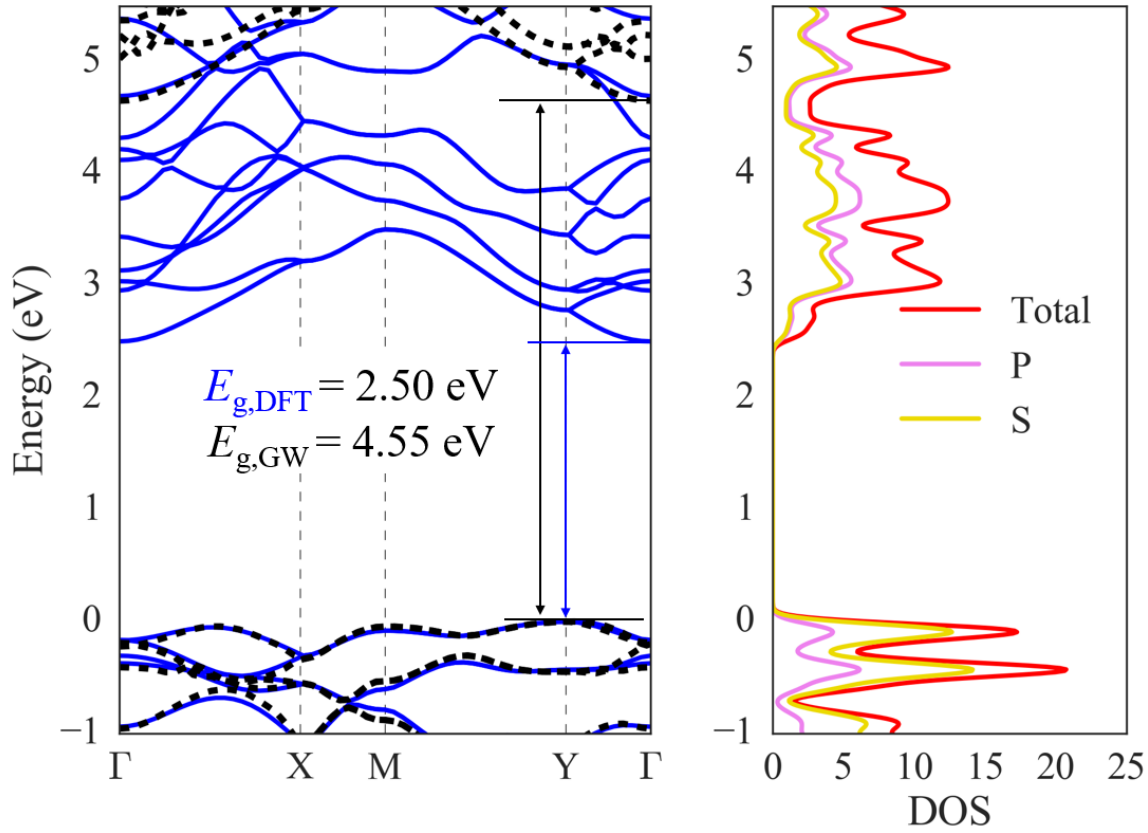


Figure 4.5 Calculated band structure (left) obtained with the PBE functional (blue lines) and the GW method (black dash lines) for the α -P₂S₃ solid. The DOS (right) is obtained with the PBE functional.

Our analysis demonstrates that not only single-layer α -P₂S₃, but also bilayer and its 3D phase constructed by the stacking of α -P₂S₃ monolayers, were stable. The minimum energy stacking for the bilayer and 3D phase are shown in inset figures in Figure 4.6. The binding energy between layers was weak, 0.13 J/m², which was predominantly vdW attraction energy. The DFT band gaps were reduced by 0.14 eV by just stacking P₂S₃ into a bilayer. By stacking P₂S₃ into 3D P₂S₃ crystal, the DFT band gap was further reduced to 2.18 eV. In addition to stacking presented here, it should be noted that the electronic properties of P₂S₃ can be modulated by cutting into P₂S₃

nanoribbons or rolling up to form P_2S_3 nanotubes, or by applying strain field, expanding its potential applications in 2D electronics.

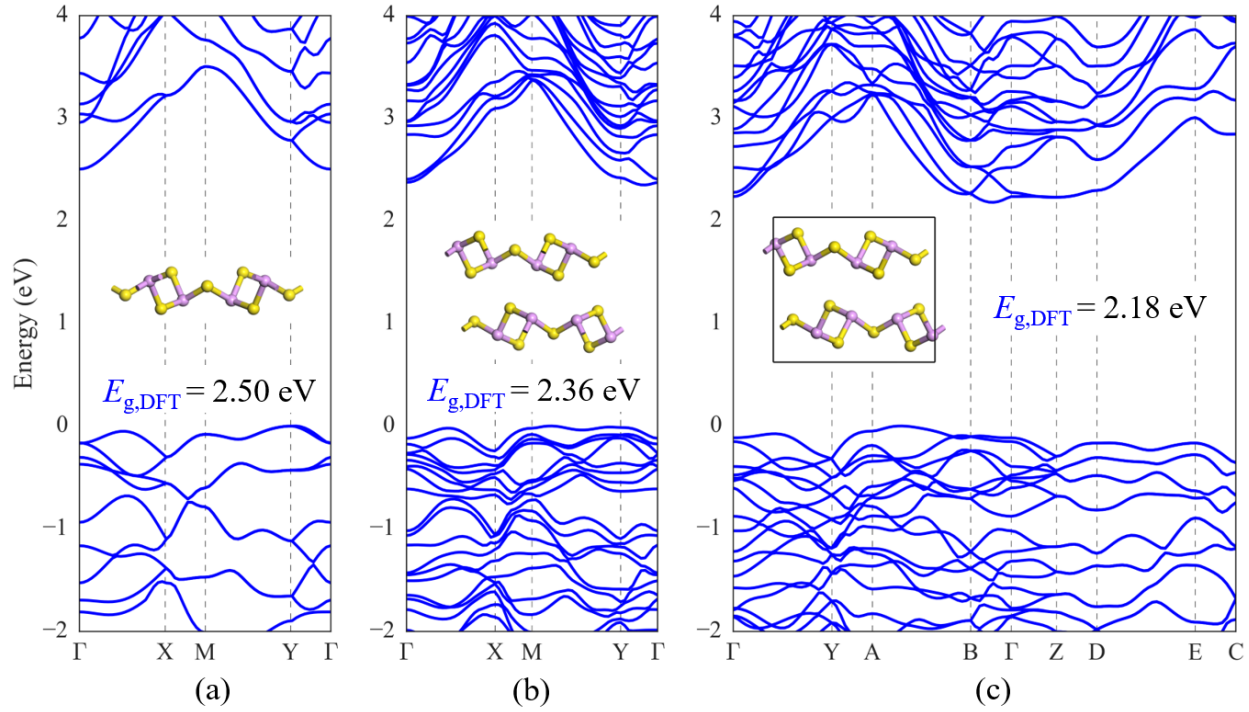


Figure 4.6 The electronic band structures of the α - P_2S_3 monolayer (a), α - P_2S_3 bilayer (b) and α - P_2S_3 3D crystal, obtained with the PBE functional. Monolayer, bilayer and 3D crystal structures of α - P_2S_3 are shown in inset figures.

4.4 Concluding remarks

In conclusion, we predicted a novel two-dimensional trisulfur dinitride (P_2S_3) crystal with the robust stability above room temperature and under chemical environments through *ab initio* simulations. Band structures calculated using the GW method indicate that 2D P_2S_3 crystal is a semiconductor with a wide indirect band gap of 4.55 eV. As the first 2D crystal composed of phosphorus and sulfur, the P_2S_3 solid can also form stable bilayer, 3D layered solid and nanoribbon

structures. These structures with tunable band structures shed light on the applications for the emerging field of 2D electronics.

Chapter 5 The Catalytic Effect of H₂O on the Hydrolysis of CO₃²⁻ in Hydrated Clusters and Its Implication to the Humidity-driven CO₂ Air Capture

5.1 Introduction

The ability of an “inert” solvent to affect the kinetics and thermodynamics of a chemical reaction has been known for over 150 years.¹⁵² Considerable efforts have been devoted to understand the role of solvents in bulk solutions.^{153–155} Recently, the solvent effect in nanometer sized clusters or in nanoscale confinement has attracted increasing interest,^{156–160} due to its ubiquity and importance in various biological and chemical processes.^{161–164} Unlike the ion hydration in the bulk solution, the high ratio of ions to water molecules in nanoscale clusters and cavities could render the hydration shells incomplete. The hydrolysis of ions with these incomplete hydration shells could be significantly different from that in bulk water.

On the other hand, the development of efficient absorbents that can easily switch between absorption and desorption, has been of paramount importance for many processes. For example, direct air capture of CO₂ represents a promising carbon negative technology, and the major challenge of developing an efficient absorbent is not how to absorb CO₂, but how to release it with very low energy cost. This essentially requires a reversible chemical reaction that can be triggered by a simple environmental variable. Lackner et al.⁴⁵ discovered that an anionic exchange resin (IER) washed by carbonate solution can efficiently capture CO₂ from ambient air when it is dry, while release CO₂ when it is wet, as shown in Figure 5.1. A better understanding of the hydrolysis of CO₃²⁻ in hydrated clusters is of great importance for understanding of such a novel humidity-swing reaction with very low energy cost.

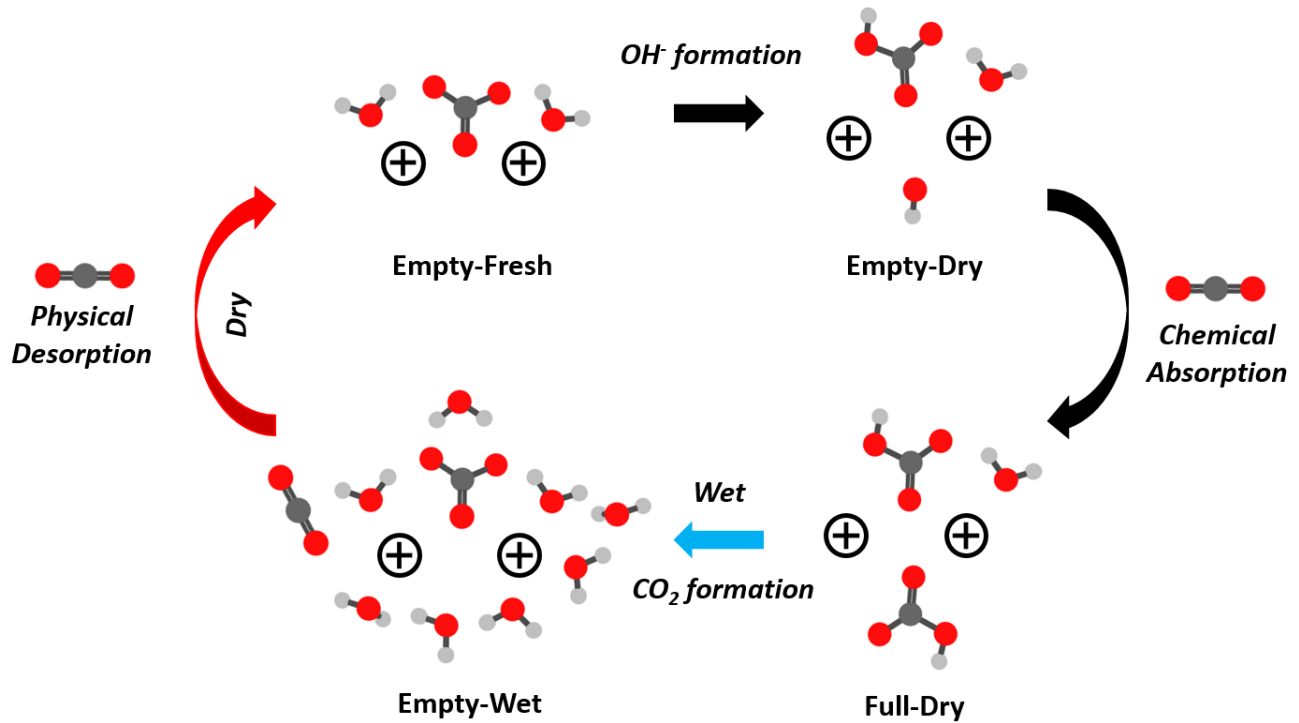
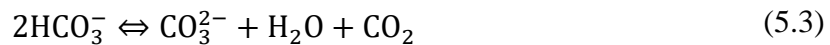
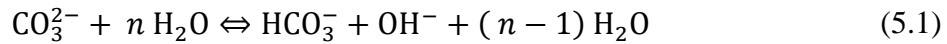


Figure 5.1 Humidity driven CO₂ absorption/desorption on IER. Empty-Fresh state: dry sorbent with only a few water molecules neighboring each carbonate ion. Empty-Dry state: OH⁻ ion and HCO₃⁻ ion are formed by the hydrolysis of CO₃²⁻ in the dry condition. Full-Dry state: the full-loaded sorbent in the dry condition. OH⁻ formation and chemical absorption of CO₂ (Eqs. 5.1-5.2) represent the absorption process. Empty-Wet state: CO₂ regeneration in the wet condition (Eq. 5.3), which represents the physical desorption of CO₂.

The absorption process (Eqs. 5.1-5.2, dry) and desorption process (Eq. 5.3, wet) are:



Our recent atomistic study^{165,166} showed that the free energy of CO₃²⁻ hydrolysis (Eq. 5.1) is negative when the number of participating water molecules, n , is smaller than about 10. That is,

the chemical reaction shifts to the right hand side (which is against the mass action law) when only a few water molecules surround each carbonate ion, rendering the material ready for CO₂ absorption through Eq. 5.2. With a large number of water molecules presenting, Eq. 5.1 swings to the left hand side like that in a bulk environment. When the fully loaded absorbent (after Eqs. 5.1-5.2) is subsequently placed in a wet environment, Eq. 5.3 releases CO₂ in gas phase, completing the absorption-desorption cycle and direct air capture of carbon dioxide.

While the thermodynamic characteristics of this sorbent have been investigated,^{165,166} the kinetic counterpart still remains to be clarified for such a humidity-swing process. The kinetic information of a chemical reaction (e.g. activation free energy) is particularly important, since only chemical reactions with low activation free energy are able to proceed at a reasonable rate. Therefore, the activation free energy of the hydrolysis of CO₃²⁻ in hydrated clusters of different sizes needs to be investigated using quantum chemical calculations.

In this chapter, the reaction pathways of the hydrolysis of CO₃²⁻ with $n = 1-8$ water molecules (Eq. 5.1) are investigated theoretically. We elucidate how water molecules modulate the reaction pathways of CO₃²⁻ hydrolysis and its underlying mechanism. It is found that the activation free energy of the CO₃²⁻ hydrolysis reaction varies with the number of water molecules, which was qualitatively validated by experiments. In addition, nano-confinement is perhaps not a necessity for the humidity driven CO₂ air capture. It was shown that chemical kinetics is not a speed limiting factor in CO₂ air capture driven by the humidity-swing. Instead, the pore-diffusion of ions is expected to be the time-limiting step. The effect of humidity on the speed of CO₂ air capture was investigated by performing CO₂ absorption experiment using IER with a high ratio of CO₃²⁻ to H₂O molecules. Our theoretical and experimental results will pave the way for designing efficient CO₂ air capture sorbents.

5.2 Computational methods

Global-minimum structural searches for stable reactants and products for the reaction in Eq. 5.1 were carried out using the Minima Hopping algorithm¹⁶⁷ implemented in CP2K¹⁴⁵ at the PBE-D3/DZVP level.^{84,144,168} Subsequently, the stable reactants and products were fully optimized at the B3LYP /6-311+G(2d,2p) level¹⁶⁹ with D3 version of Grimme's dispersion correction with Becke-Johnson damping,¹⁷⁰ using the Gaussian 09 package.¹⁴⁴ Geometries of all transition states and intermediates were fully optimized at the same level. To account for the effects of the aqueous environment, the activation free energy and reaction free energy in bulk water are calculated with 8 explicit H₂O molecules in a water dielectric using the SMD continuum solvation model.¹⁷¹ The reaction free energy in bulk water calculated is 4.0 kcal/mol, which agrees well with the experimental value (5.0 kcal/mol) at the ambient condition.¹⁷² Frequency calculations have been carried out to check for the nature of the various stationary points and transition states, which were also used for the computation of zero-point, thermal and entropy contributions to free energy at 298 K. The correlation between the stable structures and the transition states is further verified by the intrinsic reaction coordinate calculations.

5.3 Results and discussion

5.3.1 Hydrolysis reaction with $n = 1-5$

Herein, the hydrolysis of CO₃²⁻ with different number of water molecules ($n = 1-5$ in Eq. 5.1) are compared. The optimized structures and the corresponding relative free energy profiles of reaction pathways are presented in Figure 5.2(a) and in Figure 5.2(b), respectively. In order to balance the charge of carbonate anion, two mobile sodium cations are introduced into the system.

Note that only the most promising reaction pathways (with lowest activation free energy) are presented, due to the increasing number of possible reaction pathways as n increases.

For the reaction with only 1 water molecule, the reaction follows a two-stage route to the product: (1) the H₂O molecule migrates to a position where the proton transfer to the neighbor oxygen atom is energetically favorable, forming the intermediates denoted as I-1a. (2) followed by the proton transfer through the transition state TS-1 to the product P-1.

For the reaction with 2-5 H₂O molecules, a three-step route to the product is likely. The first step is the same with the reaction with 1 H₂O molecule. However, through the transition states (TS-2, TS-3, TS-4 and TS-5), the proton transfer reactions leads to intermediates (I-2b, I-3b, I-4b and I-5b), followed by the migration of ions and H₂O molecules to form the final product. One notes that the migrations of H₂O molecules and ions proceed with little or no barrier, due to the absence of chemical reaction.

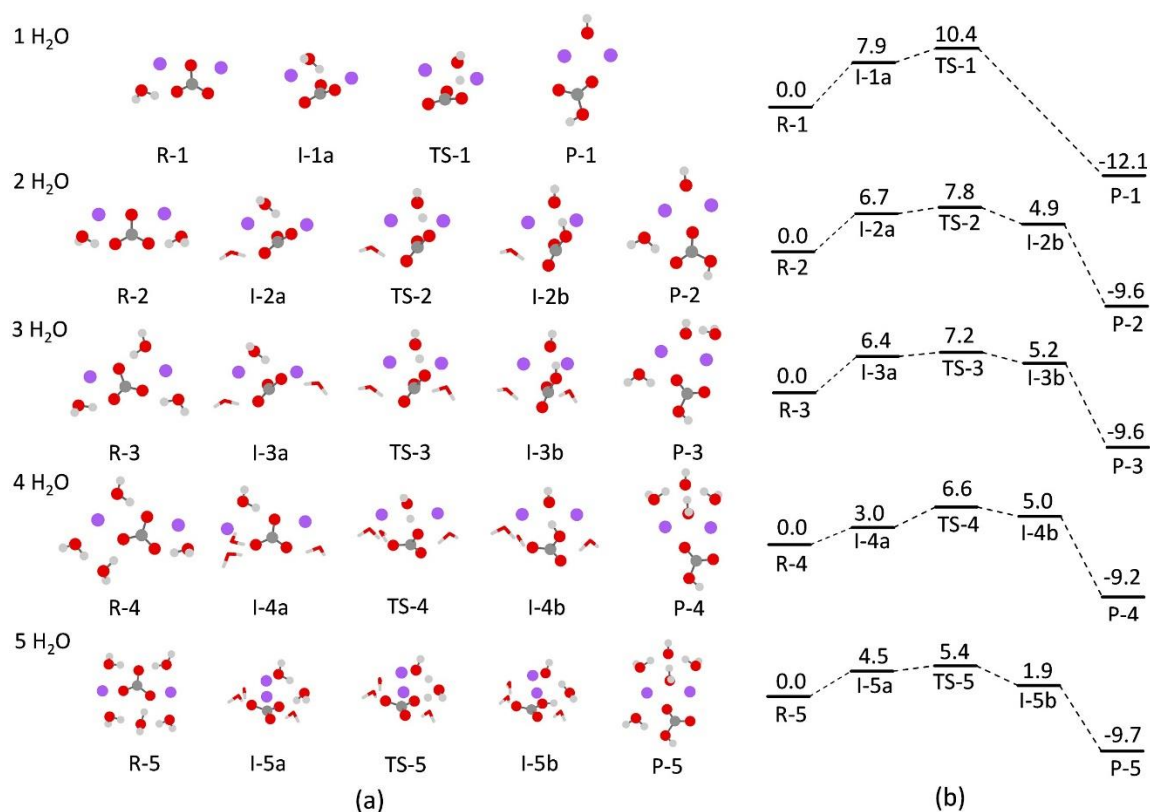


Figure 5.2 (a) Reactants, intermediates, products and transition states for the reaction in Eq. 5.1 ($n=1-5$). (b) Relative free energy profiles (in kcal/mol) for the hydration of CO_3^{2-} with 1-5 water molecules. For transition states and intermediate states, the sodium ions, carbonate ions, bicarbonate ions, hydroxyl ions and the water molecules directly involved in reaction are visualized with the ball-and-stick model, while the water molecules do not directly take part in the reaction are visualized with the tube model. For reactants and products, all species are visualized with the ball-and-stick model. The same visualization protocol is adopted in Figure 5.4.

The activation free energy decreases as n grows from 1 to 5, as shown in Figure 5.3. The reaction free energy increases by 2.5 kcal/mol as n grows from 1 to 2. However, the reaction free energy remains more or less the same as n rises from 2 to 5.

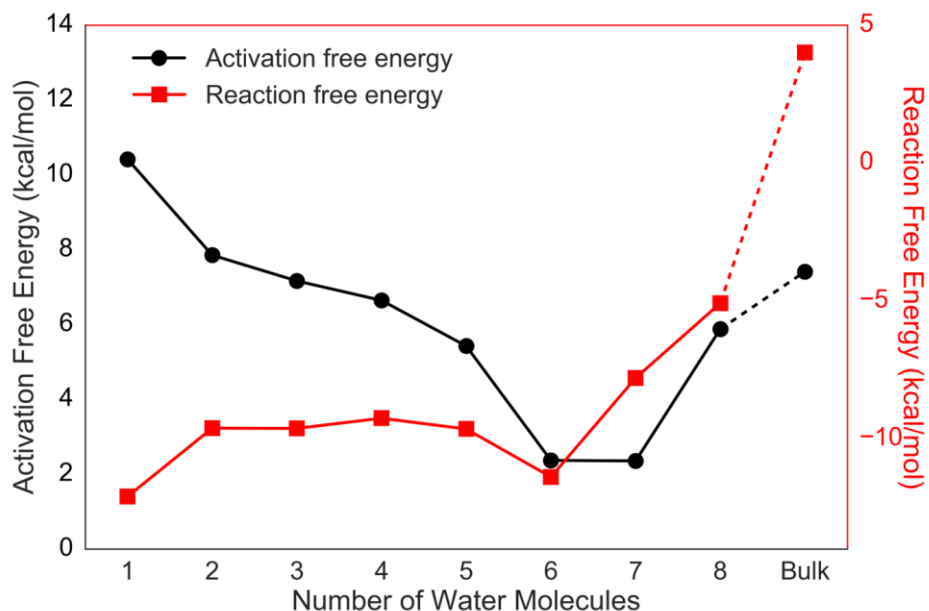


Figure 5.3 The activation free energy (in black) of Eq. 5.1 as a function of the number of H₂O molecules; the reaction free energy (in red) of Eq. 5.1 as a function of the number of H₂O molecules. The activation free energy and reaction free energy in bulk water are calculated with 8 explicit H₂O molecules using the SMD continuum solvation model.¹⁷¹

5.3.2 Hydrolysis reaction with $n = 6-8$

Here, we consider the hydrolysis of CO₃²⁻ with $n = 6-8$ water molecules for comparison. The optimized structures of species involved in the hydrolysis reactions and the corresponding relative free energy profiles of reaction pathways are shown in Figure 5.4(a) and in Figure 5.4(b), respectively.

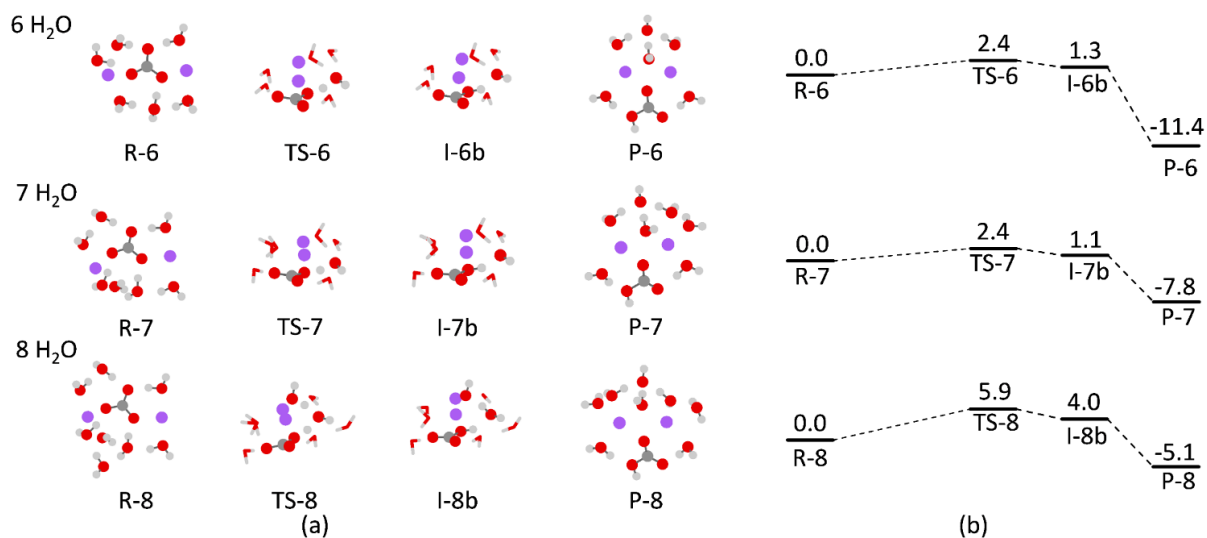


Figure 5.4 (a) Reactants, intermediates, products and transition states for the reaction in Eq. 5.1 ($n = 6-8$). (b) Relative free energy profiles (in kcal/mol) for the hydration of CO_3^{2-} with 6-8 water molecules.

For $n = 1-5$ water molecules, all the reactants follow a stepwise pathway to the transition state through the intermediates (I-1a, I-2a, I-3a, I-4a and I-5a). However, for the reactions with 6-8 H₂O molecules, the reactants (R-6, R-7 and R-8) undergo a proton transfer directly leading to the transition state, with overall lower activation free energy, as shown in Figure 5.3.

For the reactions with $n = 6$ and $n = 7$, the single proton transfer occurs, i.e. only one water molecule is involved in the proton transfer reaction. While for $n = 5$ and $n = 8$, the water mediated double proton transfer is observed. Counterintuitively, the single proton transfers with $n = 6$ and $n = 7$ have a much lower activation free energy than the water-mediated proton transfers with $n = 5$ and $n = 8$, since water-mediated proton transfer is known to lower the energy barrier of proton transfer reactions.^{173–175}

5.3.3 Comparison with the hydrolysis reaction in the bulk water ($n \gg 1$)

Without losing generality, the activation free energy and reaction free energy in bulk water ($n \gg 1$) are calculated with 8 explicit H₂O molecules in a water dielectric using the SMD continuum solvation model,¹⁷¹ as shown in Figure 5.3. Meanwhile, the reaction free energy in bulk water is deduced as 4.0 kcal/mol, a good agreement with the experimental value (5.0 kcal/mol) at the ambient condition.¹⁷² The activation free energy in bulk water is slightly higher than the barrier in reaction with 8 water molecules.

5.3.4 The driving force of the change in activation free energy.

To understand the driving force of the change in activation free energy with different number of water molecules, we decompose the activation free energy into enthalpic and entropic components, as shown in Figure 5.5(a). Clearly, the change of activation free energy is dominated by the change in its enthalpic component, which is discussed in detail in the following. The binding enthalpy of adding one H₂O to reactants, transition states and products of the reactions with n water molecules can be calculated by $\Delta H_n = H_{X_{n+1}} - H_{X_n} - H_{H_2O}$, shown in Figure 5.5(b). For $n = 1-5$, the binding enthalpy of an extra H₂O to transition states are generally lower than that of reactants. That is, water molecules adding to the system tend to stabilize the transition state structure more than the reactants, resulting in the drop of activation free barrier for $n = 1-6$. For $n = 7$, the binding enthalpy of an extra H₂O to transition state is much higher than that of reactant, which means that the extra H₂O molecule tends to stabilize the reactant more than it does to the transition state. As a result, the activation barrier increases abruptly as n grows from 7 to 8.

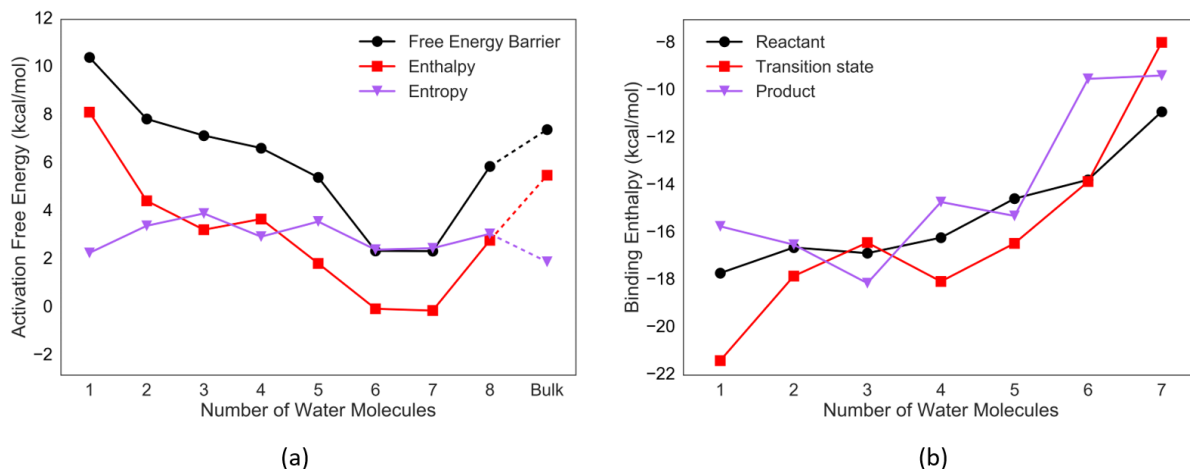


Figure 5.5 (a) The enthalpic (in red) and entropic (in purple) components of the activation free energy of Eq. 5.1 as a function of the number of H₂O molecules. (b) Binding enthalpy of adding one H₂O to reactants (in black), transition states (in red) and products (in purple) of the reactions with n water molecules.

5.3.5 Implication to the humidity driven CO₂ air capture.

The binding enthalpy of adding one H₂O to reactants generally increases as the cluster size increases, as shown in Figure 5.5(b). That is, water molecules bind more firmly with smaller ion clusters. As a result, for two different scenarios of the adsorption of H₂O on CO₃²⁻ anchored on the surface of a porous material at low humidity (Figure 5.6), the uniformly adsorption case is enthalpically favorable. Obviously, the uniformly adsorption case is entropically favored as well. Hence the water molecules tend to be more or less uniformly clustered around CO₃²⁻ ions anchored on the surface of a material at low humidity – although such a reaction system is nanometer-sized, it does not require nano-confinement. In these nanometer-sized hydrated clusters, the CO₃²⁻ hydrolysis reactions are able to spontaneously generate OH⁻ ions that are ready to capture CO₂ from air at room temperature at low humidity. The employment of a nanoporous material helps to maximize the surface area (and hence the anchored CO₃²⁻ density) for higher efficiency air capture

of CO₂ (as long as the carbonate ions are anchored uniformly and firmly), but the confinement from nanopores may not be a required condition for the humidity-swing hydrolysis reaction, contrary to the former proposal¹⁶⁵ and could extend practical applications.

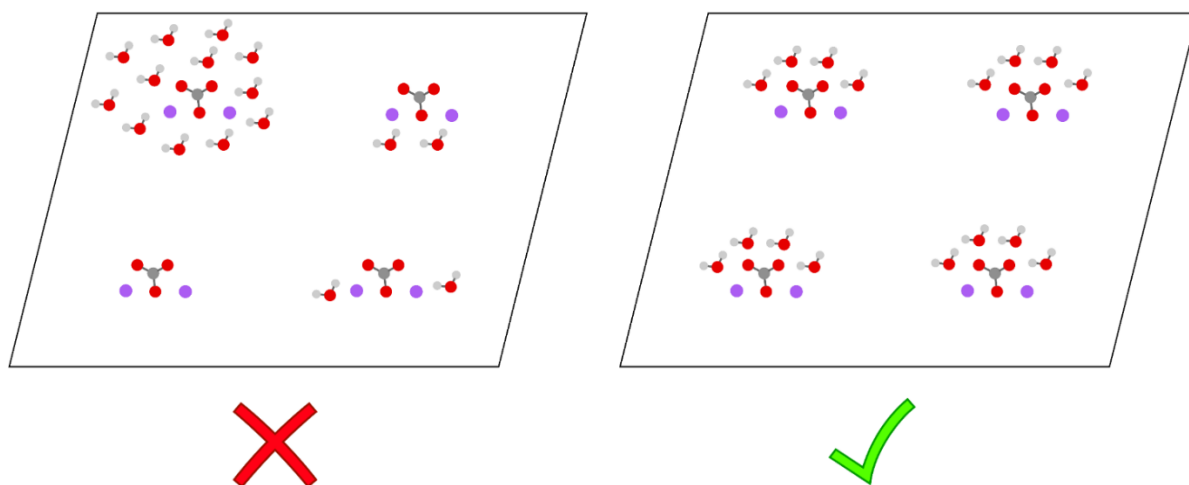


Figure 5.6 Two different scenarios of the adsorption of H₂O on CO₃²⁻ anchored on the surface of a porous material at low humidity.

Despite the strong catalytic effect of water in basic hydrolysis of CO₃²⁻ was theoretically uncovered, the overall small activation free energies (less than 11 kcal/mol) indicate that the chemical kinetics is not likely to constrain the speed of CO₂ air capture driven by the humidity-swing at room temperature. Instead, the pore-diffusion should be the time-limiting step in the humidity driven CO₂ air capture. In practice, the diffusivity of ions in the ion exchange resin (IER) is related to the humidity. To study the effect of humidity on the speed of CO₂ air capture using IER, we performed a CO₂ absorption experiment using IER which has a high ratio of CO₃²⁻ to H₂O molecules.

An experimental device[†] (Figure 5.7(a)) with humidity control was set up to determine the CO₂ kinetic properties under different humidity conditions. The weight of IER was measured at each humidity condition. The weight change of the sample accounts for the amount of water molecules adsorbed on the surface of the sample. Then the overall ratio of H₂O to CO₃²⁻ was calculated by the weight change. With the known ratio of H₂O to CO₃²⁻, the time to absorb 10 ppm CO₂ was recorded under each humidity conditions (see Figure 5.7(b)). The minimum absorption time was observed when the ratio of H₂O to CO₃²⁻ is about 3:1 to 4:1.

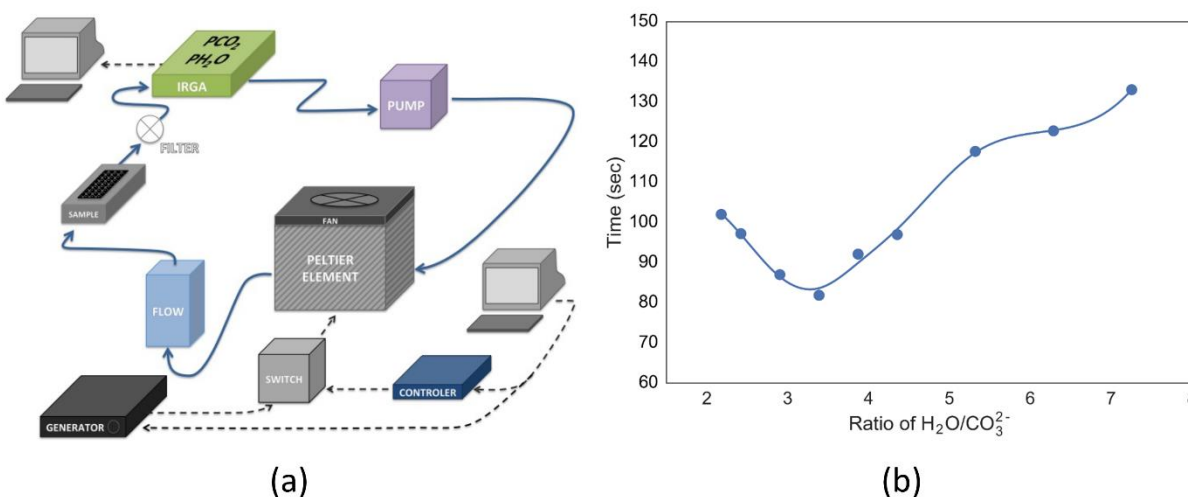


Figure 5.7 (a) Schematic of experimental device. (b) The time to absorb 10 ppm CO₂ as a function of the ratio of H₂O to CO₃²⁻.

[†] The total amount of carbon dioxide on the sample and in the gas volume is constant. We can track the absorption and desorption of carbon dioxide by measuring the carbon dioxide content of the gas. The device can control the water vapor level in the closed gas circulation system. We can determine and characterize the process of CO₂ absorption/desorption by sorbent in the test sample chamber. In the sample chamber, ion exchange resin beads were trapped by two metallic meshes with a well-fitted grid, preventing the beads in between the meshes from moving. All beads can be considered as independent when air went through. The partial pressure of H₂O and CO₂ in the device can be continuously measured by an infrared gas analyzer (IRGA, LI-COR, LI-840).

Two factors may contribute to this phenomenon. (i) The amount of produced OH^- reduces rapidly when the ratio of H_2O to CO_3^{2-} is higher than 6, which has been proved by the reaction free energy change shown in Fig. 3. The IER takes a longer time to absorb 10 PPM of CO_2 because of the presence of less OH^- on the solid surface. CO_2 spends more time in spreading to the inside of the IER to react with OH^- to produce HCO_3^- . The amount of OH^- is the determining factor of the absorption time when the ratio of H_2O to CO_3^{2-} is relatively large. (ii) When the ratio of H_2O to CO_3^{2-} is less than 3, the diffusion rates of ion species (HCO_3^- , CO_3^{2-} , OH^- , H_2O ,) are lower than those of H_2O to CO_3^{2-} is 3 or more than 3. The reduction in the number of water molecules will reduce the rate of ion diffusion and the lower ion diffusion rate may lead to a lower CO_2 absorption rate.²² The IER needs a longer time to absorb 10 PPM of CO_2 because the diffusion rate of ions is the determining factor when the ratio of H_2O to CO_3^{2-} is relatively small.

Our result is able to provide valuable insights to designing efficient CO_2 air-capture sorbents for applications in environment with different humidity (e.g. designing CO_3^{2-} anchored nanoporous materials that facilitate the formation of incomplete hydration shell of CO_3^{2-} within a specific range of humidity that corresponds to, roughly, 3:1-4:1 ratio of water molecules vs. carbonate ion in practice).

5.4 Concluding remarks

The reaction free energy determines the equilibrium point of a chemical reaction, while the activation free energy determines the reaction kinetics. As n increases, the activation free energy of CO_3^{2-} hydrolysis firstly monotonically decreases from 10.4 kcal/mol ($n = 1$) to the minimum value 2.4 kcal/mol ($n = 6$ and $n = 7$), then increases again to 7.4 kcal/mol ($n \gg 1$), as shown in Figure 5.3. The incomplete hydration shells involved in reactions with $n = 6$ and $n = 7$ render the CO_3^{2-} hydrolysis kinetically favorable. Note that the reaction free energies in reactions with $n = 1$ -

8 water molecules are actually negative, indicating that the incomplete hydration shells also render the CO_3^{2-} hydrolysis (Eq. 5.1) thermodynamically favorable.

We showed that chemical kinetics is not likely to constrain the speed of CO_2 air capture driven by the humidity-swing at room temperature. Instead, the pore-diffusion should be the time-limiting step in the humidity driven CO_2 air capture. CO_2 absorption experiment using IER with a high ratio of CO_3^{2-} to H_2O molecules was conducted to study the effect of humidity on the speed of CO_2 air capture. Our result is able to provide valuable insights to designing efficient CO_2 air-capture sorbents. In addition, the catalytic effect of water molecules is not limited to the hydrolysis of CO_3^{2-} with incomplete hydration shells. It is expected that incomplete hydration shells will have similar effects on the hydrolysis of different types of salts: as remarked in recently in the thermodynamics study our work¹⁶⁶ the hydrolysis reactions of several other basic salts are also affected by humidity, and their kinetics may also be studied using the framework proposed in this paper to optimize the design of efficient absorbents.

Chapter 6 Self-assembled Nanocapsules in Water: A Molecular Mechanism Study

6.1 Introduction

Micro- and nano-scale capsules are of great interest due to their potential applications in many fields, including drug delivery, adsorbents, nano-reactors, to name a few. The polymer-based nanocapsules has been extensively studied for drug delivery in the pharmaceutical field.^{176–181} The protective coating in these nanocapsules is usually pyrophoric and easily oxidized, to release the therapeutic substance confined inside¹⁸¹. Substances confined within nanoscale space may exhibit unique physical and chemical properties. Giovambattista et al¹⁸² studied the nanoconfinement induced phase transitions in liquid water. Shi et al¹⁶⁵ investigated the unconventional reversible chemical reaction driven by nanoconfined ion hydration. The nanoconfined space and pressure provided by a nanocapsule enable its potential application as nano-reactor.

Carbon nanotubes (CNTs) are cylindrical forms of graphene layers with either open or close ends.^{183,184} Their outstanding electrical and thermal conductivity, and superior strength-to-density and stiffness-to-density ratios have stimulated increasing interests.^{185–189} Nanocapsules self-assembled by CNTs can be ideal vehicles for drug delivery, since CNTs are non-immunogenic⁸ and can be functionalized.^{9–12}

Herein, we study the self-assembly of one-end-open CNTs into nanocapsules in water, showing that two one-end-open CNTs with different diameters, can coaxially self-assemble into a nanocapsule that is stable in water under ambient conditions. The effect of the normalized radius difference, normalized inter-tube distance, aspect ratio of the CNT pairs are systematically studied. The effect of electric field on the structure of nanocapsules is investigated with *ab initio* molecular

dynamics (AIMD) simulations, showing that nanocapsules can be disassembled by applying an external electric field. This discovery not only reveals a simple yet robust nanocapsule self-assembly mechanism, but also sheds light on the potential applications in drug delivery, nano-reactors, etc.

6.2 Model and method

Molecular dynamics (MD) calculations were performed using the LAMMPS code,⁹⁶ for the self-assembly of one-end-open CNTs into nanocapsules in an orthorhombic water box under ambient temperature ($T = 300$ K) and pressure ($P = 1$ bar). The straight part of the one-end-open CNT was described by Morse bonds, harmonic valence angles, harmonic torsion angles and Lennard-Jones (L-J) 12-6 pair interactions.¹⁹⁰ The cap of the one-end-open CNT was fixed rigid, since its deformation during the self-assembly process was negligible. Water molecules were modeled by the TIP3P-ew model¹⁹¹ and the long range electrostatic interactions were calculated using the PPPM algorithm.¹⁹² Following Hummer et al.,¹⁹³ the interactions between CNTs and water molecules were described by a L-J potential between oxygen and carbon. The equation of motion was solved with a velocity Verlet algorithm, using a time step of 1.0 fs, which led to stable dynamics trajectories.

A pair of one-end-open CNTs were initially coaxially aligned (constrained) with their open-end facing each other (see Figure 6.1). The initial constrained distance between the open ends of two CNTs was 2 Å. The system with constrained CNTs in water was first equilibrated at 300 K and 1 atmospheric pressure with the NPT (constant number of particles, constant pressure and constant temperature) ensemble for 500 ps. Constraints on CNTs were removed after the equilibration step such that they were free to move during the self-assembly process.

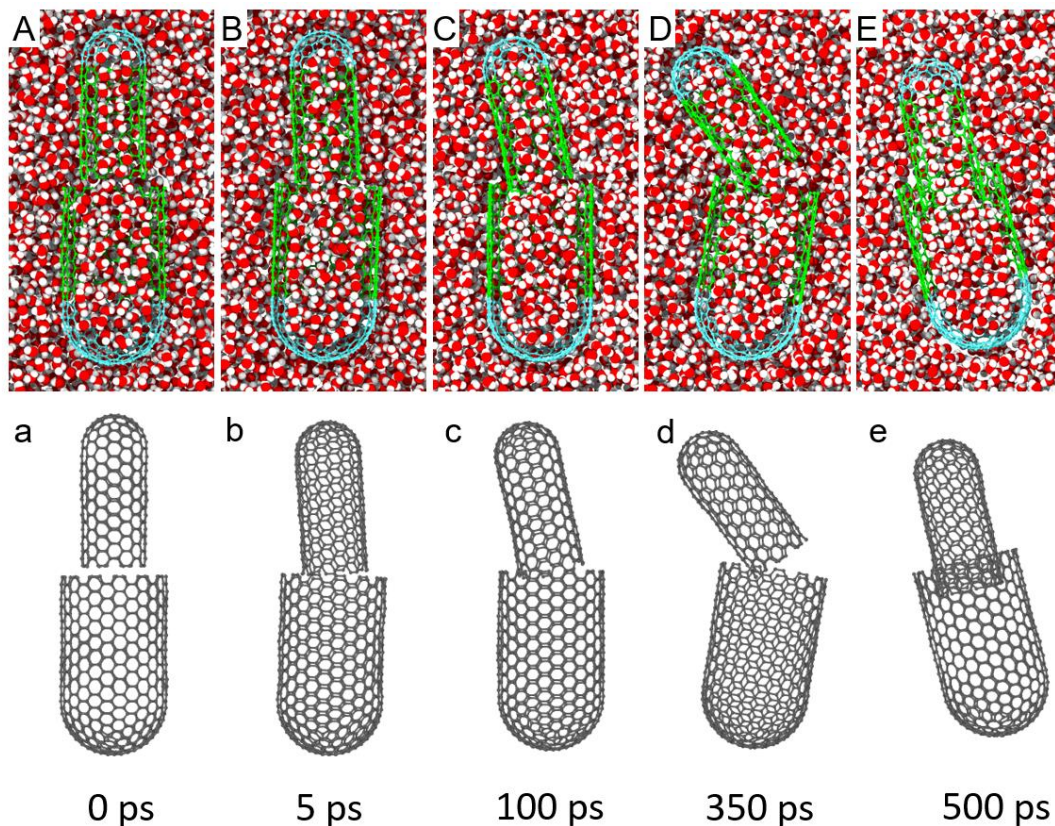


Figure 6.1 Snapshots of the self-assembly process of the nanocapsule from one-end-open (8,8) and (13,13) CNTs. In A, B, C, D and E, nanocapsules are sliced in half to show the water molecules inside. The rigid caps (A, B, C, D, E) are marked in cyan, and the straight regions described by the Morse bond model are marked in green. While in a, b, c, d and e, one-end-open CNTs are marked in grey and water molecules are not displayed for clarity.

To study the effect of electric field on the structure of nanocapsules, *ab initio* molecular dynamics simulations (cf. Figure 6.8) were performed at the PBE⁸⁴/GTH-DZVP¹⁴⁴ level in the NVT (constant number of particles, constant volume and constant temperature) ensemble of the CP2K¹⁴⁵ code. The empirical dispersion correction schemes proposed by Grimme (D3)¹⁷⁰ was used in combination with PBE functional to account for the van der Waals interactions. The external electric field was applied along the axis of nanocapsule. Water solvent outside the

nanocapsule was not considered in *ab initio* molecular dynamics simulations, due to its negligible effect on the electric field response of the nanocapsule.

6.3 Results and discussions

The self-assembly process of the nanocapsule by one-end-open (8, 8) and (13, 13) CNTs is shown in Figure 6.1. After the equilibration step mentioned in section 2, the CNTs were fully solvated (see Figure 6.1(A)). Once the constraints on CNTs were removed, the smaller tube gradually found its way into the larger tube, forming a stable nanocapsule. The self-assembly process was roughly comprised of 3 steps: (1) Two tubes came close to each other, due to inter-tube vdW attractions (Figure 6.1(a-b)). (2) Excessive water molecules were discharged through the opening formed by the rotation of tubes (Figure 6.1(b-d)). (3) Two tubes became coaxially aligned and the smaller tube was partially inserted into the larger counterpart (Figure 6.1(d-e)). In Figure 6.2, it shows the center-of-mass (COM) distance and the vdW interaction energy between two CNTs as a function of time. The three steps of self-assembly process can be clearly identified in Figure 6.2: (1) the COM distance between two CNTs decreased rapidly in the first 15 ps; (2) the COM distance between two CNTs remained more or less the same during the second step; (3) the huge reduction of the COM distance between two CNTs indicates the quick insertion process. The magnitude of inter-tube vdW interaction energy increased as the inter-tube COM distance decreased, confirming that the vdW interaction is the driving force of the nanocapsule self-assembly.

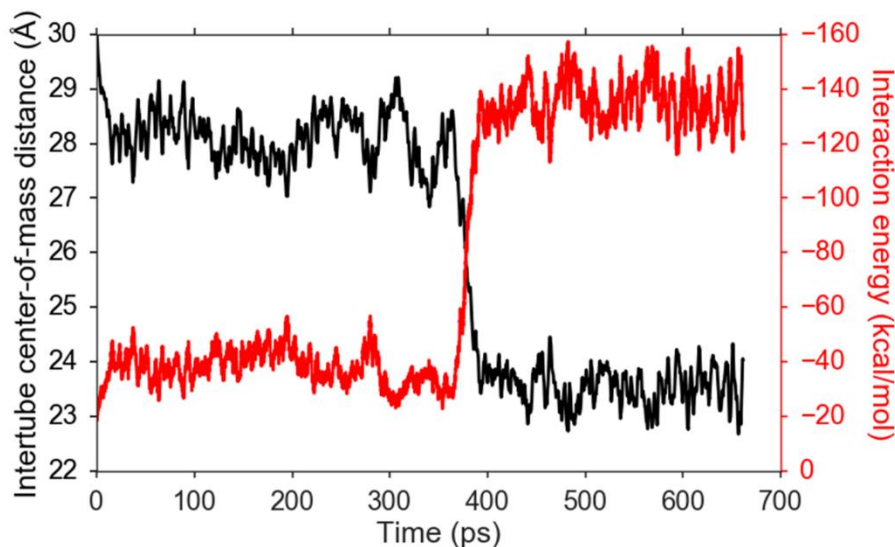


Figure 6.2 The center-of-mass distance (in black) and the interaction energy (in red) between one-end-open (8,8) and (13,13) nanotubes as a function of time. The nanocapsule is formed at around 400 ps.

6.3.1 Effect of normalized radius difference $\Delta R/r_m$

The self-assembly process is expected to be strongly dependent on the inter-tube spacing in the radial direction, since the driving force of the self-assembly is the inter-tube vdW interaction. The inter-tube spacing is characterized by normalized radius difference, denoted as $\Delta R/r_m$, where ΔR is the difference of the radius of the two CNTs; r_m is the distance at which the carbon-carbon L-J potential reaches its minimum ($r_m = 3.81$ Å). The nanocapsule self-assembly processes with different $\Delta R/r_m$ are shown in Figure 6.3, which can be divided into three categories: (1) When $\Delta R/r_m$ was close to 1 ($\Delta R/r_m = 0.89, 0.92$ and 1.06), nanocapsules were successfully assembled. (2) When $\Delta R/r_m$ was relatively large ($\Delta R/r_m = 1.24$), a nanocapsule with less solvent trapped inside was assembled. The solvent escaped from the tubes during the self-assembly process due to large inter-tube spacing. (3) When $\Delta R/r_m$ was fairly large ($\Delta R/r_m = 1.42$) or too small ($\Delta R/r_m = 0.71$), the CNTs failed to form nanocapsules. For $\Delta R/r_m = 1.42$, the self-assembly failed due to

weak inter-tube attraction. For $\Delta R/r_m = 0.71$, small inter-tube spacing rendered the nanocapsule self-assembly energetically unfavorable.

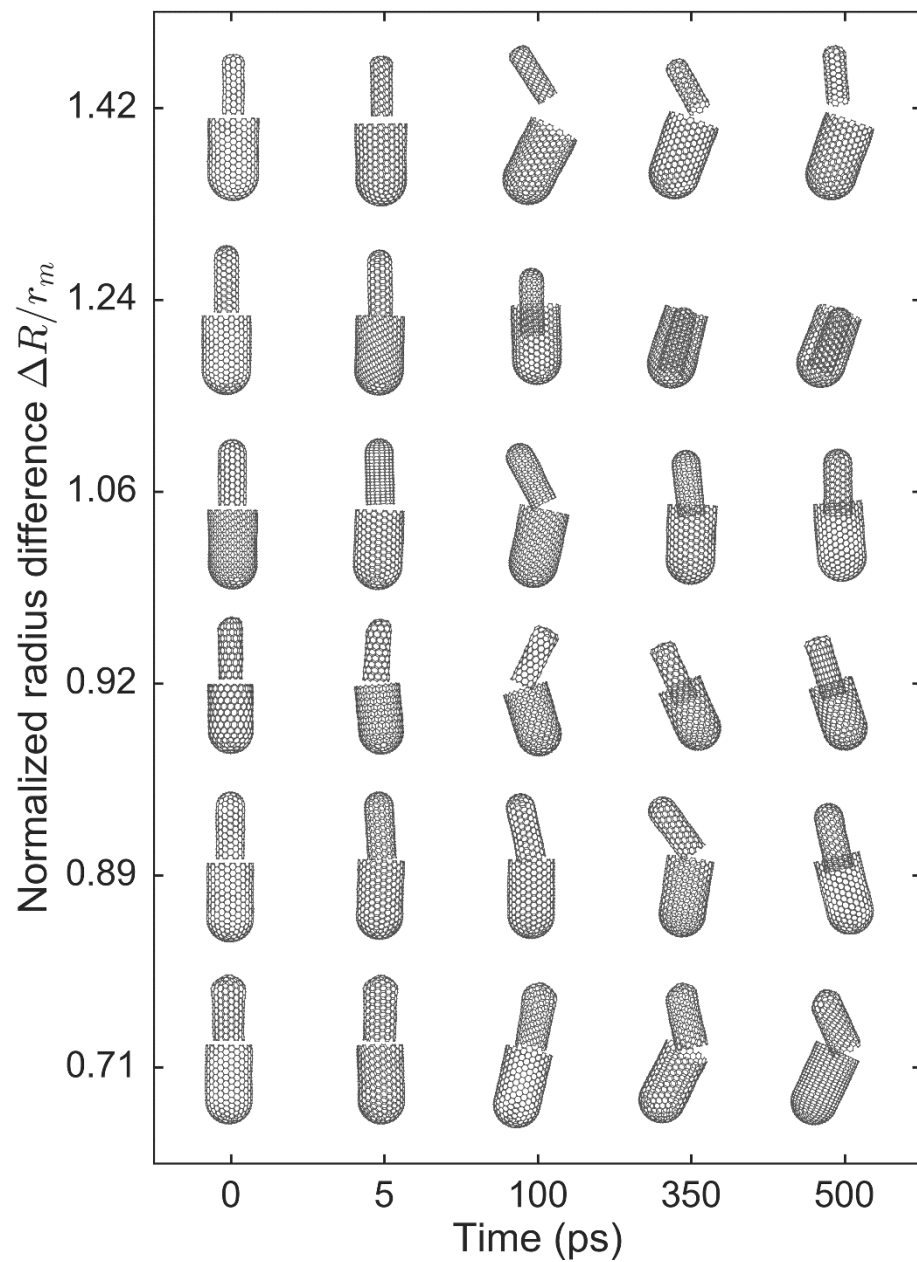


Figure 6.3 Time evolution of the nanocapsule self-assembly by one-end-open CNT pairs with different normalized radius differences ($\Delta R/r_m$).

For $\Delta R/r_m = 0.92$ and $\Delta R/r_m = 0.89$, nanocapsules were self-assembled by zigzag and armchair CNT pairs, respectively. Nanocapsules with similar structures were self-assembled following the aforementioned 3-step route, indicating that the effect of chirality on the assembly process is negligible.

6.3.2 Effect of normalized inter-tube distance D/r_m

Similarly, the initial inter-tube distance is expected to strongly affect the self-assembly of nanocapsules. The normalized inter-tube distance is defined as D/r_m , where D is the initial axial distance of the open-ends of CNTs. The time evolution of nanocapsule self-assembly by one-end-open (8, 8) and (13, 13) CNTs with different D/r_m are shown in Figure 6.4. When the inter-tube distance was relatively small ($D/r_m \leq 1.31$), nanocapsules were successfully self-assembled, due to the relatively strong inter-tube vdW attractions. The self-assembly failed when the inter-tube distance is large ($D/r_m > 1.31$), due to weak inter-tube vdW attraction.

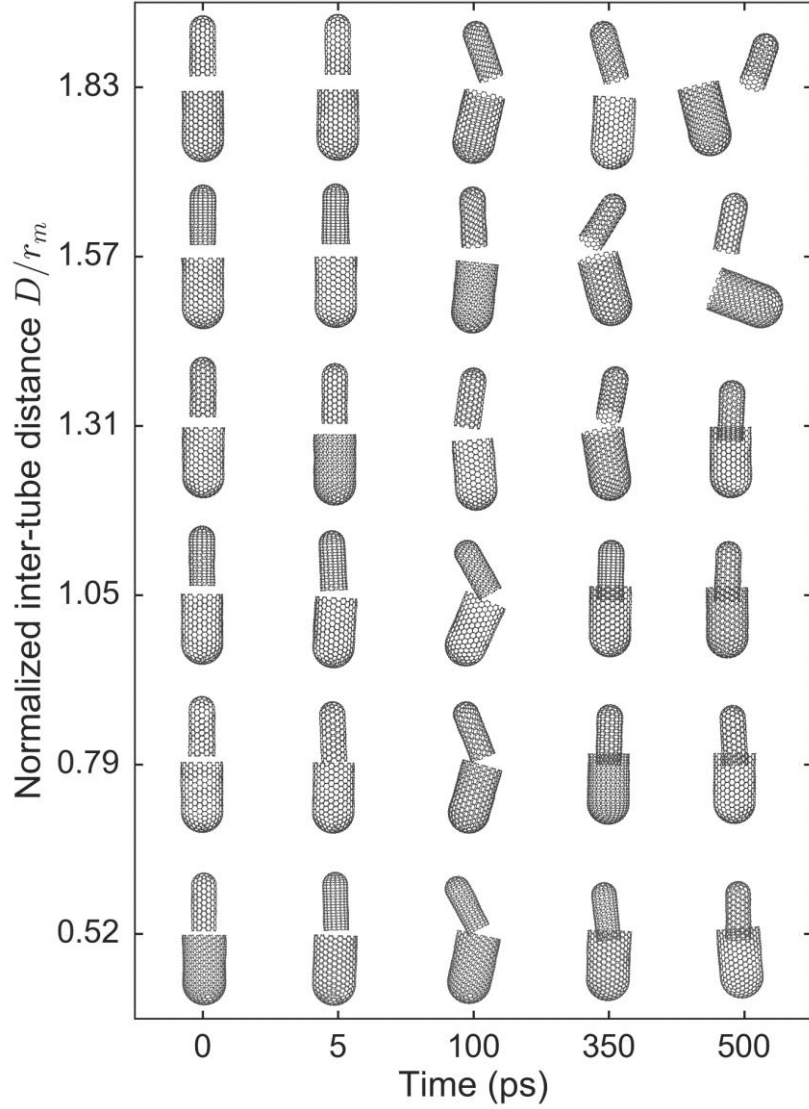


Figure 6.4 Time evolution of the nanocapsule self-assembly by one-end-open CNT pairs ($\Delta R/r_m = 1.06$) with varying normalized inter-tube distances (D/r_m).

6.3.3 Effect of temperature

Figure 6.5 shows the nanocapsule self-assembly map as both D/r_m and $\Delta R/r_m$ are varied. The cases when the nanocapsule was assembled or not at 300 K and 350 K are separated by the solid red line and the dashed red line, respectively. The effect of temperature on the nanocapsule self-assembly can be evaluated by the temperature-induced shift of the parameter space boundary

that distinguishes the successful self-assembly and failed ones. The dividing line shifts left as temperature rises, indicating that the nanocapsule self-assembly was not favored at relatively high temperature, due to the strong thermal fluctuations.

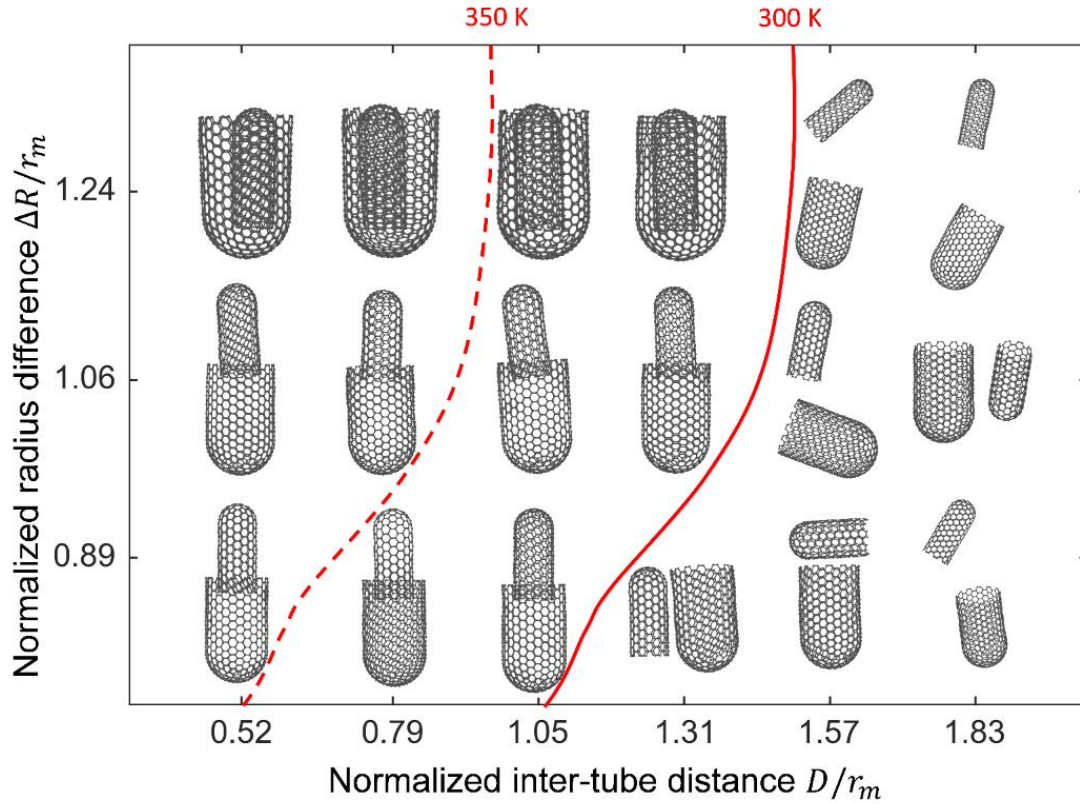


Figure 6.5 The nanocapsule self-assembly map as both normalized inter-tube distance (D/r_m) and normalized radius difference ($\Delta R/r_m$) are varied. Snapshots of systems at time $t=500$ ps are shown. The cases when the nanocapsule is assembled or not at 300 K are separated by the solid red line. The scenarios when the nanocapsule is assembled or not at 350 K are separated by the dashed red line (the systems at 350 K are not shown).

6.3.4 Effect of aspect ratio l/d

The role of aspect ratio of CNT pairs is investigated by comparing the self-assembly of nanocapsules by one-end-open (8, 8) and (13, 13) CNTs with different l/d , where l is the total

length of the two CNTs in a nanocapsule (before assembly); d is the average diameter of the CNTs. In Figure 6.6, it shows that it took much less time for systems with large aspect ratios ($l/d= 6.3$ & 5.2) to form the nanocapsule than the systems with small aspect ratios ($(l/d= 2.5$ & $3.8)$). When $l/d= 2.5$ & 3.8 , the small CNT rotated during the insertion process, prolonging the self-assembly process. On the contrary, an extremely fast insertion of the small tube into the large tube without perceptible rotation was observed when $l/d= 6.3$ & 5.2 , since the longer tubes were more resistant to rotation in water.

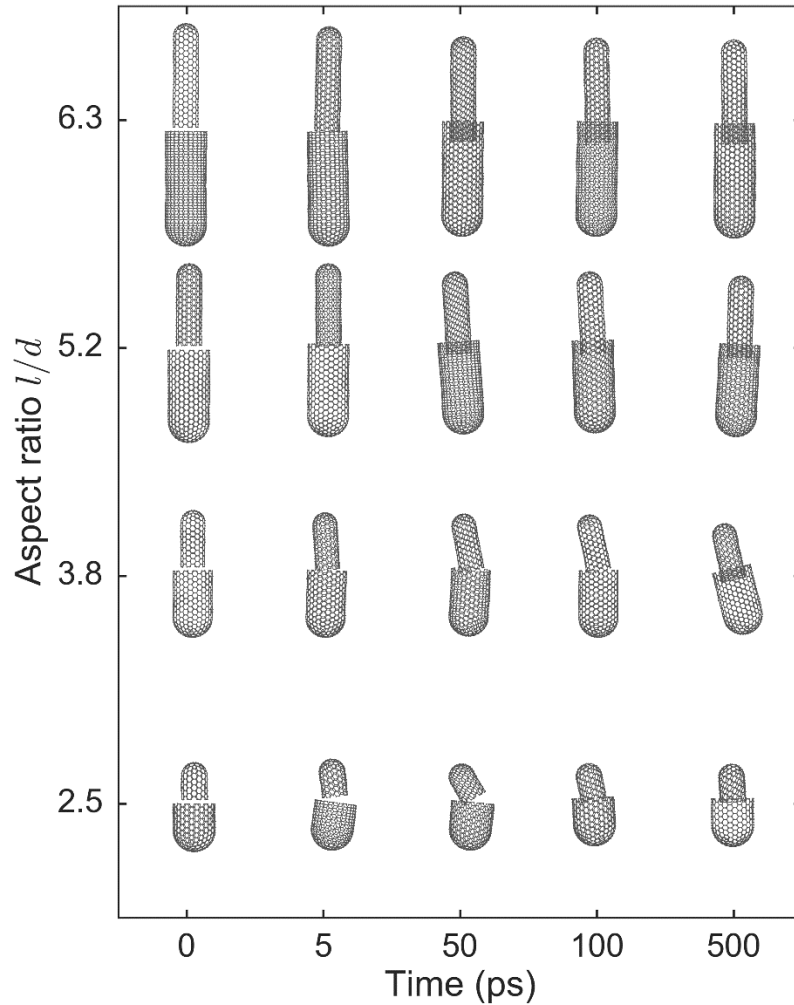


Figure 6.6 Time evolution of the nanocapsule self-assembly by one-end-open CNT pairs ($\Delta R/r_m = 1.06$, $D/r_m = 0.52$) with different aspect ratio, l/d .

Owing to the inter-tube vdW interaction, the pressure of water solvent inside the nanocapsule is expected to be higher than that of the solvent outside. Figure 6.7(a) shows that both the pressure inside the nanocapsule and the magnitude of inter-tube interaction energy increased with increasing l/d . The structure of water inside the nanocapsule with $l/d = 5.2$ before and after the formation of the nanocapsule are shown in Figure 6.7(b) and Figure 6.7(c), respectively. The pressure inside the nanocapsule was on the order of 1 GPa. Such a high pressure triggered the formation of square ice inside the small tube with strong nano-confinement, as shown in Figure 6.7(c). The square ice crystal formed in the nanocapsule is similar to the square ice structures formed in graphene nanocapillaries.¹⁹⁴ Recently, Vasu et al.¹⁹⁵ reported the vdW pressure formed between graphene layers (on the order of 1 GPa) is able to induce chemical reactions of the trapped interlayer molecules. Therefore, the vdW pressure inside the nano-confined space of nanocapsule sheds light on its potential applications as nano-reactors.

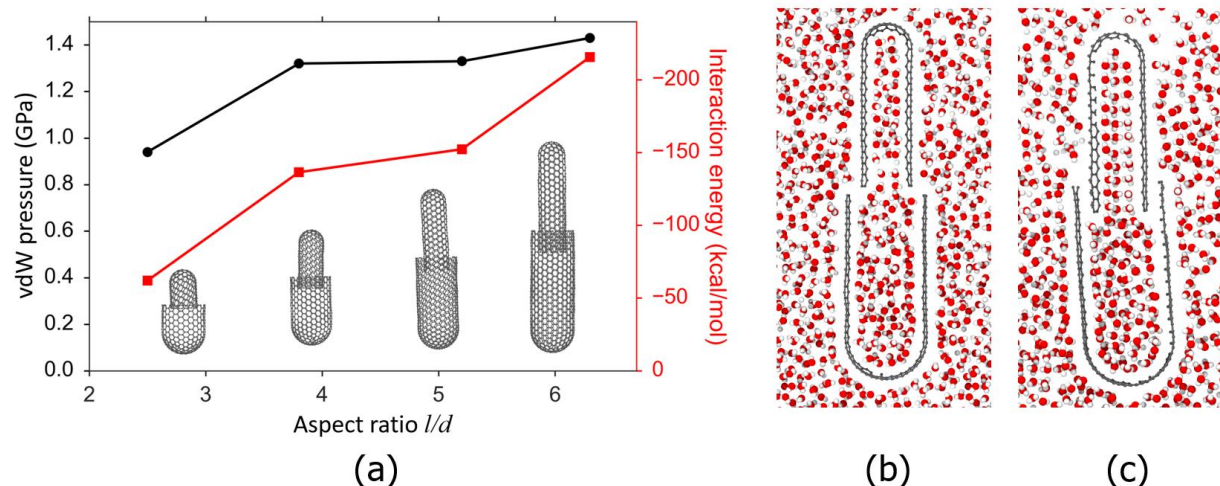


Figure 6.7 (a) The van der Waals pressure inside the nanocapsule and the interaction energy between two CNTs as a function of the aspect ratio, l/d . Comparison of water structure in the CNTs before (b) and after (c) the nanocapsule is formed. Square ice structure is formed in the smaller CNT due to the high van der Waals pressure and the nano-confinement.

It should be noted that in all simulations presented herein, the open ends of the two CNTs were in close proximity and aligned in the beginning of assembly process. If the two open ends were not aligned coaxially but they are still close to each other, with the aid of thermal fluctuation, the CNTs could still self-assemble into a nanocapsule although it takes a longer time. However, if the two CNTs were initially placed far away from each other, it would become difficult for them to attract to each other and assemble. Therefore, in practice, if one randomly places CNTs in a solution, the yield ratio of assembled nanocapsules may be low and depend on the relative density of CNTs. It is known that CNTs in solutions can be effectively aligned with an moderate external electric field, due to the electronic polarization.^{196–198} Therefore, the yield ratio of nanocapsule self-assembly could be increased by applying a moderate external electric field.

6.3.5 Open the nanocapsule by an external electric field

Once the nanocapsule is self-assembled, the structural stability of the nanocapsule is maintained by the inter-tube vdW interaction energy. Therefore, controllable opening and closing of the nanocapsule can be achieved by manipulating the inter-tube interaction energy. The polarization of carbon atoms in CNTs can be triggered by an external electric field. Consequently, the inter-tube interaction can be controlled. For instance, it is shown that the opening and closing of the carbon nanoscrolls can be controlled by an electric field, due to polarization-induced change of surface adhesion.¹⁹⁹ Zhu et al.²⁰⁰ revealed that an external electric field can effectively tune the morphology of graphene nanocages, owing to the polarization of the carbon atoms.

The electric field response of the nanocapsule when the electric field intensity, $E=0.25 \text{ V/\AA}$ and $E=0.75 \text{ V/\AA}$ were studied with AIMD simulations. Time evolution of the morphology of nanocapsules with corresponding electrostatic potential maps under electric field are displayed in

Figure 6.8. Stronger polarization was observed in the nanocapsule under the electric field with $E=0.75 \text{ V/\AA}$, compared to the scenario with $E=0.25 \text{ V/\AA}$. While the relatively weak polarization induced by the electric field with $E=0.25 \text{ V/\AA}$ was not able to open the nanocapsule, the nanocapsule was opened under $E=0.75 \text{ V/\AA}$ in less than 1 ps. Our results show that an external electric field can reduce the inter-tube adhesion in the nanocapsule, enabling facile control of the nanocapsule morphology by tuning the external electric field. Owing to its non-immunogenic nature, chemical tunability via functionalization and electric-field controlled morphology, nanocapsules self-assembled by one-end-open CNTs can be ideal vehicles for drug delivery.

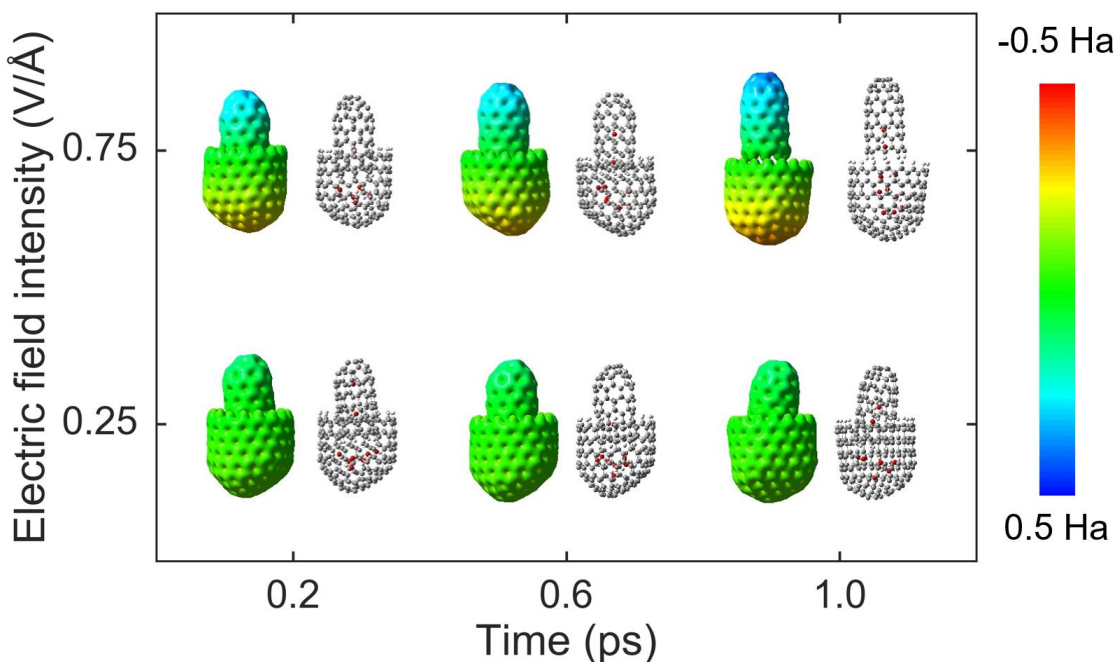


Figure 6.8 The electric field response of the nanocapsule when $E=0.25 \text{ V/\AA}$ and $E=0.75 \text{ V/\AA}$. The electrostatic potential (ESP) maps and the structures of the nanocapsule at $t=0.2 \text{ ps}$, 0.6 ps and 1 ps are shown.

6.4 Concluding remarks

In summary, molecular dynamics simulations showed that one-end-open CNTs pairs with proper radius difference can coaxially self-assemble into a nanocapsule. The nanocapsules formed are stable in aqueous solution in ambient conditions and the pressure inside the nanocapsule is much higher than the pressure in the aqueous solution, due to the vdW attractions between the CNT pairs. The effect of the normalized radius difference, normalized inter-tube distance and aspect ratio of the CNT pairs were systematically explored. AIMD simulations showed that nanocapsules can be opened by applying an external electric field, due to the polarization of the CNT pairs. Our results have general implications on fabricating nanocapsules with various building blocks such as nanotubes (e.g. open-ended CNTs), nano-bowls (e.g. $C_{50}H_{10}$ fullerene bowls), etc. In addition, the nanocapsules can be opened via external electric field, which sheds light on their potential applications in drug-delivery, nano-reactors, etc.

Chapter 7 Conclusions and Future Work

7.1 Concluding remarks

In this thesis, atomistic modelling methods have been applied to address the aforementioned challenges of research in low-dimensional materials. The discoveries and advances are summarized as follows:

We present a reactive force field (ReaxFF) for phosphorus and hydrogen, which provides an accurate description of the chemical and mechanical properties of pristine and defected black phosphorene. A 60° angle correction term is added which significantly improves the description of phosphorus clusters. ReaxFF for P/H is transferable to a wide range of P/H systems including bulk black phosphorus, blue phosphorene, phosphorus clusters, phosphorus hydride molecules, hydrogenated phosphorene nanoribbons and phosphorene nanotubes. Emphasis has been placed on acquiring a good description of mechanical response of black phosphorene with different types of defects. Compared to the SW potential for phosphorene, ReaxFF for P/H systems provides a notable improvement in the description of the cohesive energy, mechanical response of pristine and defected black phosphorene and the thermal stability of phosphorene nanotubes. A counterintuitive phenomenon was observed that single vacancies weaken the black phosphorene more than relatively more unstable double vacancies. It was shown that the mechanical response of black phosphorene is more sensitive to defects in the zigzag direction than the armchair direction. Straightforward extensions to the heterogeneous systems, including oxides, nitrides, etc., enable the ReaxFF parameters for P/H systems to build a solid foundation for the simulation of a wide range of P-containing materials.

A new two-dimensional S_3N_2 crystal with distinctive structures and outstanding properties was proposed. Band structures calculated using the GW method indicate that 2D S_3N_2 crystal is a wide, direct band-gap (3.92 eV) semiconductor with a small hole effective mass. The anisotropic optical response of 2D S_3N_2 crystal was revealed by GW-BSE calculations. S_3N_2 is the first 2D crystal composed of nitrogen and sulphur. Its fascinating properties could pave the way for optoelectronic applications such as blue or ultra-violet light-emitting diodes (LEDs) and photodetectors.

Inspired by the discovery of S_3N_2 , we predicted a novel P_2S_3 2D crystal with high stability through *ab initio* simulations. Band structures calculated using the GW method indicate that P_2S_3 monolayer is a semiconductor with a wide indirect band gap of 4.55 eV. As the first 2D crystal composed of phosphorus and sulfur, the P_2S_3 solid can also form stable bilayer, 3D layered solid and nanoribbon structures. These structures with tunable band structures shed light on the applications for the emerging field of 2D electronics.

We showed that the hydrolysis reaction is strongly affected by relative humidity. The hydrolysis of CO_3^{2-} with $n = 1-8$ water molecules was studied by *ab initio* method. For $n = 1-5$ water molecules, all the reactants follow a stepwise pathway to the transition state. For $n = 6-8$ water molecules, all the reactants undergo a direct proton transfer to the transition state with overall lower activation free energy. The activation free energy of the reaction is dramatically reduced from 10.4 to 2.4 kcal/mol as the number of water molecules varies from 1 to 6. Meanwhile, the degree of the hydrolysis of CO_3^{2-} is significantly increased compared to the bulk water solution scenario. The incomplete hydration shells facilitate the hydrolysis of CO_3^{2-} with few water molecules (especially for $n = 6$) to be both thermodynamically and kinetically favorable. We showed that chemical kinetics is not likely to be the speed-limiting step of the humidity-driven

CO₂ air capture. The pore-diffusion of ions should be the time-limiting step in the CO₂ air capture driven by humidity-swing. By conducting CO₂ absorption experiment using IER with a high ratio of CO₃²⁻ to H₂O molecules, the effect of humidity on the speed of CO₂ air capture was investigated. Our result can provide valuable insights for designing efficient CO₂ air-capture sorbents.

MD simulations showed that one-end-open CNTs pairs with proper radius difference can coaxially self-assemble into a nanocapsule. The nanocapsules formed are stable in aqueous solution in ambient conditions and the inner pressure of the nanocapsule is much higher than the pressure in the aqueous solution. The effect of the normalized radius difference, normalized inter-tube distance and aspect ratio of the CNT pairs were systematically studied. AIMD simulations showed that nanocapsules can be disassembled by applying an external electric field. Our results shed light on fabricating nanocapsules with various building blocks such as nanotubes, nano-bowls (e.g. C₅₀H₁₀ fullerene bowls), etc. In addition, the nanocapsules can be opened via external electric field, which underpinned their potential applications in drug-delivery, nano-reactors, etc.

7.2 Future work

- **Structure-property relationship of low-dimensional materials**
 - The development of efficient computational tools to provide guidance for the design and fabrication of low-dimensional devices
 - The ReaxFF for P/H developed in this thesis will be applied to investigate the interplay between structure and property for various P/H systems. For example, the effect of defects on the mechanical and thermal properties of phosphorene nanotubes; the mechanical and thermal properties of faceted phosphorene nanotubes and phosphorene buckyballs, etc.

- Extension of the ReaxFF for P/H. For example, ReaxFF for P/H/O will be developed to study the corrosion of phosphorene by oxygen gas and water molecules using reactive molecular dynamics simulations.
- **Applications of low-dimensional materials in energy and environmental engineering**
 - Discovery and design of new low-dimensional materials for applications in energy and environmental engineering
 - Computational screening of low-dimensional materials for catalysis
 - Design chemical routes for synthesizing S_3N_2 and P_2S_3 2D materials
 - Systematic study of the effects of strain, curvature, defects and doping on the electronic, optical and chemical properties of S_3N_2 and P_2S_3
 - Green chemistry by nano-catalysis
 - Build a more comprehensive model which incorporates quaternary ammonium ions and polystyrene backbones for the study of the effect of humidity on the hydrolysis of CO_3^{2-} in CO_2 air capture sorbent.
 - The catalytic effect of water in other acid-base reactions in nanoscale hydrated clusters
 - Self-assembly of high pressure nano-reactors from low-dimensional nanostructures, including nano-bowls, nano-cones, etc.

Bibliography

- (1) Kroto, H. W.; Heath, J. R.; O'Brien, S. C.; Curl, R. F.; Smalley, R. E. C60: Buckminsterfullerene. *Nature* **1985**, *318* (6042), 162–163.
- (2) Park, J.; Pasupathy, A. N.; Goldsmith, J. I.; Chang, C.; Yaish, Y.; Petta, J. R.; Rinkoski, M.; Sethna, J. P.; Abruña, H. D.; McEuen, P. L.; et al. Coulomb Blockade and the Kondo Effect in Single-Atom Transistors. *Nature* **2002**, *417* (6890), 722–725.
- (3) Winkelmann, C. B.; Roch, N.; Wernsdorfer, W.; Bouchiat, V.; Balestro, F. Superconductivity in a Single-C60 Transistor. *Nat. Phys.* **2009**, *5* (12), 876–879.
- (4) Iijima, S. Helical Microtubules of Graphitic Carbon. *nature* **1991**, *354* (6348), 56.
- (5) Staii, C.; Johnson Jr, A.; Chen, M.; Gelperin, A. DNA-Decorated Carbon Nanotubes for Chemical Sensing. *Nano Lett.* **2005**, *5* (9), 1774–1778.
- (6) Banks, C. E.; Davies, T. J.; Wildgoose, G. G.; Compton, R. G. Electrocatalysis at Graphite and Carbon Nanotube Modified Electrodes: Edge-Plane Sites and Tube Ends Are the Reactive Sites. *Chem. Commun.* **2005**, No. 7, 829–841.
- (7) Chou, T.-W.; Gao, L.; Thostenson, E. T.; Zhang, Z.; Byun, J.-H. An Assessment of the Science and Technology of Carbon Nanotube-Based Fibers and Composites. *Compos. Sci. Technol.* **2010**, *70* (1), 1–19.
- (8) Pantarotto, D.; Partidos, C. D.; Hoebeke, J.; Brown, F.; Kramer, E.; Briand, J.-P.; Muller, S.; Prato, M.; Bianco, A. Immunization with Peptide-Functionalized Carbon Nanotubes Enhances Virus-Specific Neutralizing Antibody Responses. *Chem. Biol.* **2003**, *10* (10), 961–966.
- (9) Sun, Y.-P.; Fu, K.; Lin, Y.; Huang, W. Functionalized Carbon Nanotubes: Properties and Applications. *Acc. Chem. Res.* **2002**, *35* (12), 1096–1104.
- (10) Shim, M.; Shi Kam, N. W.; Chen, R. J.; Li, Y.; Dai, H. Functionalization of Carbon Nanotubes for Biocompatibility and Biomolecular Recognition. *Nano Lett.* **2002**, *2* (4), 285–288.
- (11) Sun, Y.-P.; Zhou, B.; Henbest, K.; Fu, K.; Huang, W.; Lin, Y.; Taylor, S.; Carroll, D. L. Luminescence Anisotropy of Functionalized Carbon Nanotubes in Solution. *Chem. Phys. Lett.* **2002**, *351* (5), 349–353.
- (12) Xiao, X.; Li, T.; Peng, Z.; Jin, H.; Zhong, Q.; Hu, Q.; Yao, B.; Luo, Q.; Zhang, C.; Gong, L.; et al. Freestanding Functionalized Carbon Nanotube-Based Electrode for Solid-State Asymmetric Supercapacitors. *Nano Energy* **2014**, *6*, 1–9.
- (13) Novoselov, K. S.; Geim, A. K.; Morozov, S. V.; Jiang, D.; Katsnelson, M. I.; Grigorieva, I. V.; Dubonos, S. V.; Firsov, A. A. Two-Dimensional Gas of Massless Dirac Fermions in Graphene. *Nature* **2005**, *438* (7065), 197–200.
- (14) Zhang, Y.; Tan, Y.-W.; Stormer, H. L.; Kim, P. Experimental Observation of the Quantum Hall Effect and Berry's Phase in Graphene. *Nature* **2005**, *438* (7065), 201–204.
- (15) Morozov, S.; Novoselov, K.; Katsnelson, M.; Schedin, F.; Ponomarenko, L.; Jiang, D.; Geim, A. Strong Suppression of Weak Localization in Graphene. *Phys. Rev. Lett.* **2006**, *97* (1), 016801.
- (16) Novoselov, K. S.; Geim, A. K.; Morozov, Sv.; Jiang, D.; Katsnelson, Mi.; Grigorieva, Iv.; Dubonos, Sv.; Firsov, Aa. Two-Dimensional Gas of Massless Dirac Fermions in Graphene. *nature* **2005**, *438* (7065), 197–200.

- (17) Novoselov, K. S.; Geim, A. K.; Morozov, S. V.; Jiang, D.; Zhang, Y.; Dubonos, S. V.; Grigorieva, I. V.; Firsov, A. A. Electric Field Effect in Atomically Thin Carbon Films. *science* **2004**, *306* (5696), 666–669.
- (18) Lee, C.; Wei, X.; Kysar, J. W.; Hone, J. Measurement of the Elastic Properties and Intrinsic Strength of Monolayer Graphene. *science* **2008**, *321* (5887), 385–388.
- (19) Balandin, A. A.; Ghosh, S.; Bao, W.; Calizo, I.; Teweldebrhan, D.; Miao, F.; Lau, C. N.; others. Superior Thermal Conductivity of Single-Layer Graphene. *Nano Lett.* **2008**, *8* (3), 902–907.
- (20) Lin, Y.-M.; Dimitrakopoulos, C.; Jenkins, K. A.; Farmer, D. B.; Chiu, H.-Y.; Grill, A.; Avouris, P. 100-GHz Transistors from Wafer-Scale Epitaxial Graphene. *Science* **2010**, *327* (5966), 662–662.
- (21) Liu, M.; Yin, X.; Ulin-Avila, E.; Geng, B.; Zentgraf, T.; Ju, L.; Wang, F.; Zhang, X. A Graphene-Based Broadband Optical Modulator. *Nature* **2011**, *474* (7349), 64–67.
- (22) Deng, M.; Yang, X.; Silke, M.; Qiu, W.; Xu, M.; Borghs, G.; Chen, H. Electrochemical Deposition of Polypyrrole/Graphene Oxide Composite on Microelectrodes towards Tuning the Electrochemical Properties of Neural Probes. *Sens. Actuators B Chem.* **2011**, *158* (1), 176–184.
- (23) Kim, K. S.; Zhao, Y.; Jang, H.; Lee, S. Y.; Kim, J. M.; Kim, K. S.; Ahn, J.-H.; Kim, P.; Choi, J.-Y.; Hong, B. H. Large-Scale Pattern Growth of Graphene Films for Stretchable Transparent Electrodes. *nature* **2009**, *457* (7230), 706–710.
- (24) Zhu, Y.; Murali, S.; Stoller, M. D.; Ganesh, K.; Cai, W.; Ferreira, P. J.; Pirkle, A.; Wallace, R. M.; Cychosz, K. A.; Thommes, M.; et al. Carbon-Based Supercapacitors Produced by Activation of Graphene. *Science* **2011**, *332* (6037), 1537–1541.
- (25) Hu, K.; Kulkarni, D. D.; Choi, I.; Tsukruk, V. V. Graphene-Polymer Nanocomposites for Structural and Functional Applications. *Prog. Polym. Sci.* **2014**, *39* (11), 1934–1972.
- (26) Novoselov, K. S.; Jiang, D.; Schedin, F.; Booth, T. J.; Khotkevich, V. V.; Morozov, S. V.; Geim, A. K. Two-Dimensional Atomic Crystals. *Proc. Natl. Acad. Sci. U. S. A.* **2005**, *102* (30), 10451–10453.
- (27) Pacil Ę D.; Meyer, J. C.; Girit, Ę. Ė.; Zettl, A. The Two-Dimensional Phase of Boron Nitride: Few-Atomic-Layer Sheets and Suspended Membranes. *Appl. Phys. Lett.* **2008**, *92* (13), 133107.
- (28) Topsakal, M.; Aktürk, E.; Ciraci, S. First-Principles Study of Two- and One-Dimensional Honeycomb Structures of Boron Nitride. *Phys. Rev. B* **2009**, *79* (11), 115442.
- (29) Mak, K. F.; Lee, C.; Hone, J.; Shan, J.; Heinz, T. F. Atomically Thin MoS_2 : A New Direct-Gap Semiconductor. *Phys. Rev. Lett.* **2010**, *105* (13), 136805.
- (30) Radisavljevic, B.; Radenovic, A.; Brivio, J.; Giacometti, V.; Kis, A. Single-Layer MoS_2 Transistors. *Nat. Nanotechnol.* **2011**, *6* (3), 147–150.
- (31) Li, L.; Yu, Y.; Ye, G. J.; Ge, Q.; Ou, X.; Wu, H.; Feng, D.; Chen, X. H.; Zhang, Y. Black Phosphorus Field-Effect Transistors. *Nat. Nanotechnol.* **2014**, *9* (5), 372–377.
- (32) Liu, H.; Neal, A. T.; Zhu, Z.; Luo, Z.; Xu, X.; Tománek, D.; Ye, P. D. Phosphorene: An Unexplored 2D Semiconductor with a High Hole Mobility. *ACS Nano* **2014**, *8* (4), 4033–4041.
- (33) Fei, R.; Yang, L. Strain-Engineering the Anisotropic Electrical Conductance of Few-Layer Black Phosphorus. *Nano Lett.* **2014**, *14* (5), 2884–2889.

- (34) Buscema, M.; Groenendijk, D. J.; Blanter, S. I.; Steele, G. A.; van der Zant, H. S. J.; Castellanos-Gomez, A. Fast and Broadband Photoresponse of Few-Layer Black Phosphorus Field-Effect Transistors. *Nano Lett.* **2014**, *14* (6), 3347–3352.
- (35) Hong, T.; Chamlagain, B.; Lin, W.; Chuang, H.-J.; Pan, M.; Zhou, Z.; Xu, Y.-Q. Polarized Photocurrent Response in Black Phosphorus Field-Effect Transistors. *Nanoscale* **2014**, *6* (15), 8978–8983.
- (36) Xia, F.; Wang, H.; Jia, Y. Rediscovering Black Phosphorus as an Anisotropic Layered Material for Optoelectronics and Electronics. *Nat. Commun.* **2014**, *5*, 4458.
- (37) Novoselov, K. S.; Fal'ko, V. I.; Colombo, L.; Gellert, P. R.; Schwab, M. G.; Kim, K. A Roadmap for Graphene. *Nature* **2012**, *490* (7419), 192–200.
- (38) Adhikari, B.; Biswas, A.; Banerjee, A. Graphene Oxide-Based Hydrogels to Make Metal Nanoparticle-Containing Reduced Graphene Oxide-Based Functional Hybrid Hydrogels. *ACS Appl. Mater. Interfaces* **2012**, *4* (10), 5472–5482.
- (39) Liu, X.; Antonietti, M. Moderating Black Powder Chemistry for the Synthesis of Doped and Highly Porous Graphene Nanoplatelets and Their Use in Electrocatalysis. *Adv. Mater.* **2013**, *25* (43), 6284–6290.
- (40) Zhang, L.; Shao, J.-J.; Zhang, W.; Zhang, C.; Zheng, X.; Du, H.; Yang, Q.-H. Graphene-Based Porous Catalyst with High Stability and Activity for the Methanol Oxidation Reaction. *J. Phys. Chem. C* **2014**, *118* (45), 25918–25923.
- (41) Zhou, D.; Liu, Q.; Cheng, Q.; Zhao, Y.; Cui, Y.; Wang, T.; Han, B. Graphene-Manganese Oxide Hybrid Porous Material and Its Application in Carbon Dioxide Adsorption. *Chin. Sci. Bull.* **2012**, *57* (23), 3059–3064.
- (42) Sun, Y.; Wu, Q.; Shi, G. Graphene Based New Energy Materials. *Energy Environ. Sci.* **2011**, *4* (4), 1113–1132.
- (43) Gao, H.; Xiao, F.; Ching, C. B.; Duan, H. High-Performance Asymmetric Supercapacitor Based on Graphene Hydrogel and Nanostructured MnO₂. *ACS Appl. Mater. Interfaces* **2012**, *4* (5), 2801–2810.
- (44) Lackner, K. S.; Brennan, S.; Matter, J. M.; Park, A.-H. A.; Wright, A.; Van Der Zwaan, B. The Urgency of the Development of CO₂ Capture from Ambient Air. *Proc. Natl. Acad. Sci.* **2012**, *109* (33), 13156–13162.
- (45) Lackner, K. S. Capture of Carbon Dioxide from Ambient Air. *Eur. Phys. J. Spec. Top.* **2009**, *176* (1), 93–106.
- (46) Wang, T.; Lackner, K. S.; Wright, A. Moisture Swing Sorbent for Carbon Dioxide Capture from Ambient Air. *Environ. Sci. Technol.* **2011**, *45* (15), 6670–6675.
- (47) Born, M.; Oppenheimer, R. Zur Quantentheorie Der Molekeln. *Ann. Phys.* **1927**, *389* (20), 457–484.
- (48) Hohenberg, P.; Kohn, W. Inhomogeneous Electron Gas. *Phys. Rev.* **1964**, *136* (3B), B864.
- (49) Kohn, W.; Sham, L. J. Self-Consistent Equations Including Exchange and Correlation Effects. *Phys. Rev.* **1965**, *140* (4A), A1133.
- (50) van Duin, A. C. T.; Dasgupta, S.; Lorant, F.; Goddard, W. A. ReaxFF: A Reactive Force Field for Hydrocarbons. *J. Phys. Chem. A* **2001**, *105* (41), 9396–9409.
- (51) A Reactive Potential for Hydrocarbons with Intermolecular Interactions. *J. Chem. Phys.* **2000**, *112* (14), 6472–6486.
- (52) Tersoff, J. New Empirical Approach for the Structure and Energy of Covalent Systems. *Phys. Rev. B* **1988**, *37* (12), 6991.

- (53) Go, J.; Bg, B.; H, T.; Wj, M.; Ra, S. Comparison of Cluster and Infinite Crystal Calculations on Zeolites with the Electronegativity Equalization Method (Eem). *J. Phys. Chem.* **1995**, *99* (10), 3251–3258.
- (54) van Duin, A. C. T.; Strachan, A.; Stewman, S.; Zhang, Q.; Xu, X.; Goddard, W. A. ReaxFFSiO Reactive Force Field for Silicon and Silicon Oxide Systems. *J. Phys. Chem. A* **2003**, *107* (19), 3803–3811.
- (55) Liu, L.; Liu, Y.; Zybin, S. V.; Sun, H.; Goddard, W. A. ReaxFF- L G: Correction of the ReaxFF Reactive Force Field for London Dispersion, with Applications to the Equations of State for Energetic Materials. *J. Phys. Chem. A* **2011**, *115* (40), 11016–11022.
- (56) Alder, B.; Wainwright, Te. Phase Transition for a Hard Sphere System. *J. Chem. Phys.* **1957**, *27* (5), 1208–1209.
- (57) Allen, M. P.; Tildesley, D. J. *Computer Simulation of Liquids*; Oxford university press, 1989.
- (58) Rapaport, D. C.; Blumberg, R. L.; McKay, S. R.; Christian, W.; others. The Art of Molecular Dynamics Simulation. *Comput. Phys.* **1996**, *10* (5), 456–456.
- (59) Marx, D.; Hutter, J. *Ab Initio Molecular Dynamics: Basic Theory and Advanced Methods*; Cambridge University Press, 2009.
- (60) Geim, A. K.; Novoselov, K. S. The Rise of Graphene. *Nat. Mater.* **2007**, *6* (3), 183–191.
- (61) De Heer, W. A.; Berger, C.; Wu, X.; First, P. N.; Conrad, E. H.; Li, X.; Li, T.; Sprinkle, M.; Hass, J.; Sadowski, M. L.; et al. Epitaxial Graphene. *Solid State Commun.* **2007**, *143* (1), 92–100.
- (62) Bonaccorso, F.; Sun, Z.; Hasan, T.; Ferrari, A. Graphene Photonics and Optoelectronics. *Nat. Photonics* **2010**, *4* (9), 611–622.
- (63) Bao, Q.; Loh, K. P. Graphene Photonics, Plasmonics, and Broadband Optoelectronic Devices. *ACS Nano* **2012**, *6* (5), 3677–3694.
- (64) Song, Y.; Qu, K.; Zhao, C.; Ren, J.; Qu, X. Graphene Oxide: Intrinsic Peroxidase Catalytic Activity and Its Application to Glucose Detection. *Adv. Mater.* **2010**, *22* (19), 2206–2210.
- (65) Lukowski, M. A.; Daniel, A. S.; Meng, F.; Forticaux, A.; Li, L.; Jin, S. Enhanced Hydrogen Evolution Catalysis from Chemically Exfoliated Metallic MoS₂ Nanosheets. *J. Am. Chem. Soc.* **2013**, *135* (28), 10274–10277.
- (66) Glass, C. W.; Oganov, A. R.; Hansen, N. USPEX—evolutionary Crystal Structure Prediction. *Comput. Phys. Commun.* **2006**, *175* (11), 713–720.
- (67) Lyakhov, A. O.; Oganov, A. R.; Stokes, H. T.; Zhu, Q. New Developments in Evolutionary Structure Prediction Algorithm USPEX. *Comput. Phys. Commun.* **2013**, *184* (4), 1172–1182.
- (68) Wang, Y.; Lv, J.; Zhu, L.; Ma, Y. CALYPSO: A Method for Crystal Structure Prediction. *Comput. Phys. Commun.* **2012**, *183* (10), 2063–2070.
- (69) Kumar, H.; Er, D.; Dong, L.; Li, J.; Shenoy, V. B. Elastic Deformations in 2D van Der Waals Heterostructures and Their Impact on Optoelectronic Properties: Predictions from a Multiscale Computational Approach. *Sci. Rep.* **2015**, *5*, 10872.
- (70) Kumar, H.; Dong, L.; Shenoy, V. B. Limits of Coherency and Strain Transfer in Flexible 2D van Der Waals Heterostructures: Formation of Strain Solitons and Interlayer Debonding. *Sci. Rep.* **2016**, *5*.
- (71) Khorshidi, A.; Peterson, A. A. Amp: A Modular Approach to Machine Learning in Atomistic Simulations. *Comput. Phys. Commun.* **2016**, *207*, 310–324.
- (72) Midtvedt, D.; Lewenkopf, C. H.; Croy, A. Multi-Scale Approach for Strain-Engineering of Phosphorene. *ArXiv170106395 Cond-Mat* **2017**.

- (73) Kaneta, C.; Katayama-Yoshida, H.; Morita, A. Lattice Dynamics of Black Phosphorus. *Solid State Commun.* **1982**, *44* (5), 613–617.
- (74) Jiang, J.-W. Parametrization of Stillinger–Weber Potential Based on Valence Force Field Model: Application to Single-Layer MoS₂ and Black Phosphorus. *Nanotechnology* **2015**, *26* (31), 315706.
- (75) Jiang, J.-W.; Park, H. S.; Rabczuk, T. Molecular Dynamics Simulations of Single-Layer Molybdenum Disulphide (MoS₂): Stillinger-Weber Parametrization, Mechanical Properties, and Thermal Conductivity. *J. Appl. Phys.* **2013**, *114* (6), 064307.
- (76) Midtvedt, D.; Croy, A. Comment on “Parametrization of Stillinger–Weber Potential Based on a Valence Force Field Model: Application to Single-Layer MoS₂ and Black Phosphorus.” *Nanotechnology* **2016**, *27* (23), 238001.
- (77) Zhang, Q.; Çağın, T.; van Duin, A.; Goddard, W. A.; Qi, Y.; Hector, L. G. Adhesion and Nonwetting-Wetting Transition in the $\text{Al}/\text{Al}_2\text{O}_3$ Interface. *Phys. Rev. B* **2004**, *69* (4), 045423.
- (78) Ojwang', J. G. O.; Santen, R. van; Kramer, G. J.; Duin, A. C. T. van; Iii, W. A. G. Predictions of Melting, Crystallization, and Local Atomic Arrangements of Aluminum Clusters Using a Reactive Force Field. *J. Chem. Phys.* **2008**, *129* (24), 244506.
- (79) LaBrosse, M. R.; Johnson, J. K.; van Duin, A. C. T. Development of a Transferable Reactive Force Field for Cobalt. *J. Phys. Chem. A* **2010**, *114* (18), 5855–5861.
- (80) Singh, S. K.; Srinivasan, S. G.; Neek-Amal, M.; Costamagna, S.; van Duin, A. C. T.; Peeters, F. M. Thermal Properties of Fluorinated Graphene. *Phys. Rev. B* **2013**, *87* (10), 104114.
- (81) Mortazavi, B.; Ostadhossein, A.; Rabczuk, T.; van Duin, A. C. T. Mechanical Response of All-MoS₂ Single-Layer Heterostructures: A ReaxFF Investigation. *Phys Chem Chem Phys* **2016**, *18* (34), 23695–23701.
- (82) Segall, M. D.; Lindan, P. J. D.; Probert, M. J.; Pickard, C. J.; Hasnip, P. J.; Clark, S. J.; Payne, M. C. First-Principles Simulation: Ideas, Illustrations and the CASTEP Code. *J. Phys. Condens. Matter* **2002**, *14* (11), 2717.
- (83) Payne, M. C.; Teter, M. P.; Allan, D. C.; Arias, T. A.; Joannopoulos, J. D. Iterative Minimization Techniques for *ab Initio* Total-Energy Calculations: Molecular Dynamics and Conjugate Gradients. *Rev. Mod. Phys.* **1992**, *64* (4), 1045–1097.
- (84) Perdew, J. P.; Burke, K.; Ernzerhof, M. Generalized Gradient Approximation Made Simple. *Phys. Rev. Lett.* **1996**, *77* (18), 3865–3868.
- (85) Grimme, S. Semiempirical GGA-Type Density Functional Constructed with a Long-Range Dispersion Correction. *J. Comput. Chem.* **2006**, *27* (15), 1787–1799.
- (86) Monkhorst, H. J.; Pack, J. D. Special Points for Brillouin-Zone Integrations. *Phys. Rev. B* **1976**, *13* (12), 5188–5192.
- (87) Roundy, D.; Cohen, M. L. Ideal Strength of Diamond, Si, and Ge. *Phys. Rev. B* **2001**, *64* (21), 212103.
- (88) Luo, W.; Roundy, D.; Cohen, M. L.; Morris, J. W. Ideal Strength of Bcc Molybdenum and Niobium. *Phys. Rev. B* **2002**, *66* (9), 094110.
- (89) Wei, Q.; Peng, X. Superior Mechanical Flexibility of Phosphorene and Few-Layer Black Phosphorus. *Appl. Phys. Lett.* **2014**, *104* (25), 251915.
- (90) Hu, W.; Yang, J. Defects in Phosphorene. *J. Phys. Chem. C* **2015**, *119* (35), 20474–20480.

- (91) Ding, Y.; Wang, Y. Structural, Electronic, and Magnetic Properties of Adatom Adsorptions on Black and Blue Phosphorene: A First-Principles Study. *J. Phys. Chem. C* **2015**, *119* (19), 10610–10622.
- (92) Brown, A.; Rundqvist, S. Refinement of the Crystal Structure of Black Phosphorus. *Acta Crystallogr.* **1965**, *19* (4), 684–685.
- (93) Jones, R. O.; Hohl, D. Structure of Phosphorus Clusters Using Simulated annealing—P₂ to P₈. *J. Chem. Phys.* **1990**, *92* (11), 6710–6721.
- (94) Pauling, L.; Simonetta, M. Bond Orbitals and Bond Energy in Elementary Phosphorus. *J. Chem. Phys.* **1952**, *20* (1), 29.
- (95) Osman, R.; Coffey, P.; Van Wazer, J. R. Use of Pseudopotential Theory to Study Molecular Structure. II. NOCOR (Neglect of Core Orbitals) Calculation of the P₄ and P₂ Molecules and Their Interconversion. *Inorg. Chem.* **1976**, *15* (2), 287–292.
- (96) Plimpton, S. Fast Parallel Algorithms for Short-Range Molecular Dynamics. *J. Comput. Phys.* **1995**, *117* (1), 1–19.
- (97) Nosé S. A Unified Formulation of the Constant Temperature Molecular Dynamics Methods. *J. Chem. Phys.* **1984**, *81* (1), 511–519.
- (98) Hoover, W. G. Canonical Dynamics: Equilibrium Phase-Space Distributions. *Phys. Rev. A* **1985**, *31* (3), 1695–1697.
- (99) Vilhelmsen, L. B.; Hammer, B. A Genetic Algorithm for First Principles Global Structure Optimization of Supported Nano Structures. *J. Chem. Phys.* **2014**, *141* (4), 044711.
- (100) Dittner, M.; Müller, J.; Aktulga, H. M.; Hartke, B. Efficient Global Optimization of Reactive Force-Field Parameters. *J. Comput. Chem.* **2015**, *36* (20), 1550–1561.
- (101) Chenoweth, K.; van Duin, A. C. T.; Goddard, W. A. ReaxFF Reactive Force Field for Molecular Dynamics Simulations of Hydrocarbon Oxidation. *J. Phys. Chem. A* **2008**, *112* (5), 1040–1053.
- (102) Rossini, F. D.; Rossini, F. D. *Selected Values of Chemical Thermodynamic Properties*; US Government Printing Office Washington, DC, 1952; Vol. 500.
- (103) Freysoldt, C.; Grabowski, B.; Hickel, T.; Neugebauer, J.; Kresse, G.; Janotti, A.; Van de Walle, C. G. First-Principles Calculations for Point Defects in Solids. *Rev. Mod. Phys.* **2014**, *86* (1), 253–305.
- (104) Komsa, H.-P.; Kotakoski, J.; Kurasch, S.; Lehtinen, O.; Kaiser, U.; Krashennnikov, A. V. Two-Dimensional Transition Metal Dichalcogenides under Electron Irradiation: Defect Production and Doping. *Phys. Rev. Lett.* **2012**, *109* (3), 035503.
- (105) Hao, F.; Chen, X. First-Principles Study of the Defected Phosphorene under Tensile Strain. *J. Appl. Phys.* **2016**, *120* (16), 165104.
- (106) Brent, J. R.; Savjani, N.; Lewis, E. A.; Haigh, S. J.; Lewis, D. J.; O'Brien, P. Production of Few-Layer Phosphorene by Liquid Exfoliation of Black Phosphorus. *Chem. Commun.* **2014**, *50* (87), 13338–13341.
- (107) Das, S.; Demarteau, M.; Roelofs, A. Ambipolar Phosphorene Field Effect Transistor. *ACS Nano* **2014**, *8* (11), 11730–11738.
- (108) Guan, J.; Zhu, Z.; Tománek, D. High Stability of Faceted Nanotubes and Fullerenes of Multiphase Layered Phosphorus: A Computational Study. *Phys. Rev. Lett.* **2014**, *113* (22), 226801.
- (109) Guo, H.; Lu, N.; Dai, J.; Wu, X.; Zeng, X. C. Phosphorene Nanoribbons, Phosphorus Nanotubes, and van Der Waals Multilayers. *J. Phys. Chem. C* **2014**, *118* (25), 14051–14059.

- (110) Liu, H.; Neal, A. T.; Si, M.; Du, Y.; Peide, D. Y. The Effect of Dielectric Capping on Few-Layer Phosphorene Transistors: Tuning the Schottky Barrier Heights. *IEEE Electron Device Lett.* **2014**, *35* (7), 795–797.
- (111) Liu, H.; Neal, A. T.; Zhu, Z.; Xu, X.; Tomanek, D.; Ye, P. D.; Luo, Z. Phosphorene: An Unexplored 2D Semiconductor with a High Hole Mobility. *ACS Nano* **2014**.
- (112) Seifert, G.; Hernández, E. Theoretical Prediction of Phosphorus Nanotubes. *Chem. Phys. Lett.* **2000**, *318* (4), 355–360.
- (113) Liao, X.; Hao, F.; Xiao, H.; Chen, X. Effects of Intrinsic Strain on the Structural Stability and Mechanical Properties of Phosphorene Nanotubes. *Nanotechnology* **2016**, *27* (21), 215701.
- (114) König, M.; Wiedmann, S.; Brüne, C.; Roth, A.; Buhmann, H.; Molenkamp, L. W.; Qi, X.-L.; Zhang, S.-C. Quantum Spin Hall Insulator State in HgTe Quantum Wells. *Science* **2007**, *318* (5851), 766–770.
- (115) Cahangirov, S.; Topsakal, M.; Aktürk, E.; Şahin, H.; Ciraci, S. Two- and One-Dimensional Honeycomb Structures of Silicon and Germanium. *Phys. Rev. Lett.* **2009**, *102* (23), 236804.
- (116) Vogt, P.; De Padova, P.; Quaresima, C.; Avila, J.; Frantzeskakis, E.; Asensio, M. C.; Resta, A.; Ealet, B.; Le Lay, G. Silicene: Compelling Experimental Evidence for Graphenelike Two-Dimensional Silicon. *Phys. Rev. Lett.* **2012**, *108* (15), 155501.
- (117) Dávila, M. E.; Xian, L.; Cahangirov, S.; Rubio, A.; Lay, G. L. Germanene: A Novel Two-Dimensional Germanium Allotrope Akin to Graphene and Silicene. *New J. Phys.* **2014**, *16* (9), 095002.
- (118) Özçelik, V. O.; Durgun, E.; Ciraci, S. New Phases of Germanene. *J. Phys. Chem. Lett.* **2014**, *5* (15), 2694–2699.
- (119) Tang, P.; Chen, P.; Cao, W.; Huang, H.; Cahangirov, S.; Xian, L.; Xu, Y.; Zhang, S.-C.; Duan, W.; Rubio, A. Stable Two-Dimensional Dumbbell Stanene: A Quantum Spin Hall Insulator. *Phys. Rev. B* **2014**, *90* (12), 121408.
- (120) Tao, L.; Cinquanta, E.; Chiappe, D.; Grazianetti, C.; Fanciulli, M.; Dubey, M.; Molle, A.; Akinwande, D. Silicene Field-Effect Transistors Operating at Room Temperature. *Nat. Nanotechnol.* **2015**, *10* (3), 227–231.
- (121) Wang, Q. H.; Kalantar-Zadeh, K.; Kis, A.; Coleman, J. N.; Strano, M. S. Electronics and Optoelectronics of Two-Dimensional Transition Metal Dichalcogenides. *Nat. Nanotechnol.* **2012**, *7* (11), 699–712.
- (122) Chhowalla, M.; Shin, H. S.; Eda, G.; Li, L.-J.; Loh, K. P.; Zhang, H. The Chemistry of Two-Dimensional Layered Transition Metal Dichalcogenide Nanosheets. *Nat. Chem.* **2013**, *5* (4), 263–275.
- (123) Jariwala, D.; Sangwan, V. K.; Lauhon, L. J.; Marks, T. J.; Hersam, M. C. Emerging Device Applications for Semiconducting Two-Dimensional Transition Metal Dichalcogenides. *ACS Nano* **2014**, *8* (2), 1102–1120.
- (124) Xu, X.; Yao, W.; Xiao, D.; Heinz, T. F. Spin and Pseudospins in Layered Transition Metal Dichalcogenides. *Nat. Phys.* **2014**, *10* (5), 343–350.
- (125) Qian, X.; Liu, J.; Fu, L.; Li, J. Quantum Spin Hall Effect in Two-Dimensional Transition Metal Dichalcogenides. *Science* **2014**, *346* (6215), 1344–1347.
- (126) Cong, C.; Shang, J.; Wu, X.; Cao, B.; Peimyoo, N.; Qiu, C.; Sun, L.; Yu, T. Synthesis and Optical Properties of Large-Area Single-Crystalline 2D Semiconductor WS₂ Monolayer from Chemical Vapor Deposition. *Adv. Opt. Mater.* **2014**, *2* (2), 131–136.

- (127) Novoselov, K. S.; Geim, A. K.; Morozov, S. V.; Jiang, D.; Zhang, Y.; Dubonos, S. V.; Grigorieva, I. V.; Firsov, A. A. Electric Field Effect in Atomically Thin Carbon Films. *Science* **2004**, *306* (5696), 666–669.
- (128) Xia, F.; Wang, H.; Xiao, D.; Dubey, M.; Ramasubramaniam, A. Two-Dimensional Material Nanophotonics. *Nat. Photonics* **2014**, *8* (12), 899–907.
- (129) Bernardi, M.; Palummo, M.; Grossman, J. C. Extraordinary Sunlight Absorption and One Nanometer Thick Photovoltaics Using Two-Dimensional Monolayer Materials. *Nano Lett.* **2013**, *13* (8), 3664–3670.
- (130) Mas-Ballesté R.; Gómez-Navarro, C.; Gómez-Herrero, J.; Zamora, F. 2D Materials: To Graphene and beyond. *Nanoscale* **2011**, *3* (1), 20–30.
- (131) Butler, S. Z.; Hollen, S. M.; Cao, L.; Cui, Y.; Gupta, J. A.; Gutiérrez, H. R.; Heinz, T. F.; Hong, S. S.; Huang, J.; Ismach, A. F.; et al. Progress, Challenges, and Opportunities in Two-Dimensional Materials Beyond Graphene. *ACS Nano* **2013**, *7* (4), 2898–2926.
- (132) Oganov, A. R.; Glass, C. W. Crystal Structure Prediction Using Ab Initio Evolutionary Techniques: Principles and Applications. *J. Chem. Phys.* **2006**, *124* (24), 244704.
- (133) Oganov, A. R.; Lyakhov, A. O.; Valle, M. How Evolutionary Crystal Structure Prediction Works—and Why. *Acc. Chem. Res.* **2011**, *44* (3), 227–237.
- (134) Giannozzi, P.; Baroni, S.; Bonini, N.; Calandra, M.; Car, R.; Cavazzoni, C.; Davide Ceresoli; Chiarotti, G. L.; Cococcioni, M.; Dabo, I.; et al. QUANTUM ESPRESSO: A Modular and Open-Source Software Project for Quantum Simulations of Materials. *J. Phys. Condens. Matter* **2009**, *21* (39), 395502.
- (135) Sham, L. J.; Schlüter, M. Density-Functional Theory of the Energy Gap. *Phys. Rev. Lett.* **1983**, *51* (20), 1888–1891.
- (136) Perdew, J. P.; Levy, M. Physical Content of the Exact Kohn-Sham Orbital Energies: Band Gaps and Derivative Discontinuities. *Phys. Rev. Lett.* **1983**, *51* (20), 1884–1887.
- (137) Hedin, L. New Method for Calculating the One-Particle Green’s Function with Application to the Electron-Gas Problem. *Phys. Rev.* **1965**, *139* (3A), A796–A823.
- (138) Marini, A.; Hogan, C.; Grüning, M.; Varsano, D. Yambo: An Ab Initio Tool for Excited State Calculations. *Comput. Phys. Commun.* **2009**, *180* (8), 1392–1403.
- (139) Aulbur, W. G.; Jönsson, L.; Wilkins, J. W. Quasiparticle Calculations in Solids. In *Solid State Physics*; Spaepen, H. E. and F., Ed.; Academic Press, 2000; Vol. 54, pp 1–218.
- (140) Salpeter, E. E.; Bethe, H. A. A Relativistic Equation for Bound-State Problems. *Phys. Rev.* **1951**, *84* (6), 1232–1242.
- (141) Onida, G.; Reining, L.; Rubio, A. Electronic Excitations: Density-Functional versus Many-Body Green’s-Function Approaches. *Rev. Mod. Phys.* **2002**, *74* (2), 601–659.
- (142) Spataru, C. D.; Ismail-Beigi, S.; Benedict, L. X.; Louie, S. G. Quasiparticle Energies, Excitonic Effects and Optical Absorption Spectra of Small-Diameter Single-Walled Carbon Nanotubes. *Appl. Phys. A* **2004**, *78* (8), 1129–1136.
- (143) Yang, L.; Spataru, C. D.; Louie, S. G.; Chou, M. Y. Enhanced Electron-Hole Interaction and Optical Absorption in a Silicon Nanowire. *Phys. Rev. B* **2007**, *75* (20), 201304.
- (144) VandeVondele, J.; Hutter, J. Gaussian Basis Sets for Accurate Calculations on Molecular Systems in Gas and Condensed Phases. *J. Chem. Phys.* **2007**, *127* (11), 114105.
- (145) VandeVondele, J.; Krack, M.; Mohamed, F.; Parrinello, M.; Chassaing, T.; Hutter, J. Quickstep: Fast and Accurate Density Functional Calculations Using a Mixed Gaussian and Plane Waves Approach. *Comput. Phys. Commun.* **2005**, *167* (2), 103–128.

- (146) Zandiataashbar, A.; Lee, G.-H.; An, S. J.; Lee, S.; Mathew, N.; Terrones, M.; Hayashi, T.; Picu, C. R.; Hone, J.; Koratkar, N. Effect of Defects on the Intrinsic Strength and Stiffness of Graphene. *Nat. Commun.* **2014**, *5*, 3186.
- (147) Wang, G.; Slough, W. J.; Pandey, R.; Karna, S. P. Degradation of Phosphorene in Air: Understanding at Atomic Level. *2D Mater.* **2016**, *3* (2), 025011.
- (148) Geim, A. K.; Grigorieva, I. V. Van Der Waals Heterostructures. *Nature* **2013**, *499* (7459), 419–425.
- (149) Nicolosi, V.; Chhowalla, M.; Kanatzidis, M. G.; Strano, M. S.; Coleman, J. N. Liquid Exfoliation of Layered Materials. *Science* **2013**, *340* (6139), 1226419.
- (150) Paton, K. R.; Varrla, E.; Backes, C.; Smith, R. J.; Khan, U.; O'Neill, A.; Boland, C.; Lotya, M.; Istrate, O. M.; King, P.; et al. Scalable Production of Large Quantities of Defect-Free Few-Layer Graphene by Shear Exfoliation in Liquids. *Nat. Mater.* **2014**, *13* (6), 624–630.
- (151) Li, Y.; Liao, Y.; Chen, Z. Be₂C Monolayer with Quasi-Planar Hexacoordinate Carbons: A Global Minimum Structure. *Angew. Chem. Int. Ed.* **2014**, *53* (28), 7248–7252.
- (152) Abraham, M. H.; Grellier, P. L.; Abboud, J.-L. M.; Doherty, R. M.; Taft, R. W. Solvent Effects in Organic Chemistry-Recent Developments. *Can. J. Chem.* **1988**, *66* (11), 2673–2686.
- (153) Zhang, Q.; Bell, R.; Truong, T. N. Ab Initio and Density Functional Theory Studies of Proton Transfer Reactions in Multiple Hydrogen Bond Systems. *J. Phys. Chem.* **1995**, *99* (2), 592–599.
- (154) Wang, B.; Cao, Z. How Water Molecules Modulate the Hydration of CO₂ in Water Solution: Insight from the Cluster-Continuum Model Calculations. *J. Comput. Chem.* **2013**, *34* (5), 372–378.
- (155) Jaramillo, P.; Coutinho, K.; Canuto, S. Solvent Effects in Chemical Processes. Water-Assisted Proton Transfer Reaction of Pterin in Aqueous Environment. *J. Phys. Chem. A* **2009**, *113* (45), 12485–12495.
- (156) Huck, W. T. S. Effects of Nanoconfinement on the Morphology and Reactivity of Organic Materials. *Chem. Commun.* **2005**, No. 33, 4143–4148.
- (157) Marracino, P.; Amadei, A.; Apollonio, F.; d'Inzeo, G.; Liberti, M.; Crescenzo, A. di; Fontana, A.; Zappacosta, R.; Aschi, M. Modeling of Chemical Reactions in Micelle: Water-Mediated Keto–Enol Interconversion As a Case Study. *J. Phys. Chem. B* **2011**, *115* (25), 8102–8111.
- (158) Heisler, I. A.; Kondo, M.; Meech, S. R. Reactive Dynamics in Confined Liquids: Ultrafast Torsional Dynamics of Auramine O in Nanoconfined Water in Aerosol OT Reverse Micelles. *J. Phys. Chem. B* **2009**, *113* (6), 1623–1631.
- (159) Gilliland, J. W.; Yokoyama, K.; Yip, W. T. Solvent Effect on Mobility and Photostability of Organic Dyes Embedded inside Silica Sol–Gel Thin Films. *Chem. Mater.* **2005**, *17* (26), 6702–6712.
- (160) Abou-Zied, O. K. Steady-State and Time-Resolved Spectroscopy of 2,2'-Bipyridine-3,3'-Diol in Solvents and Cyclodextrins: Polarity and Nanoconfinement Effects on Tautomerization. *J. Phys. Chem. B* **2010**, *114* (2), 1069–1076.
- (161) Daiguji, H.; Yang, P.; Majumdar, A. Ion Transport in Nanofluidic Channels. *Nano Lett.* **2004**, *4* (1), 137–142.
- (162) Ranatunga, K. M.; Shrivastava, I. H.; Smith, G. R.; Sansom, M. S. Side-Chain Ionization States in a Potassium Channel. *Biophys. J.* **2001**, *80* (3), 1210–1219.

- (163) Truskett, T. M. The Subtleties of Water in Small Spaces. *Proc. Natl. Acad. Sci. U. S. A.* **2003**, *100* (18), 10139–10140.
- (164) Park, S.; Moilanen, D. E.; Fayer, M. D. Water Dynamics The Effects of Ions and Nanoconfinement. *J. Phys. Chem. B* **2008**, *112* (17), 5279–5290.
- (165) Shi, X.; Xiao, H.; Lackner, K. S.; Chen, X. Capture CO₂ from Ambient Air Using Nanoconfined Ion Hydration. *Angew. Chem.* **2016**, *128* (12), 4094–4097.
- (166) Shi, X.; Xiao, H.; Chen, X.; Lackner, K. S. The Effect of Moisture on the Hydrolysis of Basic Salts. *Chem. - Eur. J.* **2016**, *22* (51), 18326–18330.
- (167) Goedecker, S. Minima Hopping: An Efficient Search Method for the Global Minimum of the Potential Energy Surface of Complex Molecular Systems. *J. Chem. Phys.* **2004**, *120* (21), 9911–9917.
- (168) Grimme, S.; Antony, J.; Ehrlich, S.; Krieg, H. A Consistent and Accurate Ab Initio Parametrization of Density Functional Dispersion Correction (DFT-D) for the 94 Elements H–Pu. *J. Chem. Phys.* **2010**, *132* (15), 154104.
- (169) Lee, C.; Yang, W.; Parr, R. G. Development of the Colle-Salvetti Correlation-Energy Formula into a Functional of the Electron Density. *Phys. Rev. B* **1988**, *37* (2), 785–789.
- (170) Grimme, S.; Ehrlich, S.; Goerigk, L. Effect of the Damping Function in Dispersion Corrected Density Functional Theory. *J. Comput. Chem.* **2011**, *32* (7), 1456–1465.
- (171) Marenich, A. V.; Cramer, C. J.; Truhlar, D. G. Universal Solvation Model Based on Solute Electron Density and on a Continuum Model of the Solvent Defined by the Bulk Dielectric Constant and Atomic Surface Tensions. *J. Phys. Chem. B* **2009**, *113* (18), 6378–6396.
- (172) Schock, M. R. Response of Lead Solubility to Dissolved Carbonate in Drinking Water. *J. Am. Water Works Assoc.* **1980**, *72* (12), 695–704.
- (173) Mohammed, O. F.; Pines, D.; Dreyer, J.; Pines, E.; Nibbering, E. T. J. Sequential Proton Transfer Through Water Bridges in Acid-Base Reactions. *Science* **2005**, *310* (5745), 83–86.
- (174) Kamachi, T.; Yoshizawa, K. Water-Assisted Oxo Mechanism for Heme Metabolism. *J. Am. Chem. Soc.* **2005**, *127* (30), 10686–10692.
- (175) Lima, M. C. P.; Coutinho, K.; Canuto, S.; Rocha, W. R. Reaction Mechanism and Tautomeric Equilibrium of 2-Mercaptopyrimidine in the Gas Phase and in Aqueous Solution: A Combined Monte Carlo and Quantum Mechanics Study. *J. Phys. Chem. A* **2006**, *110* (22), 7253–7261.
- (176) Legrand, P.; Barratt, G.; Mosqueira, V.; Fessi, H.; Devissaguet, J. P. Polymeric Nanocapsules as Drug Delivery Systems. A Review. *STP Pharma Sci.* **1999**, *9* (5), 411–418.
- (177) Barratt, G. M. Therapeutic Applications of Colloidal Drug Carriers. *Pharm. Sci. Technol. Today* **2000**, *3* (5), 163–171.
- (178) Sinha, V. R.; Bansal, K.; Kaushik, R.; Kumria, R.; Trehan, A. Poly- ϵ -Caprolactone Microspheres and Nanospheres: An Overview. *Int. J. Pharm.* **2004**, *278* (1), 1–23.
- (179) Letchford, K.; Burt, H. A Review of the Formation and Classification of Amphiphilic Block Copolymer Nanoparticulate Structures: Micelles, Nanospheres, Nanocapsules and Polymersomes. *Eur. J. Pharm. Biopharm. Off. J. Arbeitsgemeinschaft Für Pharm. Verfahrenstechnik EV* **2007**, *65* (3), 259–269.
- (180) Delcea, M.; Yashchenok, A.; Videnova, K.; Kreft, O.; Möhwald, H.; Skirtach, A. G. Multicompartmental Micro- and Nanocapsules: Hierarchy and Applications in Biosciences. *Macromol. Biosci.* **2010**, *10* (5), 465–474.

- (181) Kothamasu, P.; Kanumur, H.; Ravur, N.; Maddu, C.; Parasuramrajam, R.; Thangavel, S. Nanocapsules: The Weapons for Novel Drug Delivery Systems. *BioImpacts BI* **2012**, 2 (2), 71–81.
- (182) Giovambattista, N.; Rossky, P. J.; Debenedetti, P. G. Phase Transitions Induced by Nanoconfinement in Liquid Water. *Phys. Rev. Lett.* **2009**, 102 (5), 050603.
- (183) Iijima, S. Helical Microtubules of Graphitic Carbon. *Nature* **1991**, 354 (6348), 56–58.
- (184) Harris, P. J. F. *Carbon Nanotube Science: Synthesis, Properties and Applications*; Cambridge University Press, 2009.
- (185) Saito, R.; Fujita, M.; Dresselhaus, G.; Dresselhaus, M. S. Electronic Structure of Graphene Tubules Based on $\{\mathrm{C}\}_{60}$. *Phys. Rev. B* **1992**, 46 (3), 1804–1811.
- (186) Mintmire, J. W.; Dunlap, B. I.; White, C. T. Are Fullerene Tubules Metallic? *Phys. Rev. Lett.* **1992**, 68 (5), 631–634.
- (187) Falvo, M. R.; Clary, G. J.; Taylor, R. M.; Chi, V.; Brooks, F. P.; Washburn, S.; Superfine, R. Bending and Buckling of Carbon Nanotubes under Large Strain. *Nature* **1997**, 389 (6651), 582–584.
- (188) Iijima, S.; Ichihashi, T. Single-Shell Carbon Nanotubes of 1-Nm Diameter. *Nature* **1993**, 363 (6430), 603–605.
- (189) Baughman, R. H. Putting a New Spin on Carbon Nanotubes. *Science* **2000**, 290 (5495), 1310–1311.
- (190) Walther, J. H.; Jaffe, R.; Halicioglu, T.; Koumoutsakos, P. Carbon Nanotubes in Water: Structural Characteristics and Energetics. *J. Phys. Chem. B* **2001**, 105 (41), 9980–9987.
- (191) A Modified TIP3P Water Potential for Simulation with Ewald Summation. *J. Chem. Phys.* **2004**, 121 (20), 10096–10103.
- (192) Hockney, R. W.; Eastwood, J. W. *Computer Simulation Using Particles*; CRC Press, 1988.
- (193) Hummer, G.; Rasaiah, J. C.; Noworyta, J. P. Water Conduction through the Hydrophobic Channel of a Carbon Nanotube. *Nature* **2001**, 414 (6860), 188–190.
- (194) Algara-Siller, G.; Lehtinen, O.; Wang, F. C.; Nair, R. R.; Kaiser, U.; Wu, H. A.; Geim, A. K.; Grigorieva, I. V. Square Ice in Graphene Nanocapillaries. *Nature* **2015**, 519 (7544), 443–445.
- (195) Vasu, K. S.; Prestat, E.; Abraham, J.; Dix, J.; Kashtiban, R. J.; Beheshtian, J.; Sloan, J.; Carbone, P.; Neek-Amal, M.; Haigh, S. J.; et al. Van Der Waals Pressure and Its Effect on Trapped Interlayer Molecules. *Nat. Commun.* **2016**, 7, 12168.
- (196) Chen, X. Q.; Saito, T.; Yamada, H.; Matsushige, K. Aligning Single-Wall Carbon Nanotubes with an Alternating-Current Electric Field. *Appl. Phys. Lett.* **2001**, 78 (23), 3714–3716.
- (197) Senthil Kumar, M.; Lee, S. H.; Kim, T. Y.; Kim, T. H.; Song, S. M.; Yang, J. W.; Nahm, K. S.; Suh, E.-K. DC Electric Field Assisted Alignment of Carbon Nanotubes on Metal Electrodes. *Solid-State Electron.* **2003**, 47 (11), 2075–2080.
- (198) Kamat, P. V.; Thomas, K. G.; Barazzouk, S.; Girishkumar, G.; Vinodgopal, K.; Meisel, D. Self-Assembled Linear Bundles of Single Wall Carbon Nanotubes and Their Alignment and Deposition as a Film in a Dc Field. *J. Am. Chem. Soc.* **2004**, 126 (34), 10757–10762.
- (199) Shi, X.; Cheng, Y.; Pugno, N. M.; Gao, H. Tunable Water Channels with Carbon Nanoscrolls. *Small* **2010**, 6 (6), 739–744.
- (200) Zhu, S.; Li, T. Hydrogenation-Assisted Graphene Origami and Its Application in Programmable Molecular Mass Uptake, Storage, and Release. *ACS Nano* **2014**, 8 (3), 2864–2872.